

**FINAL REPORT  
FOR  
High-Bandwidth Direct Modulation of Distributed-Feedback  
Quantum-Well Lasers**

**May 1, 1996 - July 31, 1999**

**Submitted to**

**Dr. Yoon-Soo Park  
CODE 312  
Office of Naval Research  
800 N. Quincy Street  
Arlington, VA 22217-5660**

**Grant No. N00014-96-1-0902  
(AASERT)**

**Prepared by**

**S. L. Chuang  
Department of Electrical and Computer Engineering  
University of Illinois at Urbana-Champaign  
Urbana, IL 61801**

**February 1, 2000**

**DTIC QUALITY INSPECTED 1**

**DISTRIBUTION STATEMENT A  
Approved for Public Release  
Distribution Unlimited**

**20000211 018**

**FINAL REPORT on AASERT Project**  
(May 1, 1996 - July 31, 1999)

**1. Contract Title:** High-Bandwidth Direct Modulation of Distributed-Feedback Quantum-Well Lasers

**Number:** N00014-96-1-0902

**PI:** Professor S. L. Chuang  
University of Illinois at Urbana-Champaign  
Department of Electrical and Computer Engineering  
1406 W. Green Street, Urbana, IL 61801  
Phone: (217) 333-3359 Fax: (217) 333-5701  
email: s-chuang@uiuc.edu

**Program Manager:** Dr. Y. S. Park, Code: ONR 312

**2. Technical Objectives:**

Wide-bandwidth microwave modulation of semiconductor strained quantum-well lasers using distributed-feedback structures plays an important role in high bit-rate optical communication systems. It is therefore critical to conduct research on the device physics of strained semiconductor quantum-well lasers under high-frequency modulation and on the creation of new techniques to characterize high-speed quantum-well lasers. The goals of this project are (1) to design and fabricate high bandwidth distributed-feedback quantum-well lasers using strain effects and (2) to combine microwave and optical measurement techniques to investigate the physics and device performance of quantum-well lasers under high-speed modulation conditions. The project is interdisciplinary in nature since optoelectronic device technology, microwave and optical measurement techniques will be introduced to the study of high-frequency modulation of quantum-well lasers for optical communication systems.

**3. Approach**

- a. Use electrical current injection to measure the transport and intrinsic high-speed parameters of semiconductor laser and study the temperature sensitivity of these parameters.
- b. Use optical injection by pumping in the absorption region (cross-absorption modulation) to study the intrinsic small-signal modulation response of semiconductor lasers.
- c. Use optical injection by pumping in the gain region (cross-gain modulation) to study high-speed gain competition phenomena of semiconductor lasers and realize wavelength conversion.
- d. Demonstrate a novel wavelength conversion experiment by cross-absorption modulation in an integrated electro-absorption modulator/laser.
- e. Demonstrate a novel wavelength conversion experiment by cross-gain modulation in a multisection integrated laser/modulator device.
- f. Conduct experiments on four-wave mixing in conventional and novel three-electrode DFB lasers and study their polarization dependence.

**4. Accomplishments**

**A. Broaden Bandwidth by Optical Pumping in the Absorption Region.**

We study both theoretically and experimentally high-speed optical injection in the absorption region of a quantum-well laser, and compare the results with those from electrical injection including the carrier transport effect. We show that the main difference between the two responses is the low frequency roll-off. By using both injection methods, we obtain more accurate and consistent measurements of many important dynamic laser parameters which include the differential gain, carrier lifetime, K factor, and gain compression factor. Temperature-dependent data of the test laser are presented which show that the most dominant effect is the linear degradation of differential gain and injection efficiency with increasing temperature. While the K-factor is insensitive to temperature variation for multiple-quantum-well lasers, we find that the carrier capture time and nonlinear gain suppression coefficient decreases as temperature increases.

#### **B. Small-Signal Cross-Gain Modulation in Semiconductor Lasers**

We derive new rate equations for the high-speed frequency response of a test quantum-well laser in the presence of an external microwave modulated optical pump in the gain region. The model includes the effects of pump-induced stimulated recombination and cross gain saturation. Expressions for the small-signal modulation response of the test laser under gain modulation are derived. We use a multiple-quantum-well InGaAlAs Fabry-Perot (FP) laser at 1.552  $\mu\text{m}$  as the test laser and a DFB laser at 1.542  $\mu\text{m}$  as the external pump. Our data shows a reduction of carrier lifetime with increasing optical pumping, a shift of the probe laser threshold current, a change in the K factor, and a variation of the relaxation frequency with different pump powers. The experimental results agree very well with the theoretical results.

#### **C. Wavelength Conversion by Cross-Absorption Modulation Using an Integrated Electroabsorption Laser/Modulator**

Wavelength conversion by cross-absorption modulation has been demonstrated using an integrated electroabsorption modulator/distributed-feedback laser which acts as the conversion medium and converted wavelength light source. Dependencies on pump wavelength and modulator voltage have been investigated.

#### **D. Dual Pump Four-wave Mixing in a Double-moded Distributed-Feedback Laser**

We present a comprehensive theoretical model with experimental results on four-wave mixing in a DFB laser with two pump modes. The twin lasing modes serve as pump waves for the four-wave mixing which takes place within the laser cavity. We show new experimental measurements of the two-pump four-wave mixing conversion efficiency spectrum and show that to first order there is no fundamental dependence of the conversion efficiency on pump separation. The indicates significant improvement in the probe and conjugate wavelength separation and conversion efficiency. Our theoretical model agrees quite well with the measured data and predicts the key experimentally observed phenomena including the relative invariance of the conversion efficiency on pump separation and the strong enhancement of certain conjugate waves when the probe detuning is close to the pump separation.

#### **4. Significance of this work:**

The fundamental research conducted here, which includes electrical, optical absorption and optical gain high-speed responses, allows for a better understanding of current device limitations on broad-bandwidth semiconductor laser performance, and will enhance high-speed device design. Our investigation of applications for strained quantum-well optoelectronics such as wavelength conversion by cross-gain and cross-absorption

modulation enable wavelength switching in dense WDM networks. The high-speed modulation in distributed-feedback (DFB) lasers is essential for enabling the growth of future optical communication systems. Study of high-speed modulation in integrated laser/modulator devices is critical to develop broad-bandwidth transmitters.

## **6. Papers, Patents, and Awards:**

### **(Publications)**

#### **(i) Journal Papers**

1. W. Fang, M. Hattendorf, S. L. Chuang, J. Minch, C. S. Chang, C. G. Bethea, and Y. K. Chen, "Analysis of temperature sensitivity in semiconductor lasers using gain and spontaneous emission measurements," *Appl. Phys. Lett.*, vol. 70, pp. 796-798, 1997.
2. J. Minch, C. S. Chang, and S. L. Chuang, "Four-wave mixing in a distributed-feedback laser," *Appl. Phys. Lett.*, vol. 70, pp. 1360-1362, 1997.
3. J. Minch, S. L. Chuang, C. S. Chang, W. Fang, Y. K. Chen, and T. Tanbun-Ek, "Theory and experiment on the amplified spontaneous emission from distributed-feedback lasers," *IEEE J. Quantum Electron.*, vol. 33, pp. 815-823, 1997.
4. J. Minch, C. S. Chang, and S. L. Chuang, "Wavelength conversion in distributed-feedback lasers," *IEEE J. Selected Topics Quantum Electronics*, vol. 3, pp. 569-576, 1997.
5. W. Fang, A. Hsu, S. L. Chuang, T. Tanbun-Ek, and A. M. Sergent, "Measurement and modeling of distributed-feedback lasers with spatial hole burning," *IEEE J. Selected Topics Quantum Electronics*, vol. 3, pp. 547-554, 1997.
6. T. Keating, J. Minch, C. S. Chang, P. Enders, W. Fang, S. L. Chuang, T. Tanbun-Ek, T. K. Chen, and M. Sergent, "Optical gain and refractive index of a laser amplifier in the presence of pump light for cross-gain and cross-phase modulation," *IEEE Photon. Technol. Lett.*, vol. 9, pp. 1358-1360, 1997.
7. J. Minch, S. H. Park, T. Keating and S. L. Chuang, "Theory and Experiment of InGaAsP and InGaAlAs long-wavelength strained quantum-well lasers," *IEEE J. Quant. Electron.*, vol. 35, pp. 771-782, 1999.
8. T. Keating, S. H. Park, J. Minch, X. Jin, and S. L. Chuang, "Optical gain measurements based on fundamental properties and comparison with many-body theory," *J. Appl. Phys.*, vol. 86, pp. 2945-2952, 1999.
9. A. Hsu, S. L. Chuang, W. Fang, L. Adams, G. Nykolak, and T. Tanbun-Ek, "A Wavelength-Tunable Curved Waveguide DFB Laser with Integrated Modulator," *IEEE J. Quant. Electron.*, vol. 35, pp. 961-969, 1999.
10. T. Keating, X. Jin, S. L. Chuang, and K. Hess, "Temperature dependence of electrical and optical modulation responses of quantum-well lasers," *IEEE J. Quantum Electron.*, vol. 35, pp. 1526-1534, 1999.
11. J. Minch and S. L. Chuang, "Dual-pump four-wave mixing in a double-mode distributed feedback laser," *J. Opt. Soc. Am. B*, vol. 17, pp. 53-62, 2000.

#### **(ii) Presentations**

12. J. Minch, C. S. Chang, W. Fang, S. L. Chuang, Y. K. Chen, and T. Tanbun-Ek, "Theory and experiment on the amplified spontaneous emission from DFB lasers," *Conference on Lasers and Electro-Optics*, Anaheim, CA, June 2-7, 1996.
13. W. Fang, C. G. Bethea, Y. K. Chen, T. Tanbun-Ek, and S. L. Chuang, "Measurements of spatially dependent carrier lifetimes in 1.55  $\mu\text{m}$  DFB quantum-

- well lasers using microwave modulation," Conference on Lasers and Electro-Optics, Anaheim, CA, June 2-7, 1996.
14. \*S. L. Chuang, C. S. Chang, J. Minch, and W. Fang, "Amplified spontaneous emission spectroscopy of strained quantum-well lasers-Theory and experiment," Optoelectronics'97 Symposium, San Jose, Feb. 1997. (Invited).
  15. W. Fang, S. L. Chuang, T. Tanbun-Ek, and Y. K. Chen, "Modeling and experiment of 1.55 $\mu$ m integrated electroabsorption modulator with distributed-feedback lasers," SPIE, vol. 3006, Edited by Y. S. Park and R. V. Ramaswamy, Photonics West, Optoelectronics'97 Symposium, San Jose, Feb. 1997.
  16. J. Minch, C. S. Chang, and S. L. Chuang, "Wavelength conversion using distributed-feedback lasers," Conference on Lasers and Electro-Optics, Baltimore, MD, May, 1997.
  17. J. Minch, C. S. Chang, and S. L. Chuang, "Wavelength conversion using two-pump four-wave mixing in a double-moded distributed-feedback laser," Laser and Electro-optics Society Annual Meeting, MN3, San Francisco, CA, Nov. 10-13, 1997.
  18. T. Keating, J. Minch, C. S. Chang, and S. L. Chuang, "Optimal refractive index changes for cross-gain modulation and cross-phase modulation," Photonics West, Physics and Simulation of Optoelectronic Devices VI, San Jose, CA, 1998.
  19. A. Hsu, W. Fang, S. L. Chuang, T. Tanbun-Ek, C. Bethea, and R. People "Integrated tunable laser with mode selection modulator," Photonics West, Optoelectronic Integrated Circuits II, SPIE, vol. 3290, Edited by S. Y. Wang and Y. S. Park, San Jose, CA, 1998.
  20. A. Hsu, W. Fang, and S. L. Chuang, "Modeling of normal and backward integrated electroabsorption modulator and laser," Integrated Photonic Research., Victoria, Canada, April 1998.
  21. \*S. L. Chuang, S. H. Park, J. Minch, and T. Keating, "Strained zinc-blende and wurtzite quantum-well lasers: theory and comparison with experiment," Semiconductor Science and Technology'98, La Jolla, CA, Sept. 1998.
  22. E. Young, J. Minch, and S. L. Chuang, "Polarization resolved four-wave mixing in a distributed-feedback laser," Photonics West, Physics and Simulation of Optoelectronic Devices VII, San Jose, CA, Jan. 1999.
  23. A. Hsu and S. L. Chuang, "Wavelength conversion by cross-absorption modulation using an integrated electroabsorption modulator / laser," Conference on Lasers and Electro-Optics, Baltimore, MD, May 1999.
  24. A. Hsu, S. L. Chuang, and T. Tanbun-Ek, "Multi-wavelength conversion in an integrated wavelength-tunable laser-modulator," Photonics West, OEIC IV, Proc. SPIE, Ed., Y. S. Park and R. T. Chen, vol. 3950, 2000 (in press).

\* invited talk

## ATTACHMENTS

Five major representative publications

# Theory and Experiment of $\text{In}_{1-x}\text{Ga}_x\text{As}_y\text{P}_{1-y}$ and $\text{In}_{1-x-y}\text{Ga}_x\text{Al}_y\text{As}$ Long-Wavelength Strained Quantum-Well Lasers

J. Minch, S. H. Park, T. Keating, and S. L. Chuang, *Fellow, IEEE*

**Abstract**—We present a comprehensive model for the calculation of the bandedge profile of both the  $\text{In}_{1-x}\text{Ga}_x\text{As}_y\text{P}_{1-y}$  and  $\text{In}_{1-x-y}\text{Ga}_x\text{Al}_y\text{As}$  quantum-well systems with an arbitrary composition. Using a many-body optical gain model, we compare the measured net modal gain for both material systems with calculations from the realistic band structure including valence band mixing effects. Calibrated measurements of the side light spontaneous emission spectrum based on its fundamental relation to the optical gain spectrum give values for the radiative current density. These measurements allow us to extract the relationship between total current density and carrier density. A fit of this relation yields values for the Auger coefficient for each material system.

**Index Terms**—Auger recombination, gain,  $\text{InGaAsP}$ ,  $\text{InGaAlAs}$ , semiconductor lasers, strained quantum-well lasers.

## I. INTRODUCTION

THERE are two main material systems used to fabricate long-wavelength semiconductor lasers. While the  $\text{In}_{1-x}\text{Ga}_x\text{As}_y\text{P}_{1-y}$  system has been firmly established as a candidate for high-performance lasers [1], [2], the  $\text{In}_{1-x-y}\text{Ga}_x\text{Al}_y\text{As}$  system has only recently begun to yield quality results [3]–[5]. The interest in the  $\text{In}_{1-x-y}\text{Ga}_x\text{Al}_y\text{As}$  system stems from its larger conduction band offset of  $\Delta E_c/\Delta E_g = 0.7$  compared to a value of  $\Delta E_c/\Delta E_g = 0.4$  for  $\text{In}_{1-x}\text{Ga}_x\text{As}_y\text{P}_{1-y}$ . This larger conduction band offset had been predicted to result in better electron confinement in the conduction band and, therefore, a higher temperature stability.

Previous reports have been given on the model for the band structure of these two systems [6], theoretical calculations comparing the systems in terms of threshold current density and differential gain [7], as well as the temperature dependence of the threshold current [8]. There have also been measurements of the contributions of the various recombination mechanisms for each system [9]. However, little has been published directly comparing the gain and

recombination mechanisms of these two systems, or comparing the existing many-body optical gain models with experimental measurements.

In this paper, we present a comprehensive model for the calculation of the band structure of samples made of either of these systems with an arbitrary composition. Then, using a many-body model for the optical gain and spontaneous emission, we compare the model to experimental data for each material system. Also, from simultaneous measurements of both the spontaneous emission spectrum from the side of the lasers and the gain spectrum from the facet emission, we are able to compare the relative contributions of the different recombination mechanisms in each laser system.

In Section II, we present our model for the calculation of the bandedge of each material system and the quantum-well (QW) band edge discontinuities, followed by the model for the optical gain and spontaneous emission. In Section III, we describe the structure of the lasers as well as our experimental measurements. Section IV describes the comparison of the optical gain data with calculations using our model, and the extraction of the relative contributions of the recombination mechanisms in each system. Finally, a brief conclusion is given in Section V.

## II. THEORETICAL MODEL

### A. Calculation of Bulk Bandgap with Strain

To obtain most parameters for both the  $\text{In}_{1-x}\text{Ga}_x\text{As}_y\text{P}_{1-y}$  and  $\text{In}_{1-x-y}\text{Ga}_x\text{Al}_y\text{As}$  material systems, a linear interpolation between the parameters of the relevant binary semiconductors is used. The interpolation formulas for all physical parameters  $P$  used in the calculation of the band edge, except for the bandgap, are given as [10], [11]

$$\begin{aligned} P(\text{In}_{1-x}\text{Ga}_x\text{As}_y\text{P}_{1-y}) \\ = P(\text{GaAs})xy + P(\text{GaP})x(1-y) + P(\text{InAs})(1-x)y \\ + P(\text{InP})(1-x)(1-y) \end{aligned} \quad (1)$$

$$\begin{aligned} P(\text{In}_{1-x-y}\text{Ga}_x\text{Al}_y\text{As}) \\ = P(\text{InAs})(1-x-y) + P(\text{GaAs})x + P(\text{AlAs})y. \end{aligned} \quad (2)$$

The material parameters of the binary semiconductors can be found in Table I.

The one exception to the linear interpolation is the formula for the unstrained bandgap. For each material system, this

Manuscript received July 27, 1998; revised December 1, 1998. This work was supported by the Office of Naval Research under Grant N00014-96-1-0303 and by AASERT under Grant N00014-96-1-0902. The work of S. H. Park was supported by the Catholic University of Taegu-Hyosung.

J. Minch, T. Keating, and S. L. Chuang are with the Department of Electrical and Computer Engineering, University of Illinois at Urbana-Champaign, Urbana, IL 61801 USA.

S. H. Park was with the Department of Electrical and Computer Engineering, University of Illinois at Urbana-Champaign, Urbana, IL 61801 USA. He is currently with the Department of Physics, Catholic University of Taegu-Hyosang, Hayang, Kyeonbuk, Korea.

Publisher Item Identifier S 0018-9197(99)03414-4.

TABLE I  
PARAMETERS FOR THE CALCULATION OF STRAIN AND BANDGAP ENERGY FOR THE  $\text{In}_{1-x}\text{Ga}_x\text{As}_y\text{P}_{1-y}$  AND  $\text{In}_{1-x-y}\text{Ga}_x\text{Al}_y\text{As}$  MATERIAL SYSTEMS [10], [11]

Parameter	Symbol(unit)	GaAs	InAs	InP	GaP	AlAs
Lattice Constant	$a(\text{\AA})$	5.6533	6.0584	5.8688	5.4505	5.660
Elastic Stiffness Constant	$C_{11}(10^{11}\text{dyn/cm}^2)$	11.879	8.329	10.11	14.05	12.5
Elastic Stiffness Constant	$C_{12}(10^{11}\text{dyn/cm}^2)$	5.376	4.526	5.61	6.203	5.34
Hydrostatic deformation potential						
for conduction band	$a_c(\text{eV})$	-7.17	-5.08	-5.04	-7.14	-5.64
for valence band	$a_v(\text{eV})$	1.16	1.00	1.27	1.70	2.47
Shear deformation potential						
for valence band	$b(\text{eV})$	-1.7	-1.8	-1.7	-1.8	-1.5
Valence band parameter	$\gamma_1$	6.8	20.4	4.95	4.05	3.45
	$\gamma_2$	1.9	8.3	1.65	0.49	0.68
	$\gamma_3$	2.73	9.1	2.35	1.25	1.29
Electron effective mass	$m_e/m_o$	0.067	0.023	0.077	0.25	0.15
Heavy-hole effective mass	$m_{hh}/m_o$	0.50	0.40	0.60	0.67	0.79

quantity is given as

$$\text{In}_{1-x}\text{Ga}_x\text{As}_y\text{P}_{1-y}$$

$$E_g(x, y) = 1.35 + 0.642x - 1.101y + 0.758x^2 + 0.101y^2 - 0.159xy - 0.28x^2y + 0.109xy^2 \text{ eV} \quad (3)$$

$$\text{In}_{1-x-y}\text{Ga}_x\text{Al}_y\text{As}$$

$$E_g(x, y) = 0.36 + 2.093y + 0.629x + 0.577y^2 + 0.436x^2 + 1.013xy - 2.0xy(1 - x - y) \text{ eV}. \quad (4)$$

The effects of strain are calculated in the following way. First, the strain in the plane of the epitaxial growth is

$$\epsilon = \epsilon_{xx} = \epsilon_{yy} = \frac{a_o - a}{a} \quad (5)$$

where  $a$  is the lattice constant of the quaternary epitaxial layer and  $a_o$  is the lattice constant of the substrate which is assumed to be InP. The strain in the perpendicular direction can be expressed as

$$\epsilon_{zz} = -2\frac{C_{12}}{C_{11}}\epsilon \quad (6)$$

where  $C_{11}$  and  $C_{12}$  are the elastic stiffness constants. The conduction band is shifted by the energy

$$\delta E_c(x, y) = a_c(\epsilon_{xx} + \epsilon_{yy} + \epsilon_{zz}) = 2a_c\left(1 - \frac{C_{12}}{C_{11}}\right)\epsilon \quad (7)$$

and the valence bands are shifted by

$$\delta E_{hh}(x, y) = -P_\epsilon - Q_\epsilon \quad (8)$$

$$\delta E_{lh}(x, y) = -P_\epsilon + Q_\epsilon \quad (9)$$

where

$$P_\epsilon = -a_v(\epsilon_{xx} + \epsilon_{yy} + \epsilon_{zz}) \quad (10)$$

$$= -2a_v\left(1 - \frac{C_{12}}{C_{11}}\right)\epsilon \quad (11)$$

$$Q_\epsilon = -\frac{b}{2}(\epsilon_{xx} + \epsilon_{yy} - 2\epsilon_{zz}) \quad (12)$$

$$= -b\left(1 + 2\frac{C_{12}}{C_{11}}\right)\epsilon \quad (13)$$

where  $a_c$  and  $a_v$  are the conduction-band and valence-band hydrostatic deformation potentials, and  $b$  is the valence-band shear deformation potential.

The strained bandgaps can then be expressed as

$$E_{c-hh}(x, y) = E_g(x, y) + \delta E_c(x, y) - \delta E_{hh}(x, y) \quad (14)$$

and

$$E_{c-lh}(x, y) = E_g(x, y) + \delta E_c(x, y) - \delta E_{lh}(x, y). \quad (15)$$

Fig. 1(a) shows a contour plot relating  $x$  and  $y$  to the strain and energy gap of the  $\text{In}_{1-x}\text{Ga}_x\text{As}_y\text{P}_{1-y}$  system grown on an InP substrate. Fig. 1(b) shows the same information, but inverted, so that, given a strain and a bandgap, the Ga and As mole fractions can be obtained. Fig. 2(a) and (b) shows the results for the  $\text{In}_{1-x-y}\text{Ga}_x\text{Al}_y\text{As}$  system with an InP substrate. In all of these figures, the bandgap with the smallest energy is presented (i.e.,  $c-hh$  for compressive strain,  $c-lh$  for tensile strain) and the bandgap shift due to the strain effects is taken into account. Note that these results are different from a conventional plot where the "unstrained" bandgap energy is usually presented.

#### B. Calculation of Band Offset

When modeling the bandstructure for a QW, the relative alignment of the band edges of the well and barrier material is very important. Unfortunately, there are few data for arbitrary compositions of these two quaternary material systems, especially for the strained cases. Here we present and compare two models for the band alignment of these systems.

1) *Model-Solid Theory* [10], [12]: The valence band position of a quaternary is given by

$$E_v(x, y) = \begin{cases} E_{v,av}(x, y) + \frac{\Delta(x, y)}{3} + \delta E_{hh}(x, y), \\ \text{for } hh \text{ (compressive strain)} \\ E_{v,av}(x, y) + \frac{\Delta(x, y)}{3} + \delta E_{lh}(x, y), \\ \text{for } lh \text{ (tensile strain)} \end{cases} \quad (16)$$



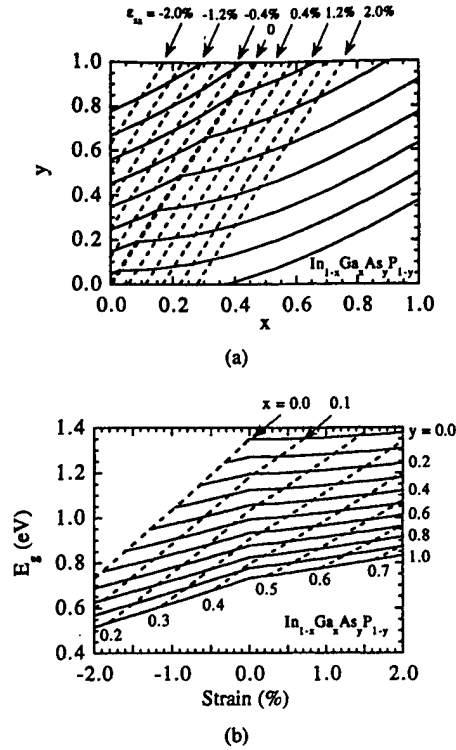


Fig. 1. Strain and strained bandgap energy versus Ga ( $x$ ) and As ( $y$ ) mole fractions for the  $\text{In}_{1-x}\text{Ga}_x\text{As}_y\text{P}_{1-y}$  material system with (a) contours of constant strain and bandgap energy and (b) contours of constant  $x$  and  $y$ .

where  $E_{v,av}(x, y)$  is the average valence subband energy and  $\Delta$  is the spin-orbit split-off band energy. These values are obtained by a linear interpolation [see (1) or (2)] of the binary values listed in Table II. The conduction band position may be calculated by simply adding the strained bandgap energy to the valence band position

$$E_c(x, y) = \begin{cases} E_v(x, y) + E_{c-hh}(x, y), & \text{for } hh \text{ (compressive strain)} \\ E_v(x, y) + E_{c-lh}(x, y), & \text{for } lh \text{ (tensile strain).} \end{cases} \quad (17)$$

The conduction band offset is given by

$$\frac{\Delta E_c}{\Delta E_g} = 1 - \frac{E_v^w - E_v^b}{E_g^w - E_g^b} \quad (18)$$

where  $E_v^w$  and  $E_v^b$  are the valence band positions in the well and barrier materials, respectively, and  $E_g^w$  and  $E_g^b$  are the strain adjusted band gaps ( $E_{c-hh}$  for compressive strain and  $E_{c-lh}$  for tensile strain) for the well and barrier materials.

2) *Harrison's Model* [13]: The position of both the conduction and valence bands are determined by

$$E_v(x, y) = \begin{cases} E_v^H(x, y) + \delta E_{hh}(x, y), & \text{for } hh \text{ (compressive strain)} \\ E_v^H(x, y) + \delta E_{lh}(x, y), & \text{for } lh \text{ (tensile strain)} \end{cases} \quad (19)$$

$$E_c(x, y) = E_c^H + \delta E_c(x, y) \quad (20)$$

where  $E_v^H(x, y)$  and  $E_c^H(x, y)$  are obtained by a linear interpolation of the binary parameters found in Table II, and  $\delta E_{hh}(x, y)$ ,  $\delta E_{lh}(x, y)$ , and  $\delta E_c(x, y)$  are the strain-induced

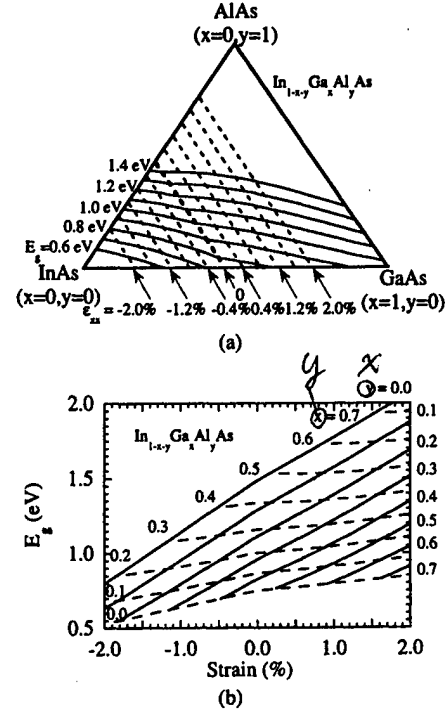


Fig. 2. Strain and strained bandgap energy versus Ga ( $x$ ) and Al ( $y$ ) mole fractions for the  $\text{In}_{1-x-y}\text{Ga}_x\text{Al}_y\text{As}$  material system with (a) contours of constant strain and bandgap energy and (b) contours of constant  $x$  and  $y$ .

energy shifts given in (7)–(9). The superscript “H” refers to Harrison’s model. The conduction band-edge discontinuity may then be calculated as

$$\frac{\Delta E_c}{\Delta E_g} = \frac{E_c^{H,b} - E_c^{H,w}}{(E_v^{H,w} - E_v^{H,b}) + (E_c^{H,b} - E_c^{H,w})} \quad (21)$$

where the superscripts  $w$  and  $b$  indicate the well and barrier materials, respectively.

It should be noted that this method simply is meant to give the parameter  $\Delta E_c/\Delta E_g$  which may be used to determine the alignment of the well and barrier materials. The difference between  $E_v(x, y)$  and  $E_c(x, y)$  from (19) and (20) should not be used to calculate the bandgap of the quaternary material. Rather, (3) and (4) should be used.

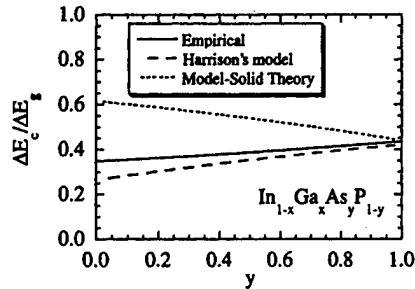
Fig. 3 shows a comparison of the model-solid theory and Harrison’s model for the calculation of the conduction band offset for both lattice-matched  $\text{In}_{1-x}\text{Ga}_x\text{As}_y\text{P}_{1-y}$  and  $\text{In}_{1-x-y}\text{Ga}_x\text{Al}_y\text{As}$ . Also shown are empirical curves (solid) based on experimental measurements of these quantities [14], [15]. For the  $\text{In}_{1-x}\text{Ga}_x\text{As}_y\text{P}_{1-y}$  system, Harrison’s model is excellent while the model-solid theory gives the opposite trend, only being good near the InGaAs boundary. For  $\text{In}_{1-x-y}\text{Ga}_x\text{Al}_y\text{As}$ , both models have some error, but Harrison’s model is again closer to the empirical curve. For the calculations of the band structure in this paper, we therefore have chosen to use Harrison’s model.

### C. Calculation of Band Structure and Gain

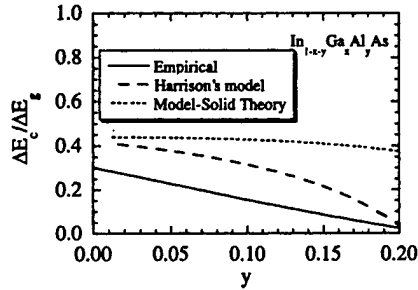
The optical gain with many-body effects is calculated by a non-Markovian model [16]. The plasma screening, bandgap renormalization (BGR), and the excitonic or the Coulomb enhancement (CE) of the interband transition probability are

TABLE II  
PARAMETERS FOR THE CALCULATION OF BAND ALIGNMENT OF THE  $\text{In}_{1-x}\text{Ga}_x\text{As}_y\text{P}_{1-y}$  AND  $\text{In}_{1-x-y}\text{Ga}_x\text{Al}_y\text{As}$  MATERIAL SYSTEMS USING THE MODEL-SOLID THEORY [12] AND HARRISON'S MODEL [13]

Parameter	Symbol(unit)	GaAs	InAs	InP	GaP	AlAs
Model-solid theory:						
Average valence band position	$E_{v,av}(\text{eV})$	-6.92	-6.67	-7.04	-7.40	-7.49
Spin-orbit split-off energy	$\Delta(\text{eV})$	0.34	0.38	0.11	0.08	0.28
Harrison's model:						
Conduction band position	$E_c^H(\text{eV})$	1.53	0.801	1.35	2.352	2.5255
Valence band position	$E_v^H(\text{eV})$	0.111	0.441	0.00	-0.388	-0.4245



(a)



(b)

Fig. 3. The conduction band offset for (a)  $\text{In}_{1-x}\text{Ga}_x\text{As}_y\text{P}_{1-y}$  and (b)  $\text{In}_{1-x-y}\text{Ga}_x\text{Al}_y\text{As}$  lattice-matched to InP. The solid lines show empirical results [14], [15] obtained from experimental data. Dashed lines show calculations using the model-solid theory and Harrison's model.

included in the model. The valence band structure is calculated by using the block-diagonalized  $3 \times 3$  Hamiltonian based on the  $k \cdot p$  method [17]. Aside from the conduction band effective mass for the  $\text{In}_{1-x}\text{Ga}_x\text{As}_y\text{P}_{1-y}$  system, parameters used in the calculation are interpolated using (1) and (2) and the binary parameters summarized in Table I. The conduction band effective mass for  $\text{In}_{1-x}\text{Ga}_x\text{As}_y\text{P}_{1-y}$  is given as

$$m_e(\text{In}_{1-x}\text{Ga}_x\text{As}_y\text{P}_{1-y}) = 0.08 - 0.116x + 0.026y - 0.059xy + (0.064 - 0.02x)y^2 + (0.06 + 0.032y)x^2. \quad (22)$$

The optical gain spectra are related to the spontaneous emission spectra from the detailed balance [18], [19] between absorption and emission of photons. This means that there is a transparency point in the gain spectra that is determined by the Fermi level separation  $\Delta F$  that suggests the carriers are in a quasi-equilibrium distribution. The following fundamental

relationship [18], [19] is then used to calculate the optical gain:

$$g(\omega) = \left[ 1 - \exp\left(\frac{\hbar\omega - \Delta F}{kT}\right) \right] g_{sp}(\omega) \quad (23)$$

$$g_{sp}(\omega) = \frac{\pi^2 c^2}{n^2 \omega^2} r_{sp}(\omega) \quad (24)$$

where  $\Delta F$  is the quasi-Fermi level separation,  $k$  is Boltzmann's constant,  $T$  is the device temperature,  $c$  is the speed of light,  $n$  is the effective refractive index of the optical waveguide mode, and  $r_{sp}(\omega)$  is the spontaneous emission rate. The spontaneous emission coefficient  $g_{sp}(\omega)$  taking into account the non-Markovian relaxation and the many-body effects is given by [16]

$$g_{sp}(\omega) = \sqrt{\frac{\mu_0}{\epsilon}} \left( \frac{e^2}{m_0^2 \omega} \right) \int_0^\infty dk_{\parallel} \frac{k_{\parallel}}{\pi L_z} |M_{lm}|^2 f_l^c(k_{\parallel}) \times (1 - f_m^v(k_{\parallel}))(1 - \text{Re } q_{k_{\parallel}}) \times \frac{\text{Re } L(E_{lm}(k_{\parallel})) - \text{Im } q_{k_{\parallel}} \text{Im } L(E_{lm}(k_{\parallel}))}{(1 - \text{Re } q_{k_{\parallel}})^2 + (\text{Im } q_{k_{\parallel}})^2} \quad (25)$$

where  $\omega$  is the angular frequency,  $\mu_0$  is the vacuum permeability,  $\epsilon$  is the dielectric constant,  $k_{\parallel}$  is the in-plane wavevector,  $L_z$  is the well thickness,  $|M_{lm}|^2$  is the momentum matrix element in the strained QW,  $f_l^c$  and  $f_m^v$  are the Fermi function for the conduction band states and the valence band states, and  $\hbar$  is the reduced Planck's constant. The indices  $l$  and  $m$  denote the electron states in the conduction band and the heavy hole (light hole) subband states in the valence band. Also,  $E_{lm}(k_{\parallel}) = E_l^c(k_{\parallel}) - E_m^v(k_{\parallel}) + E_g + \Delta E_{SX} + \Delta E_{CH} - \hbar\omega$  is the renormalized transition energy between electrons and holes, where  $E_g$  is the bandgap of the material, and  $\Delta E_{SX}$  and  $\Delta E_{CH}$  are the screened exchange and Coulomb-hole contributions [21] to the bandgap renormalization. The factor  $q_{k_{\parallel}}$  accounts for the excitonic or Coulomb enhancement of the interband transition probability [20], [21]. The lineshape function is Gaussian for the simplest non-Markovian quantum kinetics and is given by [16]

$$\text{Re } L(E_{lm}(k_{\parallel})) = \sqrt{\frac{\pi \tau_{in}(k_{\parallel}) \tau_c}{2\hbar^2}} \exp\left(-\frac{\tau_{in}(k_{\parallel}) \tau_c}{2\hbar^2} E_{lm}^2(k_{\parallel})\right) \quad (26)$$

$\int dE \Rightarrow \text{area} = \pi \cdot (\text{not one})$ .

TABLE III  
A SUMMARY OF THE STRUCTURE OF THE THREE LASER SYSTEMS STUDIED

Sample A	Well:	Number of wells	7	SCH width:	700Å
		Material	InGaAsP	Stripe width:	1.2μm
		Strain	-0.9% compressive	Cavity length:	350μm
		Width	80Å		
		PL wavelength	1.58μm		
	Barrier:	Material	InGaAsP		
		Strain	lattice matched		
		Width	80Å		
		PL wavelength	1.255μm		
Sample B	Well:	Number of wells	5	SCH width:	1000Å
		Material	InGaAlAs	Stripe width:	1.5μm
		Strain	-0.78% compressive	Cavity length:	890μm
		Width	54Å		
		PL wavelength	1.56μm		
	Barrier:	Material	InGaAlAs		
		Strain	lattice matched		
		Width	57Å		
		PL wavelength	1.21μm		
Sample C	Well:	Number of wells	5	SCH width:	600Å
		Material	InGaAlAs	Stripe width:	1.46μm
		Strain	lattice matched	Cavity length:	638μm
		Width	86Å		
		PL wavelength	1.56μm		
	Barrier:	Material	InGaAlAs		
		Strain	lattice matched		
		Width	50Å		
		PL wavelength	1.21μm		

and

$$\text{Im } L(E_{lm}(k_{\parallel})) = \frac{\tau_c}{\hbar} \int_0^{\infty} \exp\left(-\frac{\tau_c}{2\tau_{in}(k_{\parallel})} t^2\right) \cdot \sin\left(\frac{\tau_c E_{lm}(k_{\parallel})}{\hbar} t\right) dt. \quad (27)$$

The intraband relaxation time  $\tau_{in}$  and correlation time  $\tau_c$  are assumed to be constant and used as fitting parameters.

### III. EXPERIMENTS

#### A. Laser Structures

In our experiments, we perform measurements using lasers with three types of active regions. First, we tested a buried heterostructure laser with five lattice-matched QW's made of the  $\text{In}_{1-x-y}\text{Ga}_x\text{Al}_y\text{As}$  material system, as well as a buried heterostructure laser with five -0.78% compressively strained QW's of the same system [5]. Also tested was a buried heterostructure laser with seven -0.9% compressively strained QW's made of the  $\text{In}_{1-x}\text{Ga}_x\text{As}_y\text{P}_{1-y}$  material system.

Table III contains detailed information for the structure of each active region.

#### B. Experimental Procedure

The facet emission spectrum of each laser was measured for various currents below lasing threshold. The device under test is mounted on a heat sink and is held at a constant temperature of 25 °C using a thermoelectric cooling unit. The current to the device was supplied by an ILX Lightwave LDX-3412 current source and monitored to the hundredth of a milliamp using a Fluke 87 III digital multimeter. The facet output was collected using an E-TEK Dynamics laser optical fiber interface with a built-in polarizer to control the polarization of the measured emission. An optical isolator was used to prevent optical feedback effects and the light was monitored using an HP 70951B optical spectrum analyzer with a spectral resolution of 0.08 nm. The net modal gain for these devices was obtained using the well known Hakki-Paoli method [22] in which the ratio of the maximum  $I_{\max}$  and minimum  $I_{\min}$  of the amplified spontaneous emission spectrum yields the net

modal gain  $G_{\text{net}}$  by the following relations:

$$G_{\text{net}} = \Gamma g - \alpha_i = \frac{1}{L} \ln \left( \frac{S-1}{S+1} \right) + \frac{1}{2L} \ln \left( \frac{1}{R_1 R_2} \right) \quad (28)$$

$$S = \sqrt{\frac{I_{\text{max}}}{I_{\text{min}}}} \quad (29)$$

where  $g$  is the material gain for one well,  $\Gamma (=N_w \Gamma_w)$  is the optical confinement factor per well ( $\Gamma_w$ ) multiplied by  $N_w$ , the number of wells,  $\alpha_i$  is the intrinsic loss,  $L$  is the cavity length, and  $R_1$  and  $R_2$  are the facet power reflectivities.

The side light spontaneous emission [24] of the same device was also monitored for currents up to lasing threshold. In this measurement, a cleaved multimode fiber is brought up close to the side of the device, usually near the middle in order to avoid scattered light from the laser facets. First, using the same equipment as for the gain, the spontaneous emission spectrum is taken using a resolution bandwidth of 10 nm for each of the currents at which the facet emission was measured. Next, the current is controlled using an HP 4145 semiconductor parameter analyzer in order to achieve currents as low as 20  $\mu\text{A}$ . The current is swept and the light captured by the fiber is then fed into an HP 8153A Lightwave Multimeter to obtain the integrated spontaneous emission power. For these measurements, the width of the active region is sufficiently small (1.2–1.46  $\mu\text{m}$ ) so that amplification of the SE spectra is negligible.

#### IV. ANALYSIS AND DISCUSSION

The measured net modal gain obtained from the amplified spontaneous emission (ASE) spectrum using (28) for each of the three material systems studied is presented in Fig. 4 for several currents up to threshold. Typical mode spacings in the ASE spectrum for samples A, B, and C are about 0.93, 0.38, and 0.51 nm, respectively. To check for the effects of spectrometer resolution on the measured net modal gain, the min/sum method [23], which is less sensitive to the resolution limits of the measurement (although more sensitive to noise), was also used to extract the gain spectra. The resulting spectra were nearly identical except for values closest to the threshold gain value where the Hakki-Paoli method underestimates the gain, but these differences give less than a 5% error on the value of the modal gain.

Also presented in Fig. 4 are calculated spectra using the model presented above for the material gain of the three systems. The intraband relaxation time  $\tau_{\text{in}}$  and the correlation time  $\tau_c$  used for the fits are given in Table IV. For the screened exchange  $\Delta E_{\text{SX}}$  and Coulomb-hole  $\Delta E_{\text{CH}}$  contributions to the bandgap renormalization, [21, eqs. (27) and (28)] were used with a  $C$  parameter of 1.1, 1.7, and 2.0 for Samples A, B, and C, respectively. Each of these parameters affect the peak gain position and overall shape of the spectra. They were selected to yield the best overall fit, balancing these criteria. The net modal gain is obtained using an intrinsic loss which is independent of wavelength, and a confinement factor with a linear dependence on wavelength, with a slope equal to  $1.66 \times 10^{-4} \text{ nm}^{-1}$  (estimated from the wavelength-dependent refractive index and waveguide theory for the fundamental

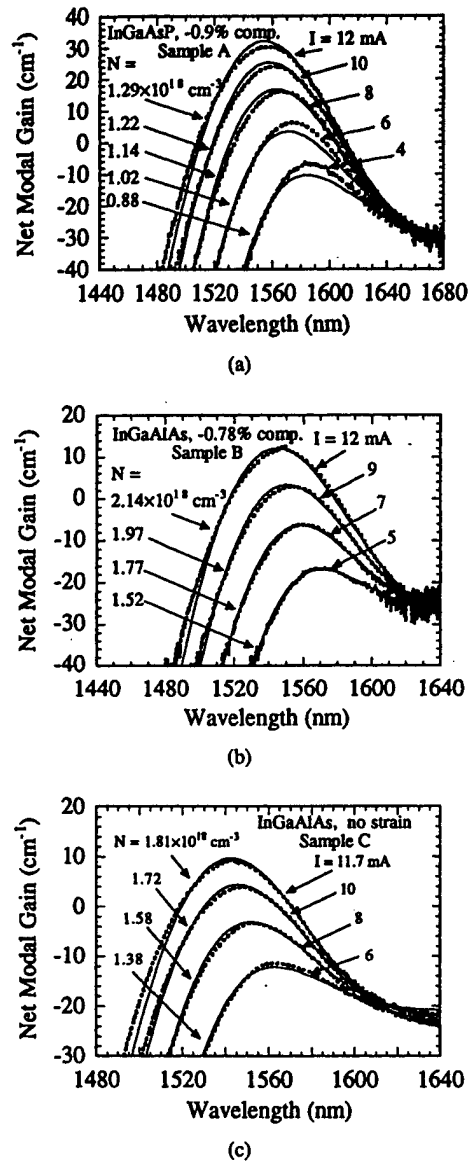


Fig. 4. The measured modal gain (solid lines) and calculated (dashed lines) values from the electronic band structure for (a)  $\text{In}_{1-x}\text{Ga}_x\text{As}_y\text{P}_{1-y}$  with  $-0.9\%$  compressive strain (Sample A), (b)  $\text{In}_{1-x-y}\text{Ga}_x\text{Al}_y\text{As}$  with  $-0.78\%$  compressive strain (Sample B), and (c)  $\text{In}_{1-x-y}\text{Ga}_x\text{Al}_y\text{As}$  lattice matched (Sample C). The device parameters are listed in Table III.

mode) and the vertical intercept treated as a parameter to fit the data.

Fig. 5(a) shows a plot of the fitted values of the intrinsic loss as a function of the injected current for each device. The observed increase in the loss is consistent with previous reports [25] and can be explained by the increase in free-carrier absorption with an increasing carrier density. The fitted optical confinement factor used for the three devices is shown in Fig. 5(b). Values for the optical confinement factor per well ( $\Gamma_w$ ) and the overall confinement factor ( $\Gamma = N_w \Gamma_w$ ) are listed in Table IV. These fitted values are in good agreement with typical values for InP-based lasers [26] when scaling due to well width is taken into account. Finally, Fig. 5(c) shows a plot of peak net modal gain versus the total current density for each laser system. The fits of the gain spectra of these three material systems allow us to obtain the density of carriers  $N$

TABLE IV  
PARAMETERS USED IN AND OBTAINED FROM THE THEORETICAL FITS

Parameter	Symbol	Sample A	Sample B	Sample C
Fit of the modal gain:				
Interband relaxation time	$\tau_{in}(fs)$	40	60	85
Correlation time	$\tau_c(fs)$	20	20	20
Quasi-Fermi level separation	$\Delta F(eV)$	0.801 (4mA)	0.804 (5mA)	0.806 (6mA)
		0.813 (6mA)	0.815 (7mA)	0.816 (8mA)
		0.822 (8mA)	0.823 (9mA)	0.823 (10mA)
		0.828 (10mA)	0.829 (12mA)	0.827 (11.7mA)
Transformation of spontaneous emission:				
Scaling coefficient	$Q(cm^{-1}nm^{-1}(mW)^{-1})$	$6.11 \times 10^{-7} \pm 0.22 \times 10^{-7}$	$1.81 \times 10^{-7} \pm 0.08 \times 10^{-7}$	$8.2 \times 10^{-8} \pm 0.02 \times 10^{-8}$
Effective index of refraction	$n$	$3.3 \pm 0.15$	$3.3 \pm 0.15$	$3.3 \pm 0.15$
Optical confinement factor	$\Gamma(=N_w\Gamma_w)$	$0.15 \pm 0.02$	$0.06 \pm 0.02$	$0.11 \pm 0.02$
Optical confinement factor per well	$\Gamma_w$	$0.021 \pm 0.0029$	$0.012 \pm 0.004$	$0.022 \pm 0.004$
Fit of the $J, N$ relationship:				
Coupling coefficient	$K_2$	$1.56 \times 10^{-14} \pm 0.01 \times 10^{-14}$	$1.64 \times 10^{-14} \pm 0.05 \times 10^{-14}$	$1.21 \times 10^{-14} \pm 0.01 \times 10^{-14}$
Monomolecular coefficient	$A(s^{-1})$	$1.1 \times 10^8 \pm 0.2 \times 10^8$	$7 \times 10^7 \pm 2 \times 10^7$	$6.7 \times 10^7 \pm 3 \times 10^7$
Auger coefficient	$C(cm^6s^{-1})$	$1.1 \times 10^{-27} \pm 0.15 \times 10^{-27}$	$1.4 \times 10^{-28} \pm 0.3 \times 10^{-28}$	$3 \times 10^{-28} \pm 2 \times 10^{-28}$
Injection efficiency	$\eta_{inj}$	$0.92 \pm 0.17$	$0.95 \pm 0.15$	$0.45 \pm 0.15$
Characteristic temperature (measured)	$T_0(^{\circ}K)$	38	53	51.4

in the QW's corresponding to the measured injection currents. For each system, other samples from the same wafer exhibit similar gain spectra.

The same model used to create the gain spectrum was also used to calculate the spontaneous emission rate for each of the material systems studied. The radiative current density can be related to the spontaneous emission rate as

$$J_{rad} = eN_w L_w \int_0^{\infty} r_{spont}(\lambda) d\lambda = eN_w L_w B_{eff} N^2 \quad (30)$$

where  $e$  is the charge on an electron,  $N_w$  is the number of wells,  $L_w$  is the width of a QW,  $r_{spont}(\lambda)$  is the spontaneous emission rate,  $B_{eff}$  is the effective radiative recombination coefficient, and  $N$  is the carrier density.  $J_{rad}$  can be obtained from our calculated spontaneous emission spectrum using (30) with

$$r_{spont}(\lambda) = \frac{8\pi c n^2}{\lambda^4} g_{sp}(\lambda) \quad (31)$$

where  $g_{sp}(\lambda)$  is given in (25),  $\lambda = 2\pi c/\omega$ ,  $c$  is the speed of light, and  $n$  is the refractive index of the QW. The calculated curves for  $J_{rad}$  of each sample are shown in Fig. 6.

In order to validate these calculations from the band structure, it is important to be able to obtain the radiative current density experimentally. As described above, we measure the spontaneous emission power spectra from the side of each laser device. The spontaneous emission power captured by the optical fiber can be related to the spontaneous emission rate by

$$P(\lambda) = K_1 \frac{hc}{\lambda} r_{spont}(\lambda) d\lambda V \quad (32)$$

where  $P(\lambda)$  is the measured power in the fiber,  $K_1$  is a coupling coefficient which includes the fraction of the spontaneous emission captured by the optical fiber,  $h$  is

Planck's constant,  $c$  is the speed of light,  $d\lambda$  is the spectrometer resolution, and  $V$  is the active region volume. Since  $K_1$  is an unknown quantity, it is not straightforward to obtain a value for the spontaneous emission rate so that (30) can be used to extract  $J_{rad}$ . A calibration can be accomplished based on the fundamental relationship between the material gain and the spontaneous emission rate [(23) and (24)], rewritten as

$$g(\lambda) = \frac{\lambda^4}{8\pi c n^2} \left[ 1 - \exp\left(\frac{hc/\lambda - \Delta F}{k_B T}\right) \right] r_{spont}(\lambda) \quad (33)$$

where  $n$  is the effective refractive index,  $\Delta F$  is the quasi-Fermi level separation energy,  $k_B$  is Boltzmann's constant, and  $T$  is the temperature. The material gain per well can be related to the measured net modal gain as

$$G_{net} = \Gamma g(\lambda) - \alpha_i \quad (34)$$

where  $\Gamma$  is the optical confinement factor and  $\alpha_i$  is the intrinsic loss for the optical waveguide mode. Combining (32)–(34), we obtain

$$G_{net}(\lambda) = Q \lambda^5 \left( 1 - \exp\left(\frac{hc/\lambda - \Delta F}{k_B T}\right) \right) P(\lambda) - \alpha_i \quad (35)$$

where

$$Q = \frac{\Gamma}{8\pi K_1 h c^2 n^2 d\lambda V} \quad (36)$$

This equation relates the measured net modal gain to the measured spontaneous emission power using the three parameters  $Q$ ,  $\Delta F$ , and  $\alpha_i$ .  $\Delta F$  and  $\alpha_i$  are not independent, however, since the net modal gain value measured at the wavelength corresponding to  $\Delta F$  is exactly the transparency level and equal to  $\alpha_i$ . (We assume here that the intrinsic loss is independent of wavelength.) Hence, the short-wavelength side

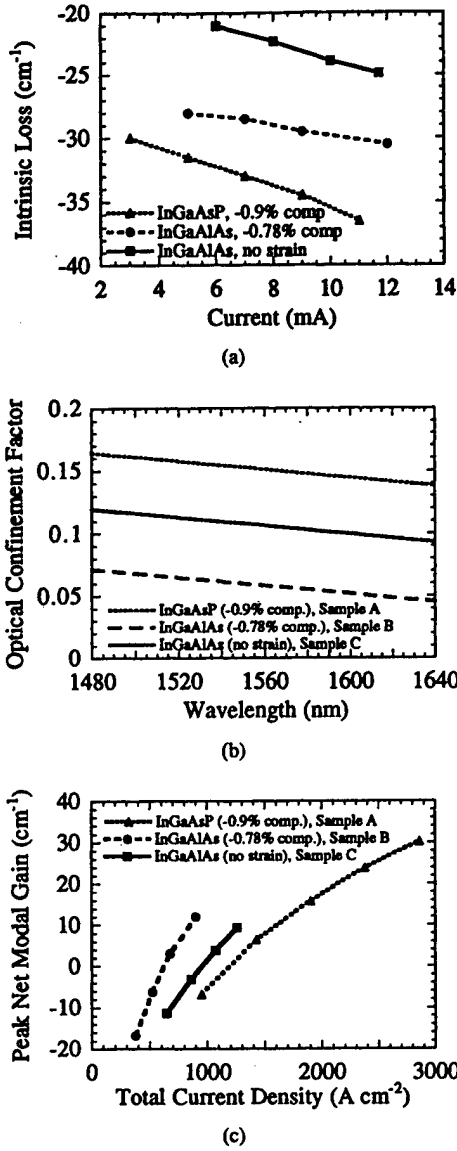


Fig. 5. (a) The optical confinement factor and (b) intrinsic loss used in the fits of the modal gain for Samples A, B, and C in Fig. 4. (c) The peak net modal gain versus the total current density.

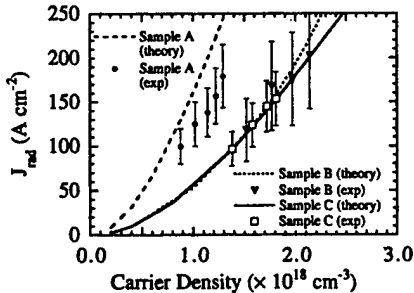


Fig. 6. The calculated total radiative current density through all wells [see (30)] as a function of carrier density (lines) compared to the extracted total radiative current density from the calibrated spontaneous emission spectrum measurements.

of the measured net modal gain spectrum gives the relationship between these two quantities.

Using  $Q$  and  $\Delta F$  as fitting parameters, (35) may then be used to transform the measured spontaneous emission power

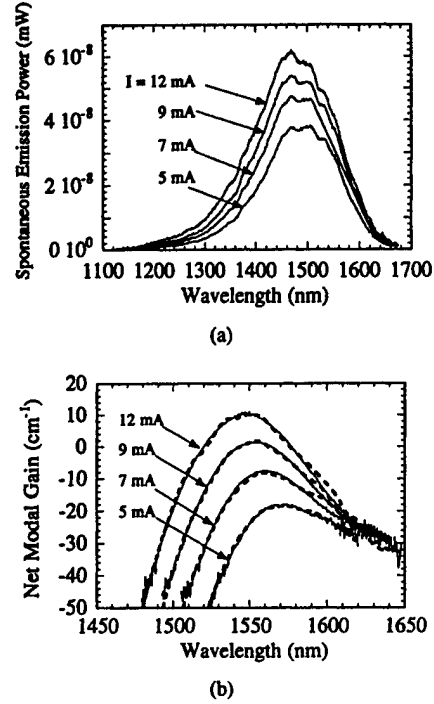


Fig. 7. (a) The measured spontaneous emission spectra for the -0.78% compressively strained  $\text{In}_{1-x-y}\text{Ga}_x\text{Al}_y\text{As}$  laser system (Sample B in Table III) and (b) the measured net modal gain spectra (solid lines) compared to the transformed spontaneous emission spectra (dashed lines) using (35).

into the net modal gain spectrum. By choosing the best fit between the measured and transformed net modal gains, an accurate value for  $Q$  can be obtained. As an example of this procedure, Fig. 7(a) shows the spontaneous emission power spectra measured for the compressively strained  $\text{In}_{1-x-y}\text{Ga}_x\text{Al}_y\text{As}$  system. These spectra were measured for each of the currents that the gain was measured at. The best fits between the transformed spontaneous emission and actually measured net modal gain spectra are shown in Fig. 7(b). The extracted values of  $Q$  are about  $1.8 \times 10^{-7}$  and vary by less than 4% among all of the currents measured, showing excellent uniformity in the measurement of the SE spectra. For  $\Delta F$ , the extracted values for each system deviate from the values obtained for the fitting of the experimental gain curves by less than 0.1% at low currents where the difference between two adjacent curves in Fig. 4 represent a shift of about 1% in  $\Delta F$ . At higher currents, the deviation gets as large as 0.45% while the separation between curves is about 0.5%.

Once accurate values of  $Q$  have been extracted, the measured spontaneous emission power spectra can be calibrated in the following way to get the actual spontaneous emission rate. By solving (32),  $r_{\text{spon}}(\lambda)$  can be expressed as

$$r_{\text{spon}}(\lambda) = T\lambda P(\lambda) \quad (37)$$

where

$$T = \frac{8\pi cn^2}{\Gamma} Q. \quad (38)$$

Note that this procedure has eliminated the need to derive the coupling coefficient  $K_1$  explicitly. The data points in Fig. 6 were obtained by substituting (37) and (38) into (30) and

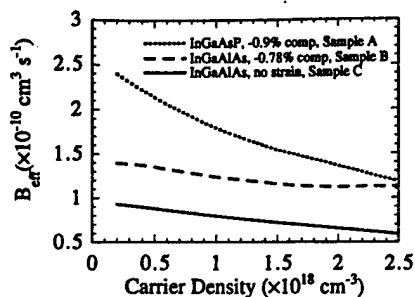


Fig. 8. The radiative recombination coefficient as a function of carrier density extracted from the calculated total radiative current density.

numerically integrating the calibrated data. The value for  $n$  was assumed to be 3.3 with an error of 0.15 for each of the material systems measured. The optical confinement factor was assumed to be constant with a value equal to the average of the range used for the gain fits, as shown in Fig. 5(b). The error range is taken from the values of the confinement factor in Fig. 5(b) at the edges of the transformed spontaneous emission spectra. This amounts to an error of about  $\pm 12\%$  for the value of the confinement factor, leading to a total error of slightly over  $\pm 20\%$  for the radiative current density.

From the calculated curves of the radiative current density  $J_{\text{rad}}$  as a function of carrier density  $N$  in Fig. 6, the radiative recombination coefficient  $B_{\text{eff}}$  for each material system is obtained from (30) and is presented in Fig. 8. This parameter is independent of the well width/number product, so it serves as a fair comparison of the relative probability of the radiative recombination of an electron-hole pair for each structure. We see that, at low carrier densities, the compressively strained  $\text{In}_{1-x}\text{Ga}_x\text{As}_y\text{P}_{1-y}$  system has the largest radiative recombination coefficient followed by the compressively strained  $\text{In}_{1-x-y}\text{Ga}_x\text{Al}_y\text{As}$  system and then the lattice-matched  $\text{In}_{1-x-y}\text{Ga}_x\text{Al}_y\text{As}$  system. It is not surprising that the strained samples are more efficient since strain has been shown to decrease the in-plane effective mass in the top ( $hh$ ) valence band, leading to a more symmetric injection of electrons and holes in the conduction and valence bands [27]. Also, the heavy-hole and light-hole subband separation becomes larger with strain, leading to less wasted carriers. At higher carrier densities, all three systems show a decrease in the radiative recombination coefficient. This is especially pronounced in the compressive  $\text{In}_{1-x}\text{Ga}_x\text{As}_y\text{P}_{1-y}$  system. This decrease is probably due to the significant population of higher energy valence subbands while the higher energy conduction subbands are virtually empty. For example, in all of these systems, the second conduction subband has less than 3% of the total carrier population. Meanwhile, for the compressive  $\text{In}_{1-x}\text{Ga}_x\text{As}_y\text{P}_{1-y}$  system, the first two heavy-hole subbands (which are the lowest subbands) have a spacing of 36 meV and a distribution of approximately 60.1% of carriers in the first heavy-hole subband and 29.6% in the second heavy-hole subband. Also, for the compressive  $\text{In}_{1-x-y}\text{Ga}_x\text{Al}_y\text{As}$  sample, there is a spacing of 65 meV between the first two heavy-hole subbands and a carrier distribution of about 80% and 19.4% for the first and second heavy-hole subbands, respectively. This difference is mostly due to the thinner

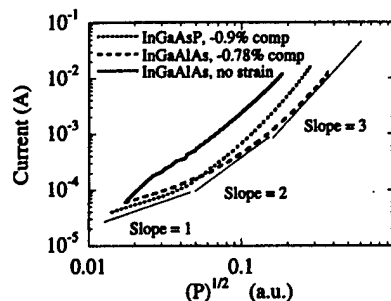


Fig. 9. The square root of the measured integrated spontaneous emission power  $\sqrt{P}$  (plotted along the  $x$  axis) versus the measured injection current along the vertical axis. The  $x$  axis is roughly proportional to carrier density, and the slope of the lines on the log-log plot give the power law for the injection current and carrier density relation.

well of the compressive  $\text{In}_{1-x-y}\text{Ga}_x\text{Al}_y\text{As}$  sample. Holes in the second heavy-hole subband are, therefore, unable to significantly contribute to radiative recombination processes since they can only recombine with electrons in the second conduction subband, which is sparsely populated for each laser system studied. The decrease seen in the compressive  $\text{In}_{1-x}\text{Ga}_x\text{As}_y\text{P}_{1-y}$  system is more significant due to the smaller spacing between valence subbands. At the higher carrier densities, this spacing leads to an even larger increase in the population of higher energy subbands, and thus more wasted carriers.

To study the major recombination mechanisms in each of these lasers, it is convenient to use the measured spontaneous power which has been monitored by an optical power meter. In this case, the data are easily measured over a large current range, and the photodetector performs the integration of the spontaneous emission power spectrum. Fig. 9 shows a log-log plot of the square root of spontaneous emission power versus the total injected current for each device studied. This format was chosen [28] to give an indication of the relative contributions of each recombination mechanism (monomolecular, radiative, and Auger). The value of the  $x$  axis can be expressed as

$$\sqrt{P} = K_2 \sqrt{B_{\text{eff}}} N \quad (39)$$

where  $K_2$  is another unknown coefficient which includes the fraction of spontaneous emission power captured by the optical fiber. We see that this is almost directly proportional to  $N$ , but not perfectly, due to the carrier dependence of  $B_{\text{eff}}$ , as discussed above. This deviation is relatively small, however, since we can see clear regions of slope one and slope three which correspond, respectively, to regimes where  $I$  is proportional to  $N$  (monomolecular mechanisms dominate) and  $N^3$  (where Auger mechanisms dominate). The region of slope two could indicate that the radiative processes are dominant, but this is not clear since there would be a point at which the slope is two due to the transition between the  $N$  and  $N^3$  regimes, even if radiative processes were missing. These issues will be clarified in the following analysis.

It is necessary to transform the measured data into a relationship between total current density and carrier density.

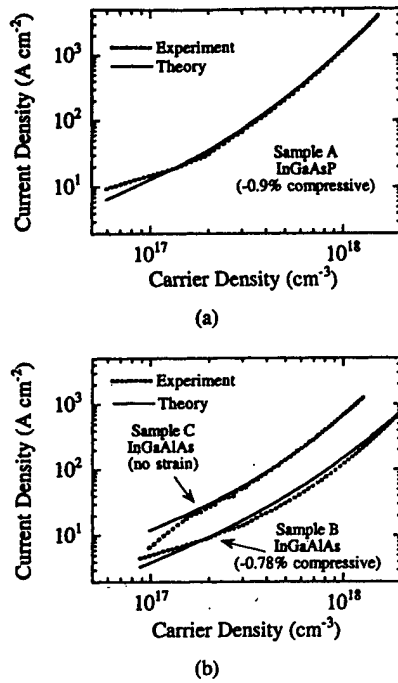


Fig. 10. The extracted current density/carrier density relation (dashed lines) as well as the best fits from the theory (solid lines) are shown for (a) the  $\text{In}_{1-x}\text{Ga}_x\text{As}_y\text{P}_{1-y}$  laser system (Sample A) and (b) the two  $\text{In}_{1-x-y}\text{Ga}_x\text{Al}_y\text{As}$  systems (Samples B and C).

Current density is easily obtained from the current as

$$J_{\text{tot}} = \frac{I}{wL} \quad (40)$$

where  $w$  is the stripe width and  $L$  is the cavity length. To obtain  $N$ , however, the unknown coefficient  $K_2$  must be determined. The fits of the net modal gain with our theory give a relation between  $I$  and  $N$  over a limited range of the measured data presently under consideration. Using the calculated dependence of  $B_{\text{eff}}$  on the carrier density for each system, and the measured  $\sqrt{P}$  value corresponding to the currents for the fitted gain data, (39) yields a value of  $K_2$  for each material system. The average between the values obtained for each of the  $I$ - $N$  pairs are used for our calculations and are listed in Table IV. All values are within 2% of the average value. Since  $K_2$  should be independent (for the most part) of injection current, it is fair to extrapolate the value of  $K_2$  from this small range of currents to the entire range of data under consideration. Using these  $K_2$  values and the calculated  $B_{\text{eff}}(N)$ , it is straightforward to obtain a value for  $N$  corresponding to the measured  $\sqrt{P}$  for each device.

The extracted relationships between  $J_{\text{tot}}$  and  $N$  are shown as dashed lines in Fig. 10(a) for the  $\text{In}_{1-x}\text{Ga}_x\text{As}_y\text{P}_{1-y}$  system and in Fig. 10(b) for the two  $\text{In}_{1-x-y}\text{Ga}_x\text{Al}_y\text{As}$  systems. The solid lines in these plots correspond to the best fit results using the relation

$$J_{\text{tot}} = \frac{eN_w L w}{\eta_{\text{inj}}} [AN + B_{\text{eff}}(N)N^2 + CN^3] \quad (41)$$

where  $\eta_{\text{inj}}$  is the injection efficiency accounting for the fraction of carriers which make it into the QW's,  $N_w$  is the number of wells,  $A$  is the monomolecular recombination coefficient,  $B_{\text{eff}}(N)$  is the calculated radiative recombination

coefficient, and  $C$  is the Auger recombination coefficient.  $A$  is a fitting parameter, but is only important for very low current densities. Its value is determined by fitting the behavior of the curve at these low current densities.  $\eta_{\text{inj}}$  and  $C$  are the major parameters which control the behavior of the curve. For a set value of  $\eta_{\text{inj}}$ , the penalty function for the fit is very sensitive to the  $C$  coefficient, so the value can be very well determined. However, a range of  $\eta_{\text{inj}}$  will give decent fits, so the extracted  $C$  value has some uncertainty. The best fit values of  $\eta_{\text{inj}}$ ,  $A$ , and  $C$  are presented in Table IV. The uncertainties on  $\eta_{\text{inj}}$  and  $C$  are determined by selecting those values which raise the penalty function 20% over the best fit value. The injection efficiency for the unstrained Sample C appears to have a relatively low injection efficiency.

It should be noted that previous measurements of the Auger coefficient in the  $\text{In}_{1-x}\text{Ga}_x\text{As}_y\text{P}_{1-y}$  material system have given values between  $2 \times 10^{-29} \text{ cm}^6 \text{ s}^{-1}$  and  $1 \times 10^{-28} \text{ cm}^6 \text{ s}^{-1}$  [29]–[31]. As discussed previously, the fact that a significant amount of holes occupy states where they may only recombine by nonradiative processes could explain why the extracted Auger coefficient for our sample is significantly higher than this range. This indicates that the Auger coefficient can be minimized by selecting the strain and well width to increase the separation of the valence subbands. For the  $\text{In}_{1-x-y}\text{Ga}_x\text{Al}_y\text{As}$  material system, a reported value of the Auger coefficient [9] is  $3.6 \times 10^{-29} \text{ cm}^6 \text{ s}^{-1}$  which is smaller than our value for the compressive sample. Our procedure, based on a comprehensive gain model and a fitting of the gain spectra to determine  $N$  and  $B_{\text{eff}}$ , should provide a reliable estimate of the  $C$  coefficient.

These extracted values are used in Fig. 11 to compare the relative contributions of  $J_{\text{mono}}$ ,  $J_{\text{rad}}$ , and  $J_{\text{Aug}}$  for the compressive  $\text{In}_{1-x-y}\text{Ga}_x\text{Al}_y\text{As}$  and compressive  $\text{In}_{1-x}\text{Ga}_x\text{As}_y\text{P}_{1-y}$  systems. Each device is dominated by the Auger recombination well before the laser reaches threshold. However, due to an Auger coefficient about 10 times larger, the Auger recombination dominates at a much lower point and becomes much larger in the  $\text{In}_{1-x}\text{Ga}_x\text{As}_y\text{P}_{1-y}$  system. This leads to a much larger threshold current density. The  $T_0$  for each of these lasers, measured from the shift in threshold over a temperature range from  $15^\circ$  to  $60^\circ$ , is also presented in Table IV. These relative values agree with the trend in the extracted Auger coefficients, indicating that Auger recombination is a major factor reducing  $T_0$  for these laser systems [28], [32]. Finally, it is interesting to note that the radiative current density never becomes the dominant recombination mechanism. At the injection level where Auger recombination becomes significant, the radiative current density is about the same as the monomolecular current density for each system studied.

## V. CONCLUSION

In this paper, we have presented a comprehensive model for the calculation of the band edges of both  $\text{In}_{1-x}\text{Ga}_x\text{As}_y\text{P}_{1-y}$  and  $\text{In}_{1-x-y}\text{Ga}_x\text{Al}_y\text{As}$  QW lasers with an arbitrary composition. Using a many-body optical gain model, we have compared the net modal gain for both material systems with



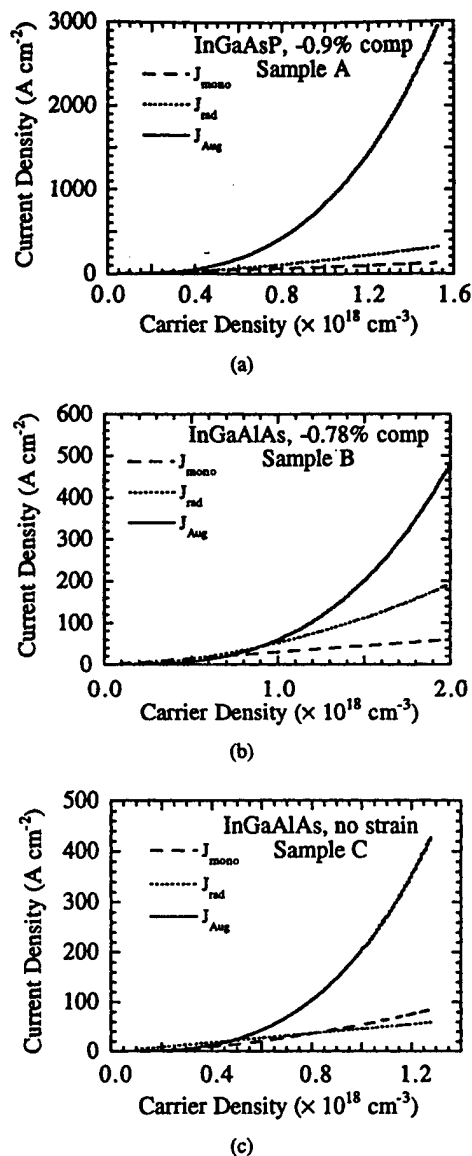


Fig. 11. The relative contributions of the monomolecular, radiative, and Auger recombination currents for (a)  $-0.9\%$  compressively strained  $\text{In}_{1-x}\text{Ga}_x\text{As}_y\text{P}_{1-y}$  (Sample A), (b)  $-0.78\%$  compressively strained  $\text{In}_{1-x-y}\text{Ga}_x\text{Al}_y\text{As}$  (Sample B), and (c) lattice-matched  $\text{In}_{1-x-y}\text{Ga}_x\text{Al}_y\text{As}$  (Sample C).

calculations from the realistic band structure. These comparisons allow us to obtain carrier densities for each of the measured currents. From a calibrated measurement of the spontaneous emission spectrum, we were able to obtain the radiative current density. These results are all in excellent agreement with our calculations. From a fit of the extracted relationship between carrier density and total current density, we were able to extract values for the Auger coefficient of each material system studied. The relative values of these parameters correspond very well with the observed temperature performance of each device.

From this study, it is difficult to make a strong statement as to which of the two material systems is superior. Obviously, more studies on a variety of active region designs would be needed to gauge all of the relevant factors and draw such a conclusion. Our measurements seem to indicate that the

$\text{InGaAlAs}$  system is at least as good as and probably better than the  $\text{InGaAsP}$  systems in terms of Auger recombination and temperature stability. Also, care should be taken to design the QW's such that there is a large separation between the lowest and highest level subbands, in order to reduce the carriers wasted by nonradiative recombination and to reduce the temperature sensitivity of the lasers.

#### ACKNOWLEDGMENT

The authors would like to thank Dr. T. Tanbun-Ek for providing devices for this study. They also wish to thank G. Liu and M. Silver for helpful discussions.

#### REFERENCES

- [1] P. J. A. Thijs, L. F. Tiemijer, P. I. Kuindersma, J. J. M. Binsma, and T. van Dongen, "High performance of  $1.5\ \mu\text{m}$  wavelength  $\text{InGaAs-InGaAsP}$  strained quantum-well lasers and amplifiers," *IEEE J. Quantum Electron.*, vol. 27, pp. 1426-1438, 1991.
- [2] P. J. A. Thijs, L. F. Tiemijer, J. J. M. Binsma, and T. van Dongen, "Progress in long-wavelength strained-layer  $\text{InGaAs(P)}$  quantum-well semiconductor lasers and amplifiers," *IEEE J. Quantum Electron.*, vol. 30, pp. 477-499, 1994.
- [3] M. Allovon and M. Quillec, "Interest in  $\text{AlGaInAs}$  on  $\text{InP}$  for optoelectronic applications," *Proc. Inst. Elect. Eng.*, vol. 139, pp. 148-152, 1992.
- [4] C. E. Zah, R. Bhat, B. Pathak, F. Favire, W. Lin, M. C. Wang, N. C. Andreadakis, D. M. Hwang, M. A. Koza, T. P. Lee, Z. Wang, D. Darby, D. Flanders, and J. J. Ssieh, "High performance uncooled  $1.3\ \mu\text{m}$   $\text{AlGaInAs/InP}$  strained-layer quantum well lasers for subscriber loop applications," *IEEE J. Quantum Electron.*, vol. 30, pp. 511-523, 1994.
- [5] T. Tanbun-Ek, S. N. G. Chu, P. W. Wisk, R. Pawelek, J. Minch, E. Young, and S. L. Chuang, "High performance buried heterostructure  $1.55\ \mu\text{m}$  wavelength  $\text{AlGaInAs/InP}$  multiple quantum well lasers grown entirely by MOVPE technique," *IEEE Photon. Technol. Lett.*, submitted for publication.
- [6] T. Ishikawa and J. Bowers, "Band lineup and In-plane effective mass of  $\text{InGaAsP}$  or  $\text{InGaAlAs}$  on  $\text{InP}$  strained-layer quantum well," *IEEE J. Quantum Electron.*, vol. 30, pp. 562-569, 1994.
- [7] O. Issanchou, J. Barrou, E. Idiart-Alhor, and M. Quillec, "Theoretical comparison of  $\text{GaInAs/GaAlInAs}$  and  $\text{GaInAs/GaInAsP}$  quantum-well lasers," *J. Appl. Phys.*, vol. 78, pp. 3925-3930, 1995.
- [8] J. Pan and J.-I. Chyi, "Theoretical study of the temperature dependence of  $1.3\ \mu\text{m}$   $\text{AlGaInAs-InP}$  multiple-quantum-well lasers," *IEEE J. Quantum Electron.*, vol. 32, pp. 2133-2138, 1996.
- [9] M. C. Wang, K. Kash, C. Zah, R. Bhat, and S. L. Chuang, "Measurement of nonradiative Auger and radiative recombination rates in strained-layer quantum-well systems," *Appl. Phys. Lett.*, vol. 62, pp. 166-168, 1993.
- [10] S. L. Chuang, *Physics of Optoelectronic Devices*. New York: Wiley, 1995.
- [11] K. H. Hellwege, Ed., *Landolt-Bornstein Numerical Data and Functional Relationships in Science and Technology*. Berlin, Germany: Springer, 1982, new series, group III, 17a; groups III-V 22a, Berlin: Springer, 1986.
- [12] C. G. Van der Walle, "Band lineups and deformation potentials in the model-solid theory," *Phys. Rev. B*, vol. 39, pp. 1871-1883, 1989.
- [13] W. A. Harrison, "Elementary theory of heterojunctions," *J. Vac. Sci. Technol.*, vol. 14, pp. 1016-1021, 1977.
- [14] J. Bohrer, A. Krost, and D. Bimberg, "Composition dependence of band gap and type of lineup in  $\text{InGaAlAs/InP}$  heterostructures," *Appl. Phys. Lett.*, vol. 63, pp. 1918-1920, 1993.
- [15] S. Adachi, *Physical Properties of III-V Semiconductor Compounds*. New York: Wiley, 1992.
- [16] D. Ahn, "Theory of non-Markovian optical gain in quantum well lasers," *Prog. Quantum Electron.*, vol. 21, pp. 249-287, 1997.
- [17] C. S. Chang and S. L. Chuang, "Modeling of strained quantum-well lasers with spin-orbit coupling," *IEEE J. Select. Topics Quantum Electron.*, vol. 1, pp. 218-229, 1995.
- [18] G. Lasher and F. Stern, "Spontaneous and stimulated recombination radiation in semiconductor," *Phys. Rev. A*, vol. 133, pp. 553-565, 1964.
- [19] C. S. Chang, S. L. Chuang, J. Minch, W. Fang, Y. K. Chen, and T. Tanbun-Ek, "Amplified spontaneous emission spectroscopy in strained

- quantum-well lasers," *IEEE J. Select. Topics Quantum Electron.*, vol. 1, pp. 1100-1107, 1995.
- [20] H. Haug and S. W. Koch, *Quantum Theory of the Optical and Electronic Properties of Semiconductors*. Singapore: World Scientific, 1993.
- [21] W. W. Chow, S. W. Koch, and M. Sargent III, *Semiconductor-Laser Physics*. Berlin, Germany: Springer, 1994, ch. 5.
- [22] B. W. Hakki and T. L. Paoli, "Gain spectra in GaAs double heterostructure injection lasers," *J. Appl. Phys.*, vol. 46, pp. 1299-1306, 1975.
- [23] D. T. Cassidy, "Technique for measurement of the gain spectra of semiconductor diode lasers," *J. Appl. Phys.*, vol. 56, pp. 3096-3099, 1984.
- [24] W. Fang, M. Hattendorf, S. L. Chuang, J. Minch, C. S. Chang, C. G. Bethea, and Y. K. Chen, "Analysis of temperature sensitivity in semiconductor lasers using gain and spontaneous emission measurements," *Appl. Phys. Lett.*, vol. 70, pp. 796-798, 1997.
- [25] G. E. Shtengel, P. A. Morton, R. F. Kazarinov, D. A. Ackerman, M. S. Hybertsen, G. L. Belenky, and C. L. Reynolds, Jr., "Experimental study of physical parameters of semiconductor lasers," *Proc. SPIE*, vol. 2994, pp. 678-689, 1997.
- [26] J. P. Loehr and J. Singh, "Theoretical studies of the effect of strain on the performance of strained quantum-well lasers based on GaAs and InP technology," *IEEE J. Quantum Electron.*, vol. 27, pp. 708-716, 1991.
- [27] E. Yablonovitch and E. O. Kane, "Band structure engineering of semiconductor lasers for optical communications," *J. Lightwave Technol.*, vol. 6, pp. 1292-1299, 1988.
- [28] S. J. Sweeney, A. F. Phillips, A. R. Adams, E. P. O'Reilly, and P. J. A. Thijs, "The effect of temperature dependent processes on the performance of 1.5  $\mu\text{m}$  compressively strained InGaAs(P) MQW semiconductor diode lasers," *IEEE Photon. Technol. Lett.*, vol. 10, pp. 1076-1078, 1998.
- [29] R. Olshansky, C. B. Su, J. Manning, and W. Powazinik, "Temperature sensitivity and high temperature operation of long wavelength semiconductor lasers," *IEEE J. Quantum Electron.*, vol. QE-20, pp. 838-854, 1984.
- [30] Y. Zou, J. S. Osinski, P. Grodzinski, P. D. Dapkus, W. Rideout, W. F. Sharfin, J. Schlafer, and F. D. Crawford, "Experimental study of Auger recombination, gain, and temperature sensitivity of 1.5  $\mu\text{m}$  compressively strained semiconductor lasers," *IEEE J. Quantum Electron.*, vol. 29, pp. 1565-1575, 1993.
- [31] G. Agrawal and N. K. Dutta, *Semiconductor Lasers*, 2nd ed. New York: Van Nostrand Reinhold, 1993.
- [32] E. P. O'Reilly and M. Silver, "Temperature sensitivity and high temperature operation of long wavelength semiconductor lasers," *Appl. Phys. Lett.*, vol. 63, pp. 3318-3320, 1993.
- J. Minch, photograph and biography not available at the time of publication.
- S. H. Park, photograph and biography not available at the time of publication.
- T. Keating, photograph and biography not available at the time of publication.
- S. L. Chuang (S'78-M'82-SM'88-F'97), photograph and biography not available at the time of publication.

# A Wavelength-Tunable Curved Waveguide DFB Laser with an Integrated Modulator

Alan Hsu, Shun-Lien Chuang, *Fellow, IEEE*, W. Fang, L. Adams, G. Nykolak, and T. Tanbun-Ek

**Abstract**—A distributed-feedback (DFB) laser with a curved waveguide in the active region integrated with an electroabsorption modulator is studied experimentally and theoretically. The modulator controls the lasing wavelength of the DFB laser by acting as an optical phase shifter. Our model, which is based on the transfer matrix method, is used to simulate this multisection device with the curved waveguide, self-consistently including the effects of spatial hole burning (SHB). The model explains the features and wavelength-tuning behavior of the spectrum and shows good agreement with experimentally measured spectra. We also show theoretically that the curved waveguide suppresses the longitudinal photon density profile of the device compared with a straight waveguide case, which implies reduced SHB effects.

**Index Terms**—Curved waveguide, distributed feedback, modulator, spatial hole burning, wavelength-tunable.

## I. INTRODUCTION

THE STUDY OF wavelength-tunable laser sources is an important topic of research, emphasized by the rapidly expanding development of wavelength-division-multiplexed (WDM) optical communications systems, which can presently transmit data at rates of over 1 Tb/s over a single optical fiber.

Research in multisection wavelength-tunable lasers has been investigated extensively for use in WDM and coherent optical communications systems, and some of the progress in this field is well summarized in [1] and [2]. Originally, the goal of developing distributed-feedback (DFB) lasers integrated with electroabsorption modulators was to improve high-speed performance by reducing frequency chirping of DFB lasers by external modulation [3]–[9]. Recently, these devices have also been used as wavelength-tunable sources [10], [11]. The use of a chirped grating pitch [12]–[14] has been investigated as a way to achieve a distributed phase shift in the grating. Several groups have implemented this chirped grating pitch using a bent or curved waveguide to achieve wavelength tuning or high-power operation and have shown promising results

[15]–[17]. In previous work, we have modeled a DFB laser and an integrated electroabsorption modulator–laser (EML) using the transfer matrix method [18], [19]. Multisection DFB lasers have been modeled using a transmission-line model as well [20].

The wavelength-tunable laser studied here, a possible candidate for WDM systems, consists of a DFB laser with a curved waveguide, integrated with an electroabsorption modulator which acts as a wavelength-tuning section. The structure for this device is identical to that of an integrated EML with the exception that the facet coatings on the laser and modulator are opposite to those of the conventional EML. A voltage bias applied to the modulator effectively controls the lasing wavelength of the DFB laser. Previously reported results for this device have shown a wavelength-tuning range of 3.5 nm and high-speed optical packet switching over four wavelength channels at a rate of 2.5 Gb/s [11].

The purpose of this work is to model this wavelength-tunable multisection device, including spatial hole burning (SHB) effects self-consistently, and to explain the characteristics of the spectrum and the wavelength-tuning behavior of this device by showing good agreement between theory and experiment. We first describe the device structure in Section II. In Section III, we explain our model based on the transfer matrix method that includes SHB effects. In Section IV, we compare measured spectrum with theory and explain the spectral features of this wavelength-tunable laser. This includes explanations for the wavelength-tuning behavior of this device as a function of modulator voltage and theoretical results which show SHB suppression due to the use of a curved waveguide. In Section V, we summarize our work and present our conclusions.

## II. DEVICE STRUCTURE

A schematic of the wavelength-tunable laser, which consists of a DFB laser with a curved waveguide integrated with an electroabsorption modulator separated by an isolation region, is shown in Fig. 1. The length of the DFB section is 300  $\mu\text{m}$ , the isolation region is about 80  $\mu\text{m}$ , and the modulator is 250  $\mu\text{m}$ . The facet reflectivity at the high-reflection (HR)-coated facet on the modulator side is 99%, and the antireflection (AR)-coated facet reflectivity on the DFB laser side is estimated to be 1% using a 50- $\mu\text{m}$  window structure on the AR side of the DFB section. The shape of this curved waveguide has been modeled previously as a raised sine shape [11]. However, this waveguide can also be modeled as an S-bend shape which has more flexible parameters and provides a more general

Manuscript received October 12, 1998; revised March 5, 1999. This work was supported by the Office of Naval Research under Grant N00014-96-1-0303 and Grant N00014-96-1-0902.

A. Hsu and S.-L. Chuang are with the Department of Electrical and Computer Engineering, University of Illinois at Urbana-Champaign, Urbana, IL 61801 USA.

W. Fang was with the Department of Electrical and Computer Engineering, University of Illinois at Urbana-Champaign, Urbana, IL 61801 USA. He is now with Bell Laboratories, Lucent Technologies, Holmdel, NJ 07733 USA.

L. Adams and G. Nykolak are with Bell Laboratories, Lucent Technologies, Murray Hill, NJ 07974 USA.

T. Tanbun-Ek was with Bell Laboratories, Lucent Technologies, Murray Hill, NJ 07974 USA. He is now with Multiplex, South Plainfield, NJ 07080 USA.

Publisher Item Identifier S 0018-9197(99)04117-2.

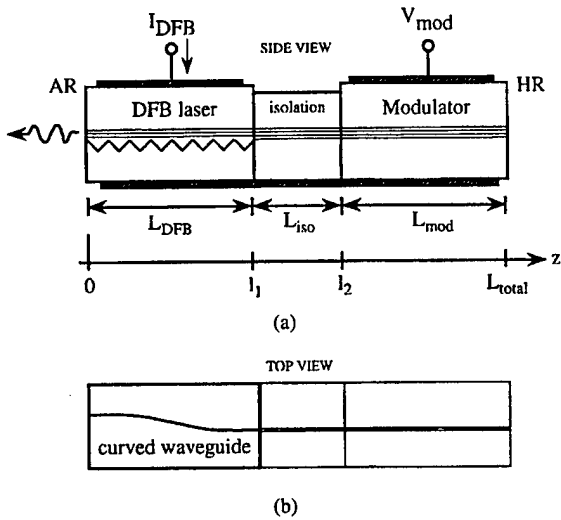


Fig. 1. (a) A side-view schematic of the two-section wavelength-tunable laser which consists of a DFB laser section at the AR side and a modulator at the HR side of the device which tunes the lasing wavelength.  $L_{total}$  is the length of the entire device,  $L_{DFB}$ ,  $L_{iso}$ , and  $L_{mod}$  are the lengths of the DFB laser, isolation, and modulator sections, respectively,  $l_1 = L_{DFB}$ , and  $l_2 = L_{DFB} + L_{iso}$ . (b) A top-view schematic illustrating the curved waveguide of the DFB laser section.

waveguide shape. The shape of the S-bend curved waveguide is given by the following equations [16]:

$$\begin{aligned} y(z) &= 2W, & \text{for } 0 \leq z \leq L_1 \\ y(z) &= 2W + \frac{W}{L_B} (L_1 - z) + \frac{W}{\pi} \sin\left(\pi \frac{z - L_1}{L_B}\right), & \text{for } L_1 \leq z \leq L_1 + 2L_B \\ y(z) &= 0, & \text{for } L_1 + 2L_B \leq z \leq L \end{aligned} \quad (1)$$

where  $L$  is the total length,  $L_1$  is the length of the straight section before the S-bend,  $L_B$  is equal to half of the length of the S-bend region, and  $W$  is the width of half of the S-bend. For this device, we estimated the S-bend parameters to be  $L = 360 \mu\text{m}$ ,  $L_1 = 47 \mu\text{m}$ ,  $L_B = 133 \mu\text{m}$ , and  $W = 10 \mu\text{m}$ .

In both devices, the active region in the DFB and the modulator sections consist of seven layers of compressively strained InGaAsP QW's and were fabricated using a selective-area metal-organic vapor phase epitaxy (MOVPE) technique. The DFB region has an estimated compressive strain of at least  $-1\%$  while the compressive strain in the modulator was measured to be about  $-0.5\%$ . The peak wavelength of the photoluminescence was measured at  $1.4891 \mu\text{m}$ . The isolation region between the DFB and modulator sections was created by shallow trenching a depth of about  $0.7 \mu\text{m}$  to yield an electrical isolation with a typical value greater than  $50 \text{ k}\Omega$ .

### III. THEORY

#### A. Longitudinal Fields in a Multisection Device

We model the longitudinal properties of the optical fields in the curved waveguide DFB laser with integrated modulator and isolation sections using the transfer matrix method. Most of the development of the transfer matrix method used in our model can be found in [18] and [19].

The laser, isolation, and modulator sections can each be represented by the transfer matrices  $\bar{F}^{DFB}$ ,  $\bar{F}^{isol}$ , and  $\bar{F}^{mod}$ , respectively, which gives the slowly varying amplitudes of the forward and backward propagating waves  $A(z)$  and  $B(z)$ , respectively, in each section. The elements of these matrices are given by [18], [19]

$$F_{11}(l) = \frac{1}{1 - r_p r_m} (e^{iq l} - r_p r_m e^{-iq l}) \quad (2)$$

$$F_{12}(l) = \frac{-r_m}{1 - r_p r_m} (e^{iq l} - e^{-iq l}) \quad (3)$$

$$F_{21}(l) = \frac{r_p}{1 - r_p r_m} (e^{iq l} - e^{-iq l}) \quad (4)$$

$$F_{22}(l) = \frac{1}{1 - r_p r_m} (-r_p r_m e^{iq l} + e^{-iq l}) \quad (5)$$

where

$$q = \sqrt{(\Delta\beta)^2 + \kappa_{ab}\kappa_{ba}} \quad (6)$$

and

$$r_p = \frac{\kappa_{ba}}{\Delta\beta + q} \quad (7)$$

$$r_m = \frac{-\kappa_{ab}}{\Delta\beta + q} \quad (8)$$

where  $\beta = 2\pi n_e(\lambda)/\lambda$  is the propagation constant where  $n_e$  is the effective index of the fundamental guided mode,  $\beta_0 = \pi/\Lambda$  where  $\Lambda$  is the grating pitch, and the detuning parameter  $\Delta\beta = \beta - \beta_0$ .

The interface between sections which includes differences in refractive index between each section is also represented by a transfer matrix  $\bar{T}^{int}$  and is derived from the boundary conditions that tangential electrical and magnetic fields are continuous at the interface at a given  $z = l_1$  or  $l_2$ , given by

$$\begin{bmatrix} A(l^+) \\ B(l^+) \end{bmatrix} = \bar{T}^{int}(l) \begin{bmatrix} A(l^-) \\ B(l^-) \end{bmatrix}. \quad (9)$$

The forward and backward propagating waves in the whole device can be modeled by multiplying the matrices for each section and interface together as given by

$$\begin{bmatrix} A(L_{total}) \\ B(L_{total}) \end{bmatrix} = \left[ \bar{F}^{mod}(L_{mod}) \right] \left[ \bar{T}^{int}(l_2) \right] \left[ \bar{F}^{isol}(L_{iso}) \right] \cdot \left[ \bar{T}^{int}(l_1) \right] \left[ \bar{F}^{DFB}(L_{DFB}) \right] \begin{bmatrix} A(0) \\ B(0) \end{bmatrix} \quad (10)$$

where  $L_{total}$  is the length of the entire device,  $L_{DFB}$ ,  $L_{iso}$ , and  $L_{mod}$  are the lengths of the DFB laser, isolation, and modulator sections, respectively, and  $l_i$  is the location of section  $i$ , where  $l_1 = L_{DFB}$ ,  $l_2 = L_{DFB} + L_{iso}$ , as shown in Fig. 1.

We model the amplified spontaneous emission spectrum for the integrated device by including an equivalent spontaneous emission source [21] into the transfer matrix method. We place an equivalent spontaneous-emission surface current density  $J_s$  at a position  $z_s$  in the (active) DFB section of the cavity and solve the boundary conditions for the electric and magnetic fields on either side of the current sheet. From this, we obtain

the relation between the field amplitudes near the source position

$$\begin{bmatrix} A^+(z_s) \\ B^+(z_s) \end{bmatrix} - \begin{bmatrix} A^-(z_s) \\ B^-(z_s) \end{bmatrix} = \bar{M}^{-1} \begin{bmatrix} 0 \\ \omega \mu J_s \end{bmatrix} = \begin{bmatrix} s_{21} \\ s_{22} \end{bmatrix} \quad (11)$$

where

$$\bar{M} = \begin{bmatrix} e^{i\beta_0 z_s} & e^{-i\beta_0 z_s} \\ \beta e^{i\beta_0 z_s} + \kappa_{ba} e^{-i\beta_0 z_s} & \kappa_{ab} e^{i\beta_0 z_s} - \beta e^{-i\beta_0 z_s} \end{bmatrix} \quad (12)$$

where  $\kappa_{ab}$  and  $\kappa_{ba}$  are the coupling coefficients used in the coupled-mode equations [19]. Next, we match boundary conditions at the facets and obtain

$$\begin{bmatrix} A(L_{\text{total}}) \\ B(0) \end{bmatrix} = \bar{D}^{-1} \bar{F}(L_{\text{total}} - z_s) \begin{bmatrix} s_{21} \\ s_{22} \end{bmatrix} \quad (13)$$

where the matrix  $D$  contains the boundary condition information at the facets

$$\bar{D} = \begin{bmatrix} 1 & -r_1 F_{11}(L_{\text{total}}) - F_{12}(L_{\text{total}}) \\ r_2 & -r_1 F_{21}(L_{\text{total}}) - F_{22}(L_{\text{total}}) \end{bmatrix} \quad (14)$$

and  $r_1$  and  $r_2$  are the complex reflectivities at the facets. The matrix  $\bar{F}(L_{\text{total}})$  is the product of all the transfer matrices in (10), and it describes the total three-section device whereas the matrix  $\bar{F}(L_{\text{total}} - z_s)$  contains only those matrices between  $z_s$  and  $L_{\text{total}}$ .

The amplified spontaneous emission intensity from each facet is obtained by summing the square of the electric field envelopes  $B(0)$  and  $A(L)$  due to a single source at  $z_s$  over all the sources  $J_s$  within the cavity ( $0 \leq z_s \leq L$ ) as given by

$$I_{\text{left}} = (1 - |r_1|^2) \int_0^L |B(0)|^2 dz_s \quad (15)$$

$$I_{\text{right}} = (1 - |r_2|^2) \int_0^L |A(L)|^2 dz_s. \quad (16)$$

The ASE is calculated using (15) and (16) for each wavelength to get the entire ASE spectrum.

The photon density profile is obtained from the electric field envelopes using

$$S(z) \propto |A(z)|^2 + |B(z)|^2. \quad (17)$$

Again, the total photon density is found by summing the photon density  $S(z)$  due to a single source at  $z_s$  over all the sources  $J_s$  within the cavity.

### B. Spatial Hole Burning

In the first iteration of the photon density calculation, the gain and carrier density profiles along the device are considered uniform. If the applied injection current is above threshold, the calculated photon density profile will be perturbed as a function of longitudinal cavity position and therefore not constant. The carrier density and gain are recalculated using the carrier density rate equation at steady state given by

$$\frac{dN}{dt} = \frac{I}{eV} - AN - BN^2 - CN^3 - v_g g(N) S \quad (18)$$

where  $I$  is the injected current,  $e$  is the electron unit charge,  $V$  is the volume of the laser active region,  $A$  is the monocarrier

lifetime coefficient,  $B$  is the bimolecular carrier recombination coefficient,  $C$  is the Auger recombination coefficient,  $v_g$  is the group velocity,  $g(N)$  is the material gain as a function of carrier density  $N$ , and  $S$  is the photon density. In the model, we consider a linearized material gain given by  $g(N) = g'(N - N_0)$ , where  $g'$  is the differential gain and  $N_0$  is the carrier density at transparency. This results in a nonuniform carrier density and profile. The refractive index profile also becomes nonuniform due to the perturbed carrier density profile through the relation

$$\Delta n_e = -\frac{\lambda \alpha_e g'}{4\pi} \Delta N \quad (19)$$

where  $\Delta n_e$  is the change in effective index,  $\lambda$  is the wavelength,  $\alpha_e$  is the linewidth enhancement factor, and  $g'$  is the differential gain. This change in refractive index to a nonuniform carrier density profile changes the threshold gain of potential lasing modes and accounts for the decrease in the sidemode suppression ratio and mode hopping associated with SHB. The photon density and carrier density are continually recalculated using (18) until a self-consistent solution is found. Only a single longitudinal mode is taken into account. Our model has been applied to the study of SHB in conventional DFB lasers with excellent agreement with experimental data [19]. It should be noted that each section of the device is further subdivided into multiple sections, and the coupled-mode equations are used to derive the transfer matrices to account for the spatially dependent refractive index and gain profiles and the grating pitch parameter.

### C. Curved Waveguide and Dispersion

The curved waveguide in the DFB laser section induces an effective variation in grating pitch  $\Lambda_{\text{eff}}$  as a function of longitudinal position and is included by [11]

$$\Lambda_{\text{eff}} = \frac{\Lambda_0}{\cos \phi(z)} \quad (20)$$

$$\phi(z) = \tan^{-1} \frac{y(z)}{z} \quad (21)$$

where  $y$  and  $z$  are defined in (1), and  $\Lambda_0$  is the grating pitch for the straight waveguide case.  $\Lambda_{\text{eff}}$  is taken into account in the model through the propagation constant  $\beta_o = \pi/\Lambda_{\text{eff}}$ , whereas in our previous work [19]  $\beta_o = \pi/\Lambda_0$ . In addition, the use of a curved waveguide slightly increases the effective length of the waveguide in the DFB laser section through which the fields propagate. This is taken into account in the model.

The effects of dispersion are also considered in the model. Over a narrow range of  $\lambda$  near a reference wavelength  $\lambda_0$ , the effective index  $n_e(\lambda)$  can be approximated by a linear function of  $\lambda$

$$n_e(\lambda) = n_e(\lambda_0) - s(\lambda - \lambda_0) \quad (22)$$

where the slope  $s$  is

$$s = \frac{(n_g - n_e(\lambda_0))}{\lambda_0} \quad (23)$$

and  $n_g$  is the group index, which can be approximated as a constant within the wavelength range of interest. We estimate

the group refractive index from the mode spacing outside the stopband in the experimental spectrum, and the value of  $s$  is estimated using previous experimental results [21] for the InGaAsP system. We then calculate  $n_e(\lambda_0)$  and solve for  $n_e(\lambda)$  using (22) over the wavelengths of interest.

#### D. Voltage-Dependent Refractive Index and Gain in the Electroabsorption Modulator

Typically in EML's, the bandgap of the modulator is slightly larger than that in the DFB laser section with a detuning of about 30–60 nm [8], [9], so that for zero or forward modulator voltage bias there is no attenuation except for insertion loss. For a positive voltage bias, carriers are injected so that light propagating through the modulator experiences gain, and the refractive index of the modulator decreases. If a negative voltage bias is applied to the modulator, absorption is increased due to the quantum-confined Stark effects or Franz-Keldysh effects which, in turn, increase the refractive index of the modulator. We model the voltage-dependent gain (negative absorption) and refractive index in the modulator through a simple linear additive term as given by

$$g_{\text{mod}} \simeq g_o + \frac{dg}{dV_{\text{mod}}} V_{\text{mod}} \quad (24)$$

$$n_{\text{mod}} \simeq n_o - \frac{dn}{dV_{\text{mod}}} V_{\text{mod}} \quad (25)$$

where  $g_{\text{mod}}$  and  $n_{\text{mod}}$  are the gain coefficient (1/cm) and effective index in the modulator, respectively,  $g_o$  and  $n_o$  are the gain and effective index in the modulator with no voltage bias,  $dg/dV_{\text{mod}}$  and  $dn/dV_{\text{mod}}$  are empirical constants, and  $V_{\text{mod}}$  is the voltage bias at the modulator. Note that both  $dg/dV_{\text{mod}}$  and  $dn/dV_{\text{mod}}$  are positive. Because the change in refractive index in the forward bias case is caused by carrier injection while the change in refractive index in the reverse bias case is caused by the electroabsorption effect, the value of  $dn/dV_{\text{mod}}$  is different for each case. In both cases, the change in refractive index in the modulator due to the voltage bias is the mechanism responsible for the phase-shifting effect, as will be explained in Section IV.

#### E. Leakage Current from the Modulator

The function of the fabricated isolation region is to provide electrical isolation between the modulator and laser sections so that the biasing of one section does not affect the performance of the other. However, the isolation region in this particular device does not provide perfect electrical isolation. When the modulator is forward-biased, carriers are injected into the modulator and a small leakage current flows from the modulator into the laser section. This leakage current will decrease the refractive index of the laser section and is included in the model using a simple empirical relation

$$n_{\text{DFB}} = n_o - \frac{dn_{\text{leak}}}{dV_{\text{mod}}} V_{\text{mod}} \quad (26)$$

where  $n_{\text{DFB}}$  is the modified effective index of the laser section,  $n_o$  is the original effective index and  $dn_{\text{leak}}/dV_{\text{mod}}$  is the change in effective index due to the leakage current

and is determined empirically by the observed shift in lasing wavelength in the measured spectrum as a function of  $V_{\text{mod}}$ .

### IV. RESULTS AND DISCUSSIONS

#### A. Wavelength-Tuning Mechanisms—Phase-Shifting and Current Tuning

Although our transfer matrix method provides the full numerical solution taking into account all multiple reflection, we present a simple physical model to illustrate the physics of the tuning mechanisms below. Since the isolation region and modulator are homogeneous, meaning that there is no distributed feedback present, the round trip through these sections can also be perceived as an effective reflectivity at the DFB-isolation region interface. Varying the modulator voltage will change the magnitude and phase of the reflectivity at this interface; hence, the modulator acts as a phase-shifting section. The voltage-dependent magnitude and phase of the interface reflectivity is approximately

$$r_{\text{int}} = r_{\text{HR}} e^{i2\beta_{\text{iso}} L_{\text{iso}}} e^{i2\beta_{\text{mod}} L_{\text{mod}}} \quad (27)$$

where  $r_{\text{int}}$  and  $r_{\text{HR}}$  are the magnitudes of the field reflectivity at the laser-isolation region and HR facet, respectively,  $L_{\text{iso}}$  and  $L_{\text{mod}}$  are the lengths of the isolation region and modulator, respectively,  $\beta_{\text{iso}}$  is the propagation constant of the isolation region, and  $\beta_{\text{mod}}$  is the voltage-dependent propagation constant of the modulator given by

$$\beta_{\text{mod}} = \frac{2\pi}{\lambda} n_{\text{mod}} - i \frac{g_{\text{mod}}}{2} \quad (28)$$

where  $g_{\text{mod}}$  and  $n_{\text{mod}}$  are functions of modulator voltage and are given by (24) and (25), respectively. Therefore, the change in phase at the interface due to a voltage-dependent change in refractive index is given by

$$\Delta\phi = \frac{4\pi\Delta n_e L_{\text{mod}}}{\lambda} \quad (29)$$

where  $\Delta n_e$  is given by the voltage-dependent term in (25).

It is well known that in an HR-/AR-coated DFB laser the lasing wavelength can change dramatically for different phases at the HR facet [22]. By integrating a phase-tuning section into the HR-coated side of the DFB laser, we use this idea to achieve voltage-controlled wavelength tuning over the stopband of the DFB laser.

The other mechanism behind wavelength tuning in this integrated device is due to leakage current from the modulator. An increasing positive modulator voltage will inject carriers into the laser section, decrease the refractive index of the laser, and shift the spectrum toward longer wavelengths. For larger negative voltage biases, carriers are absorbed from the laser and the spectrum shifts toward shorter wavelengths. Although leakage current is not usually viewed favorably, this effect, when combined with the phase-shifting effect, actually allows this device to achieve a larger wavelength-tuning range than phase shifting alone.

The wavelength-tuning behavior of this device naturally leads to a discussion on the advantages and disadvantages of current tuning and phase shifting as wavelength-tuning

mechanisms in lasers. The idea of using different injection currents and operating temperatures to produce a change in the wavelength of the lasing mode has long been known and has been extended to a variety of other types of devices, including multisection lasers. The advantage of current tuning is that one can achieve a continuous tuning range. The main disadvantage is that, for wavelength switching, as used in traffic routing applications, current tuning is a relatively slow process, limited by the carrier lifetime, and cannot support wavelength switching at rates in the multigigahertz range. In order to increase wavelength switching rates, several groups have taken advantage of the faster Franz-Keldysh effects in a reverse-biased electroabsorption modulator to produce wavelength switching. Nakajima *et al.* demonstrated wavelength switching at 10 Gb/s over a 0.2-nm range [10]. This wavelength tuning was achieved by absorption of carriers by the modulator and is essentially voltage tuning using a faster process.

Using the same type of device presented here, it has been shown that wavelength switching at 2.5 Gb/s between four wavelength channels spanning a 2.1-nm range can be achieved [11]. The wider wavelength range achieved here is due to the fact that both phase shifting and voltage tuning from quantum-confined Stark effects were used to produce the wavelength tuning.

### B. Spectrum of the Integrated DFB Laser-Modulator

Our model was first used to explain some of the features present in the output spectrum of this curved waveguide DFB laser with an integrated modulator. The spectrum of a conventional HR/AR-coated DFB laser was measured above threshold as shown in Fig. 2(a). The DFB laser spectrum typically has a lasing mode with a sidemode suppression ratio (SMSR) greater than 30 dB on one side of the stopband and side modes with amplitudes which decrease gradually for shorter and longer wavelengths away from the stopband. The measured spectrum of the integrated device with no modulator voltage bias is shown in Fig. 2(b) and shows several interesting features which differ from the conventional DFB laser. The first feature is the absence of a visible stopband. The second feature is that the modes alternate in amplitude, whereas the mode amplitudes of the conventional DFB laser gradually decrease away from the stopband. The third feature is that competing side modes can be seen on both sides of the lasing mode, whereas in the conventional DFB laser, there is usually only one competing mode located on the other side of the stopband. The theoretically calculated spectrum shown in Fig. 2(c) exhibits features which are quite similar to the measured spectrum shown in Fig. 2(b). The parameters used in simulations of the integrated wavelength-tunable device are shown in Table I.

The spectrum of the integrated device can be explained by looking at the threshold gain of the modes as a function of wavelength for several cases. First we consider the effect of using a two-section DFB laser-modulator device compared to the single-section DFB laser case. Shown in Fig. 3(a) are the modes for a single-section DFB laser with a straight waveguide case. Shown in Fig. 3(b) are the modes for the two-section integrated laser-modulator. For the single-section DFB laser,

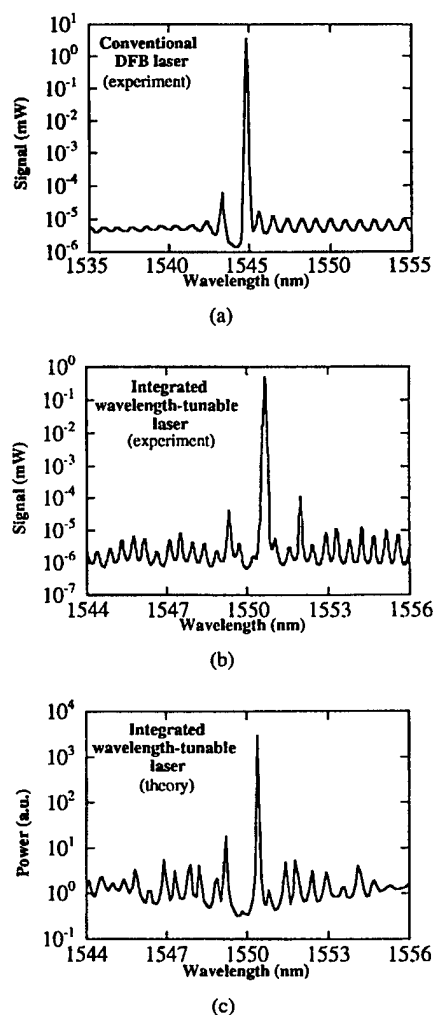


Fig. 2. (a) Measured spectrum of a conventional HR/AR-coated DFB laser. The spectrum typically has a lasing mode with good SMSR on one side of the stopband and side modes with amplitudes which decrease gradually for shorter and longer wavelengths away from the stopband. (b) Measured spectrum for the integrated wavelength-tunable laser. This spectrum differs from the conventional DFB laser in that the stopband is less visible, the modes alternate amplitudes away from the stopband, and competing side modes are present on either side of the lasing mode. (c) Theoretically calculated spectrum of the integrated wavelength-tunable laser. This spectrum shows similar features to the experimentally measured spectrum in (b).

the modes show a well-defined stopband. However, for the two-section DFB laser-modulator device, the modes seem to separate into two sets near the stopband, where the set of modes with higher threshold gain corresponds to the coupled-cavity effects from the modulator region, and the modes with lower threshold gain correspond to the DFB laser region. This accounts for the alternating mode amplitude behavior away from the stopband toward shorter and longer wavelengths as seen in the spectrum.

In a straight waveguide, the grating pitch is constant as a function of longitudinal cavity position which produces two well-defined Bragg frequency modes located opposite each other across the stopband. In the curved waveguide, the grating pitch is chirped as a function of cavity position, which produces a mode-flattening effect around the stopband which increases as a function of S-bend width  $W$ . This effect is illustrated by simulating a single-section AR/AR-coated DFB

TABLE I  
PARAMETER LIST USED FOR SIMULATIONS

Power reflectivity at HR facet $R_{HR}$	0.99
Power reflectivity at AR facet $R_{AR}$	0.01
Phase at HR facet $\phi_{HR}$	$30^\circ$
Phase at AR facet $\phi_{AR}$	$0^\circ$
Coupling coefficient-length product $\kappa L_{DFB}$	3.0
Length of laser section $L_{DFB}(\mu\text{m})$	360
Length of isolator section $L_{ISO}(\mu\text{m})$	80
Length of modulator section $L_{MOD}(\mu\text{m})$	260
Grating pitch $\Lambda_o(\mu\text{m})$	0.2308
S-bend parameter $L_1(\mu\text{m})$	47
S-bend parameter $L_B(\mu\text{m})$	133
S-bend parameter $W(\mu\text{m})$	10
Group index $n_g$	3.6
Linewidth enhancement factor $\alpha_e$	4
Optical confinement factor $\Gamma$	0.03
Transparent carrier density $N_o(\text{cm}^{-3})$	$1.5 \times 10^{-18}$
Differential gain $g'(\text{cm}^2)$	$2.7 \times 10^{-18}$
$dn_{\text{leak}}/V_{\text{mod}}(V^{-1})$	0.002169
$dg/V_{\text{mod}}(\text{cm}^{-1} V^{-1})$	8.0
$dn/V_{\text{mod}}$ for $V_{\text{mod}} > 0(V^{-1})$	0.013135
$dn/V_{\text{mod}}$ for $V_{\text{mod}} < 0(V^{-1})$	0.01129
Group velocity $v_g(\text{m/s})$	$8.33 \times 10^8$
Dispersion parameter $s(1/\mu\text{m})$	0.21930

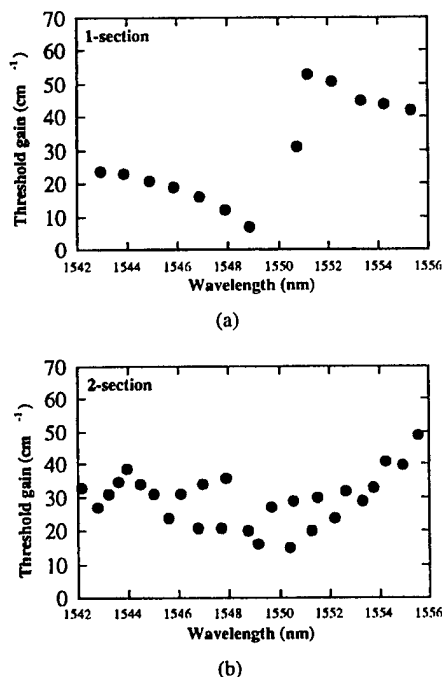


Fig. 3. (a) Modes for a one-section DFB laser, where the modes show a well-defined stopband. (b) Modes for the two-section integrated laser-modulator: the modes show a splitting near the stopband, the upper modes corresponding to the modulator region and the lower modes corresponding to the DFB laser region.

laser in order to isolate the effects of using the curved waveguide and to more clearly illustrate the effect. In Fig. 4(a)–(c), the threshold gain of the theoretically calculated modes are plotted versus wavelength for increasing values of  $W$ . The mode-flattening effect comes from the fact that, using a curved waveguide or chirped grating pitch, the Bragg wavelength is no longer defined as a single frequency but a range of frequencies. Therefore, the distributed feedback is weaker for one particular

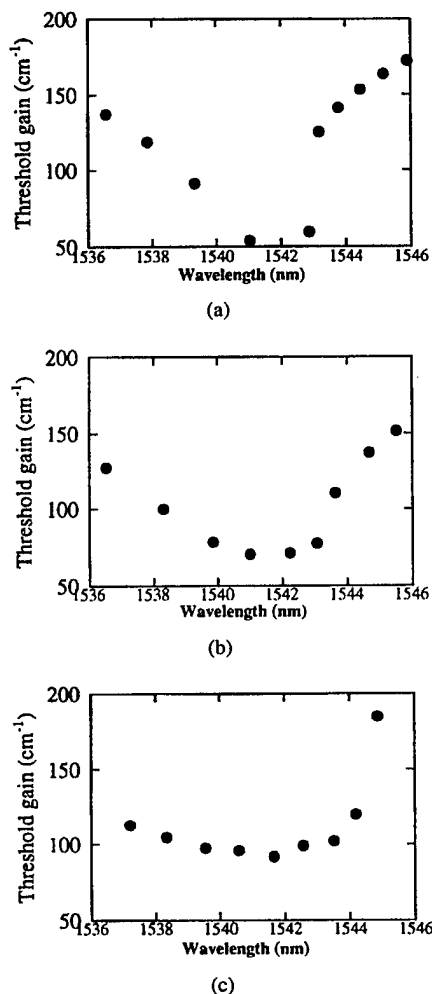


Fig. 4. The theoretically calculated threshold gain of the modes for an AR/AR-coated DFB laser as a function of wavelength for (a)  $W = 0 \mu\text{m}$ , (b)  $W = 5 \mu\text{m}$ , and (c)  $W = 15 \mu\text{m}$ . In general, increasing the width of curved waveguide  $W$  produces a mode-flattening effect around the stopband, which can enhance mode tunability.

frequency, and the SMSR as determined by the threshold gain decreases as a result. This mode-flattening effect around the stopband accounts for the presence of multiple competing side modes in the spectrum of the integrated device as well as the absence of a stopband. Although a reduced SMSR is not desirable, this mode-flattening effect may extend the wavelength-tuning range of this type of device by providing more competing modes for lasing, which may be selected by the modulator section. Far outside the stopband, the mode behavior was observed to be determined by the Fabry-Perot cavity in both experiment and theory as expected. Simulations of the modes for an HR/AR-coated DFB laser show a similar mode-flattening effect due to the curved waveguide.

### C. Wavelength Tuning of the Lasing Mode

The model was used to simulate the wavelength-tuning behavior in the integrated DFB laser-modulator for several values of modulator voltage. Fig. 5(a) shows the measured spectrum of the integrated device for modulator voltage values of 0, +0.47, +0.78, +0.87, +0.92, and +1.03 V. As explained earlier, the wavelength tuning occurs due to a



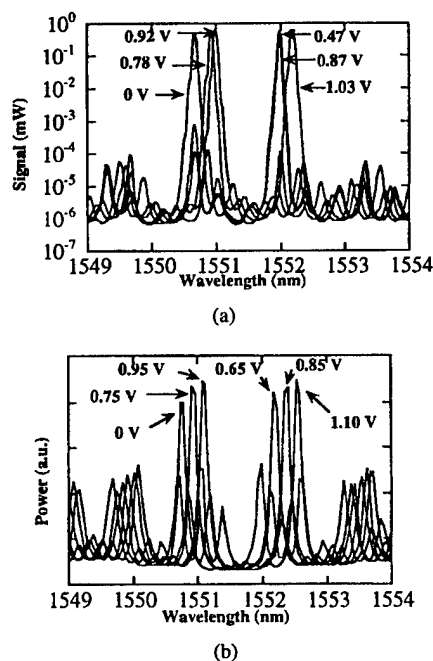


Fig. 5. (a) Measured spectrum of the integrated device at modulator voltage values of 0, +0.47, +0.78, +0.87, +0.92, and +1.03. (b) Theoretically calculated spectrum of the integrated devices at modulator voltage values of 0, +0.65, +0.75, +0.85, +0.95, and +1.10.

combination of phase shifting and current tuning. In general, the wavelength-tuning behavior of this device can be described in the following way. As the modulator voltage is increased from 0 V, the lasing mode remains at one wavelength until +0.47 V, where the lasing mode switches abruptly to a second wavelength. As the modulator voltage is increased further, the lasing mode remains at this second wavelength until +0.78 V, where the lasing mode switches to another wavelength, and this behavior continues until +1.03 V. Fig. 5(b) shows the theoretically calculated spectrum for modulator voltages of 0, +0.65, +0.75, +0.85, +0.95, and +1.10 V, which shows reasonably good agreement using the linear model for voltage-dependent refractive index.

For a positive voltage bias, the modulator gain and refractive index could be modeled more accurately by making them functions of carrier density in the modulator, which is a function of injected current in the modulator. Also, wavelength tuning of the lasing mode for positive bias voltages is also associated with changes in threshold current, linewidth, and output power. This was not included here, but we refer to [24] for a more detailed treatment.

Wavelength tuning of the lasing mode was also observed for negative modulator bias voltages, although for a more limited range for this particular device. While in the positive voltage bias case the refractive index decreases due to the injection of carriers, for this case, the refractive index increases due to absorption of carriers from quantum-confined Stark effects. Fig. 6(a) shows the measured spectra for modulator voltage values of 0, -0.45, and -0.78 V. Fig. 6(b) shows the theoretically calculated spectra for modulator voltage values of 0, -0.50, and -0.90 V, which show good agreement with the measured spectra. The lasing wavelength as a function of positive and negative modulator voltages is shown for both the

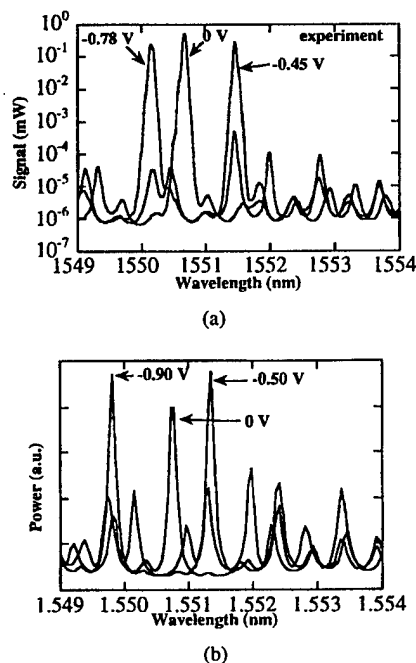


Fig. 6. (a) Measured spectra of the integrated device at modulator voltage values of 0, -0.45, and -0.78. (b) Theoretically calculated spectra of the integrated devices at modulator voltage values of 0, -0.50, and -0.90.

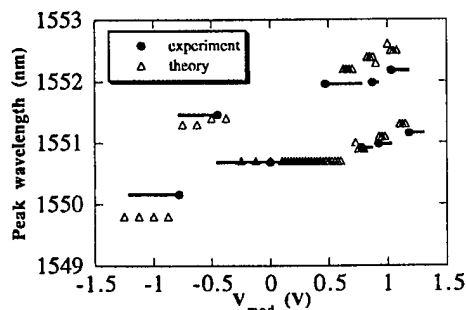


Fig. 7. Measured and theoretically calculated values of the lasing wavelength as a function of modulator voltage. The closed circles represent measured lasing wavelengths. The lines represent observed lasing wavelengths and are accurate to within  $\pm 1$  Å. The open triangles represent the theoretically calculated values.

experimentally measured and theoretically calculated spectra in Fig. 7. The closed circles are measured data points. The lasing wavelengths between data points, shown by the lines, were observed but not measured and are accurate to within  $\pm 1$  Å. The open triangles are the theoretically calculated values and show reasonably good agreement with the measured spectrum values.

#### D. Reduced SHB Due to the Curved Waveguide

SHB is an important phenomena which has been studied extensively [25]–[32], particularly in DFB lasers, because it can severely limit the maximum output power and cause mode hopping or multimode behavior. SHB is caused by a nonuniform distribution of the photon density along the longitudinal cavity which can be caused by the distributed feedback in DFB lasers as well as asymmetries in HR/AR-coated DFB lasers. A greater photon density in one region of a DFB laser will cause greater carrier depletion in that

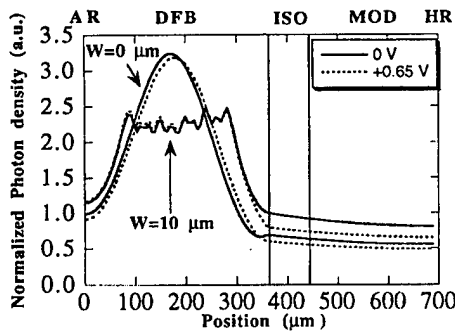


Fig. 8. The theoretically calculated photon density as a function of longitudinal cavity position for the straight waveguide ( $W = 0 \mu\text{m}$ ) and curved waveguide ( $W = 10 \mu\text{m}$ ) cases. The solid lines are for  $V_{\text{mod}} = 0$ , and the dashed lines are for a different lasing mode at  $V_{\text{mod}} = +0.65$ . The curved waveguide shows less perturbation in the photon density profile and therefore less SHB effects compared to the straight waveguide case.

region so the carrier density profile also becomes nonuniform along the cavity. This in turn produces a nonuniform refractive index profile which affects the threshold gain conditions of the modes and can result in mode hopping or multimode lasing at moderate injection currents above threshold. The model was used to calculate the longitudinal photon density profile for the straight and curved waveguide cases, as shown in Fig. 8. The corresponding facet coatings and device sections are labeled with cavity position. The solid lines are for  $V_{\text{mod}} = 0$  V, and the dashed lines are for  $V_{\text{mod}} = +0.65$  V. Considering only the laser section, the photon density profile shows a larger perturbation in the straight waveguide case than that for the curved waveguide case. One way to evaluate the amount of SHB present in a DFB laser is to calculate a flatness parameter [33]. We use a modified flatness parameter given by

$$F = \frac{1}{L} \int (I(z)_{\text{norm}} - I_{\text{avg}})^2 dz \quad (30)$$

where  $L$  is the length of the DFB laser section,  $I(z)_{\text{norm}}$  is the normalized local field intensity, and  $I_{\text{avg}}$  is the average normalized intensity. The integration is performed only over the DFB laser cavity length. Note that a greater  $F$  value indicates larger SHB effects. For the  $V_{\text{mod}} = 0$  V case, the calculated value of  $F$  was 0.78 for the straight waveguide and 0.21 for the curved waveguide. Very similar results were obtained for the other values of  $V_{\text{mod}}$ . These results suggest that the curved waveguide exhibits less SHB than in the straight waveguide case. This is significant because a device with less SHB can remain at stable operation at higher output powers.

The photon density profile of the curved waveguide, as shown in Fig. 8, exhibits an oscillatory behavior [34], [35]. This can be explained by the fact that this curved waveguide produces multiple distributed phase shifts due to the chirped pitch grating. Other groups have modeled multiple phase-shift devices which show multiple peaks in the photon density profile [36] and also distributed phase-shift devices which exhibit a rounding and flattening of a photon density peak when compared to an abrupt phase shift [16].

Several designs can be implemented to improve the performance of this device.

- 1) The present device mode shifts between only two modes. By optimizing the curved waveguide shape and increasing the mode-flattening effect, we should be able to obtain mode shifting between three or more modes, thereby increasing the wavelength-tuning range. However, the tradeoff would be a decrease in SMSR.
- 2) The concept of an amplitude-modulated grating [37] can be used to extend the phase-shifting range. Although originally designed to flatten the photon profile and reduce SHB effects, this idea may also be used to enhance the phase-shifting range.

## V. CONCLUSIONS

We have theoretically modeled a DFB laser with a curved waveguide integrated with an electroabsorption modulator which acts as a wavelength-tuning section. The characteristics of the output spectrum have been identified, and the mechanisms behind the wavelength tuning, namely, phase shifting and voltage tuning, have been explained using simulation results which show good agreement with experiment. The model also shows that the curved waveguide suppresses the photon density profile and reduces SHB compared to the straight waveguide case. The development of wavelength-tunable lasers with greater tuning range and higher power operation should be achievable using a curved waveguide.

## ACKNOWLEDGMENT

The authors would like to acknowledge R. People, C. Bethea, A. M. Sergent, and W. T. Tsang for their technical expertise and discussions.

## REFERENCES

- [1] K. Kobayashi and I. Mito, "Single frequency and tunable laser diodes," *J. Lightwave Technol.*, vol. 6, pp. 1623–1633, 1988.
- [2] H. Kawaguchi, "Progress in optical functional devices using two-section laser diodes/amplifiers," *Proc. Inst. Elect. Eng.*, pt. J, vol. 140, pp. 3–15, 1993.
- [3] Y. Kawamura, K. Wakita, Y. Yoshikuni, Y. Itaya, and H. Asahi, "Monolithic integration of a DFB laser and an MQW optical modulator in the  $1.5 \mu\text{m}$  range," *IEEE J. Quantum Electron.*, vol. QE-23, pp. 915–918, 1987.
- [4] M. Suzuki, Y. Noda, H. Tanaka, S. Akiba, Y. Kushiro, and H. Issikhi, "Monolithic integration of an InGaAsP/InP distributed feedback laser and electroabsorption modulator and vapor phase epitaxy," *IEEE J. Quantum Electron.*, vol. QE-23, pp. 915–918, 1987.
- [5] M. Aoki, M. Suzuki, H. Sano, T. Kawano, T. Ido, T. Taniwatari, K. Uomi, and A. Takai, "InGaAs/InGaAsP MQW electroabsorption modulator integrated with a DFB laser fabricated by band-gap energy control selective area MOCVD," *IEEE J. Quantum Electron.*, vol. 29, pp. 2088–2096, 1993.
- [6] T. Kato, T. Sasaki, K. Komatsu, and I. Mito, "DFB-LD/modulator integrated light source by bandgap energy controlled selective MOVPE," *Electron. Lett.*, vol. 28, pp. 153–154, 1992.
- [7] T. Tanbun-Ek, Y. K. Chen, J. A. Grenko, E. K. Byrne, J. E. Johnson, R. A. Logan, A. Tate, A. M. Sergent, K. W. Wecht, P. F. Sciorfino, Jr., and S. N. G. Chu, "Integrated DFB-DBR laser modulator grown by selective area metalorganic vapor phase epitaxy growth technique," *J. Cryst. Growth*, vol. 145, pp. 902–906, 1994.
- [8] A. Ramdane, F. Devaux, N. Souli, D. Delprat, and A. Ougazzaden, "Monolithic integration of multiple-quantum-well lasers and modulators for high-speed transmission," *IEEE J. Select. Topics Quantum Electron.*, vol. 2, pp. 326–335, 1996.
- [9] H. Takeuchi, K. Tsuzuki, K. Sato, M. Yamamoto, Y. Itaya, A. Sano, M. Yoneyama, and T. Otsuji, "Very high-speed light-source module up to 40 Gb/s containing an MQW electroabsorption modulator integrated with a DFB laser," *IEEE J. Select. Topics Quantum Electron.*, vol. 3, pp. 336–343, 1997.

- [10] H. Nakajima, J. Charil, S. Slempek, A. Gloukhian, B. Pierre, J. Landreau, and Y. Raffle, "Very high-speed wavelength switching capability Franz-Keldysh electroabsorption DFB lasers," in *Optical Fiber Conf. Tech. Dig.*, 1996, p. 276.
- [11] T. Tanbun-Ek, L. Adams, G. Nykolak, C. Bethea, R. People, A. Sergeant, P. Wisk, P. Sciortino, Jr., S. Chu, T. Fullowan, and W. T. Tsang, "Broad-band tunable electroabsorption modulated laser for WDM application," *IEEE J. Select. Topics Quantum Electron.*, vol. 3, pp. 960-966, 1997.
- [12] A. Katzir, A. C. Livanos, and A. Yariv, "Chirped-grating output couplers in dielectric waveguides," *Appl. Phys. Lett.*, vol. 30, pp. 225-226, 1977.
- [13] P. Zhou and G. S. Lee, "Chirped grating  $\lambda/4$  shifted DFB laser with uniform longitudinal field distribution," *Electron. Lett.*, vol. 26, pp. 1660-1661, 1990.
- [14] M. Okai, T. Tsuchiya, K. Uomi, N. Chinone, and T. Harada, "Corrugation-pitch modulated MQW-DFB lasers with narrow spectral linewidth," *IEEE J. Quantum Electron.*, vol. 27, pp. 1767-1772, 1991.
- [15] W. T. Tsang, R. M. Kapre, R. A. Logan, and T. Tanbun-Ek, "Control of lasing wavelength in distributed feedback lasers by angling the active stripe with respect to the grating," *IEEE Photon. Technol. Lett.*, vol. 5, pp. 10-12, 1993.
- [16] H. Hillmer, A. Grabmaier, S. Hansmann, H.-L. Zhu, H. Burkhard, and K. Magari, "Tailored DFB lasers properties by individually chirped gratings using bent waveguide," *IEEE J. Select. Topics Quantum Electron.*, vol. 1, pp. 356-362, 1995.
- [17] J. Salzman, H. Olesen, A. Moller-Larson, O. Albrektsen, J. Hanberg, J. Norregaard, B. Jonsson, and B. Tromborg, "Distributed feedback lasers with an S-bent waveguide for high-power single-mode operation," *IEEE J. Select. Topics Quantum Electron.*, vol. 1, pp. 346-355, 1995.
- [18] W. Fang, S. L. Chuang, T. Tanbun-Ek, and Y. K. Chen, "Modeling and experiment of 1.55  $\mu\text{m}$  integrated electroabsorption modulator with distributed-feedback laser," in *Proc. SPIE: Optoelectronic Integrated Circuits*, Y. S. Park and R. V. Ramaswamy, Eds., 1997, vol. 3006, pp. 207-215.
- [19] W. Fang, A. Hsu, S. L. Chuang, T. Tanbun-Ek, and A. M. Sergeant, "Measurement and modeling of distributed-feedback lasers with spatial hole burning," *IEEE J. Select. Topics Quantum Electron.*, vol. 3, pp. 547-554, 1997.
- [20] C. H. Chen and G. Griffel, "Static, dynamic, and noise analysis of multisection DFB lasers using frequency-domain transmission line model," *IEEE J. Quantum Electron.*, vol. 34, pp. 1533-1544, 1998.
- [21] C. S. Chang, S. L. Chuang, J. R. Minch, W. Fang, Y. K. Chen, and T. Tanbun-Ek, "Amplified spontaneous emission spectroscopy in strained quantum-well lasers," *IEEE J. Select. Topics Quantum Electron.*, vol. 1, pp. 1100-1107, 1995.
- [22] S. Chinn, "Effects of mirror reflectivity in a distributed-feedback laser," *IEEE J. Quantum Electron.*, vol. 9, pp. 574-580, 1973.
- [23] M. Kitamura, M. Yamaguchi, K. Emura, I. Mito, and K. Kobayashi, "Lasing mode and spectral linewidth control by phase tunable distributed feedback laser diodes with double channel planar buried heterostructure (DFB-DC-PBH LD's)," *IEEE J. Quantum Electron.*, vol. QE-21, pp. 415-417, 1985.
- [24] H. Olesen, X. Pan, and B. Tromborg, "Theoretical analysis of tuning properties for a phase-tunable DFB laser," *IEEE J. Quantum Electron.*, vol. QE-23, pp. 2367-2375, 1987.
- [25] M. Aoki, K. Uomi, T. Tsuchiya, S. Sasaki, M. Okai, and N. Chinone, "Quantum size effect on longitudinal spatial hole burning in MQW  $\lambda/4$ -shifted DFB lasers," *IEEE J. Quantum Electron.*, vol. 27, pp. 1782-1789, 1991.
- [26] F. Girardin, G. H. Duan, and A. Talneau, "Modeling and measurement of spatial-hole-burning applied to amplitude modulated coupling distributed feedback lasers," *IEEE J. Quantum Electron.*, vol. 31, pp. 834-841, 1995.
- [27] M. R. Phillips, T. E. Darcie, and E. J. Flynn, "Experimental measure of dynamic spatial-hole burning in DFB lasers," *IEEE Photon. Technol. Lett.*, vol. 4, pp. 1201-1203, 1992.
- [28] S. Hansmann, H. Walter, H. Hillmer, and H. Burkhard, "Static and dynamic properties of InGaAsP-InP distributed feedback lasers—A detailed comparison between experiment and theory," *IEEE J. Quantum Electron.*, vol. 30, pp. 2477-2484, 1994.
- [29] I. Orfanos, T. Sphicopoulos, A. Tsigopoulos, and C. Caroubalos, "A tractable above-threshold model for the design of DFB and phase-shifted DFB lasers," *IEEE J. Quantum Electron.*, vol. 27, pp. 946-956, 1991.
- [30] M. G. Davis and R. F. O'Dowd, "A transfer matrix method based large-signal dynamic model for multielectrode DFB lasers," *IEEE J. Quantum Electron.*, vol. 30, pp. 2458-2466, 1994.
- [31] P. Correc, "Stability of phase-shifted DFB lasers against hole burning," *IEEE J. Quantum Electron.*, vol. 30, pp. 2467-2476, 1994.
- [32] S. F. Yu, "A quasithree-dimensional large-signal dynamic model of distributed feedback lasers," *IEEE J. Quantum Electron.*, vol. 32, pp. 424-432, 1996.
- [33] H. Soda, Y. Kotaki, H. Sudo, H. Ishikawa, S. Yamakoshi, and H. Imai, "Stability in single longitudinal mode operation in GaInAsP/InP phase adjusted DFB lasers," *IEEE J. Quantum Electron.*, vol. QE-23, pp. 804-814, 1987.
- [34] A. Hsu, W. Fang, S. L. Chuang, T. Tanbun-Ek, C. Bethea, and R. People, "Integrated tunable laser with mode selection modulator," in *Photonics West*, San Jose, CA, Jan. 24-30, 1998.
- [35] A. Hsu, W. Fang, and S. L. Chuang, "Modeling of normal and backward integrated electroabsorption modulator and laser," in *Integrated Photonics Research*, Victoria, BC, Canada, Mar. 29-Apr. 3, 1998.
- [36] H. Ghafouri-Shiraz and B. S. K. Lo, *Distributed Feedback Laser Diodes*. New York: Wiley, 1996.
- [37] G. Morthier, K. David, P. Vankwikelberge, and R. Baets, "A new DFB-laser diode with reduced spatial hole burning," *IEEE Photon. Technol. Lett.*, vol. 2, pp. 388-390, 1990.

**Alan Hsu** was born in Chicago Heights, IL, in 1974. He received the B.S. and M.S. degrees in electrical engineering from the University of Illinois at Urbana-Champaign in 1996 and 1998, respectively, where he is currently working toward the Ph.D. degree.

His research interests include integrated semiconductor laser devices for high-speed wavelength-division-multiplexed fiber-optic communication systems as well as all-optical wavelength conversion. He is also working on fiber-optic sensor development for rail break and buckling detection applications. He has conducted research as an intern at NTT Basic Research Laboratories, Atsugi, Japan, in 1998, Bell Laboratories, Murray Hill, NJ, in 1997, and Qualcomm, San Diego, CA, in 1995 and 1996.

**Shun-Lien Chuang** (S'78-M'82-SM'88-F'97) received the B.S. degree in electrical engineering from National Taiwan University in 1976 and the M.S., E.E., and Ph.D. degrees in electrical engineering from the Massachusetts Institute of Technology, Cambridge, in 1980, 1981, and 1983, respectively.

In 1983, he joined the Department of Electrical and Computer Engineering at the University of Illinois at Urbana-Champaign (UIUC), Urbana, where he is currently a Professor. He was a Resident Visitor at AT&T Bell Laboratories, Holmdel, NJ, in 1989 and a consultant at Bellcore and Polaroid in 1991. He was a Senior Visiting Professor (Sabbatical Chair) at SONY Research Center in 1995 and an Invited Professor at NTT Basic Research Laboratories, Japan, in 1997. He is conducting research on strained quantum-well semiconductor lasers, electroabsorption modulators, fiber optics, and femtosecond nonlinear optics. He was a Feature Editor for a special issue in *Journal of the Optical Society of America B* on "Terahertz Generation, Physics, and Applications" in 1994, and he is the author of *Physics of Optoelectronic Devices* (New York: Wiley, 1995).

Dr. Chuang is a fellow of the Optical Society of America and a member of the American Physical Society. He has been cited several times for Excellence in Teaching at UIUC. He received the Andersen Consulting Award for excellence in advising in 1994 and was selected as an Associate at the Center for Advanced Study at UIUC in 1995. He was also awarded a Fellowship from the Japan Society for the Promotion of Science to visit the University of Tokyo in 1996. He is an Associate Editor of the *IEEE JOURNAL OF QUANTUM ELECTRONICS*.

**W. Fang**, photograph and biography not available at the time of publication.

**L. E. Adams**, photograph and biography not available at the time of publication.

**G. Nykolak**, photograph and biography not available at the time of publication.

**T. Tanbun-Ek**, photograph and biography not available at the time of publication.

# Optical gain measurements based on fundamental properties and comparison with many-body theory

T. Keating, S. H. Park,<sup>a)</sup> J. Minch,<sup>b)</sup> X. Jin, and S. L. Chuang<sup>c)</sup>

*Department of Electrical and Computer Engineering, University of Illinois at Urbana-Champaign, 1406 West Green Street, Urbana, Illinois 61801*

T. Tanbun-Ek<sup>d)</sup>

*Bell Laboratories, Lucent Technologies, 700 Mountain Avenue, Murray Hill, New Jersey 07974*

(Received 28 September 1998; accepted for publication 8 June 1999)

We present high accuracy measurements of gain, loss, and transparency energy in long-wavelength semiconductors based on a hybrid approach using the fundamental relationship between the gain and the spontaneous emission spectra. Independent measurements of optical gain, transparency energy, and loss show the accuracy and validity of this technique. These results are compared with those obtained by the non-Markovian gain model with many-body effects under the spontaneous emission transformation method. It is found that the hybrid approach for the gain spectrum alleviates many of the problems related to the poor signal to noise ratio in the amplified-spontaneous emission near and below the band edge. The theoretical spectra compare well with the measured spectra for both the transverse electric and transverse magnetic polarizations. © 1999 American Institute of Physics. [S0021-8979(99)01018-X]

## I. INTRODUCTION

Optical gain and loss are of fundamental importance to the study of lasers, since the gain determines many device performance characteristics. Therefore, accurate and reliable gain measurement techniques are essential tools for the experimental study of lasers. Likewise, highly accurate theoretical gain models incorporating the most realistic physical effects are also essential to advance the state of the art. Such models are most stringently tested against the best obtainable data, since the usefulness of theoretical predictions of gain and carrier density depends both on the model and on close agreement with accurately measured data.

On the experimental side, several excellent and widely used techniques already exist for measurements of gain and loss, yet there are instances where improvements are still needed. Measuring the gain in a Fabry-Perot or distributed-feedback laser typically first involves measuring the amplified spontaneous emission (ASE) of the laser. Since the ASE signals are very weak below the band edge, however, the evaluation of gain may degrade strongly due to poor signal to noise ratios in the ASE. As a consequence, commonly used techniques for measuring the modal gain, such as the Hakki-Paoli method<sup>1</sup> or Cassidy's<sup>2</sup> method, show a significant amount of noise in the region of the gain tail because of reduced signal intensity. While some reduction in the noise susceptibility of both methods can be achieved through an

averaging procedure,<sup>3</sup> the results thus obtained are less accurate.

Difficulties in measuring the gain tail can compound to create further problems, since estimates of the intrinsic loss are often obtained by examining the limit of the gain tail. For instance, assuming the intrinsic losses are constant with respect to wavelength, the measured loss may be used to find the transparency energy. But it is impossible to do so if the losses are inaccurate. In turn each of these problems impacts the comparison between theory and experiment. Accurate values of the loss are needed to properly renormalize theoretical spectra. Moreover, an incorrect renormalization will, in effect, shift the location of the transparency energy. Thus, clear data in the tail region is necessary for comparison to theoretical gain models in terms of predicted line broadening behavior.

On the theoretical side, conventional optical gain calculations are usually based on the density-matrix theory with a phenomenological damping term which gives the Lorentzian line shape function.<sup>4</sup> A few groups<sup>5-8</sup> have argued that the optical gain spectra calculated with the Lorentzian line shape function deviate from the experimental results. Especially, an anomalous absorption region below the band gap and discrepancies between the transparency points and the Fermi-level separation appear in the gain spectra when the Lorentzian line shape is used. To overcome these artifacts, the intraband relaxation times by the carrier-carrier and carrier-longitudinal optical (LO) phonon scatterings have been considered to obtain the line shape function.<sup>7,8</sup> Its low-energy tail decreases much faster than the Lorentzian line shape while its high-energy tail is close to the Lorentzian line shape. This shows that the steepness of the low-energy tail of the line shape function is most important. However, these models require a large amount of computational time. As a

<sup>a)</sup>On leave from the Department of Physics, Catholic University of Taegu-Hyosang, Hayang, Kyeonbuk, Korea.

<sup>b)</sup>Currently with Lincoln laboratory, 244 Wood Street, Lexington, MA 02420.

<sup>c)</sup>Author to whom correspondence should be addressed; electronic mail: s-chuang@uiuc.edu

<sup>d)</sup>Also with Multiplex, Inc. 115 Corporate Blvd., South Plainfield, NJ 07080.

simplified approach, approximate formula considering only the hole-hole scattering has often been used in calculating the optical gain spectrum.<sup>9-11</sup> Another approach is to replace the Lorentzian line shape function with a sharper spectral function, i.e., with a Gaussian line shape. The effect of Gaussian line shape is similar to that of the line shape function considering the carrier-carrier and carrier-LO phonon scattering.

On the other hand, the spontaneous emission transformation method using the fundamental relations between the spontaneous emission and the absorption coefficients has been proposed as an improved method.<sup>5,12-15</sup> It guarantees that artifacts mentioned above are circumvented independent of the line shape functions (Lorentzian, Gaussian, or others). Also, the slow convergence of the Lorentzian leads to a very long tail of the gain spectra into the band gap, in contradiction to experimental observations.<sup>15</sup> Hence, a non-Markovian (Gaussian) gain model under the spontaneous emission transformation method is desirable to obtain the optical gain spectrum.<sup>16,17</sup>

In this article, we present high accuracy measurements of the optical gain, using the fundamental relationship between the spontaneous emission spectrum and the gain spectrum. The values for transparency energy and loss obtained from this technique compare favorably with those obtained from several independent measurements.<sup>18</sup> Experimentally, the major techniques involve measuring (1) gain and spontaneous emission, (2) polarization resolved gain spectra, (3) optical-pump induced modified gain spectra, and (4) pump-induced electrical responses<sup>19</sup> for directly obtaining the transparency energy and losses. The key information each technique provides is summarized as follows. First, since spontaneous emission and gain are related by only three parameters, the transparency energy, the loss, and a coupling constant, matching gain and spontaneous emission provides a way to estimate these parameters. Second, the quasi-Fermi level separation is the same at a fixed injection current for each polarization, so the polarization-resolved gain spectra will cross at the same quasi-Fermi level separation. Third, the net absorption of an optical pump will be zero at the quasi-Fermi level separation, so the change in gain will be zero for a pump wavelength located at that energy. Finally, the change in induced device voltage due to absorption of an external optical pump light will be zero when the pump wavelength is at the transparency energy.

The transformed spontaneous emission procedure yields highly accurate measurements of the gain tail, which are difficult to obtain from the other techniques. The experimentally obtained spectra are presented along with theoretical fits based on a many-body gain model. Theoretical gain models provide estimates of the carrier density within the active region by matching the predicted gain spectrum to the measured gain. For the best accuracy it is necessary to include all of the most important physical effects which determine the gain. A non-Markovian optical gain model with many-body effects is used to calculate the spectra. The plasma screening, band-gap renormalization (BGR), and the excitonic or the Coulomb enhancement (CE) of the interband transition probability are included in the model. Good agreement between

theory and experiment for both the transverse electric (TE) and transverse magnetic (TM) polarizations is obtained. Our model also provides the numerical values for the carrier densities.

Experimental results for the measurement of gain, loss, and transparency energy using the spontaneous emission spectrum and its fundamental relationship with the gain is presented in Sec. II along with a comparison to other methods for obtaining these quantities. A description of the many-body gain model and comparisons between theoretical and experimental results are discussed in Secs. III and IV. Finally, the summary and conclusions are presented in Sec. V.

## II. EXPERIMENTAL TECHNIQUES

The following experiments were performed using a nominally lattice-matched AlGaInAs multiple quantum-well laser. An unstrained quantum-well laser is chosen so that there will be a significant amount of gain for both the TE and TM polarizations. The laser is a Fabry-Perot device with a cavity length of 638  $\mu\text{m}$  and one facet coated for high (85%) reflectivity. Round trip mirror loss is 11.4  $\text{cm}^{-1}$ . The device was temperature controlled and all data were taken at 25  $^{\circ}\text{C}$ . For all spectra the device current was measured to within 10  $\mu\text{A}$  accuracy. Threshold at this temperature was 11.7 mA. Further structural details are described in Sec. IV.

### A. Method I: Measurement of spontaneous emission and the use of the fundamental relation

As described above, direct measurements of the gain provided insufficient data in the low energy tail region. On the other hand, very accurately measured values of transparency energy and loss can be yielded by using an indirect technique based on the relationship between spontaneous emission and gain. The optical gain spectra are related to the spontaneous emission spectra from the detailed balance between absorption and emission of photons.<sup>5,12-15</sup> That is, the modal gain from spontaneous emission is given by

$$g(E) = \frac{h^3 c^2}{8 \pi n_r^2 E^2} \left( 1 - \exp \frac{E - \Delta F}{k_B T} \right) r_{sp}(E) \quad (1)$$

in which  $r_{sp}$  is the spontaneous emission rate,  $\hbar = h/2\pi$ ,  $h$  is the Planck's constant,  $T$  is the temperature,  $E = \hbar \omega$ ,  $\Gamma$  is the optical confinement factor, and  $\Delta F$  is the transparency energy, which is given by the energy separation of the quasi-Fermi levels of the electrons and holes. In practice, the spontaneous emission power  $P_{sp}(\lambda)$  is measured within small resolution intervals  $d\lambda$  determined by the spectrometer over the entire spectrum,

$$P_{sb}(\lambda) = K_1 \frac{hc}{\lambda} r_{sp}(\lambda) d\lambda V \quad (2)$$

so the relation in Eq. (1) must be modified. First, the energy is expressed in terms of the wavelength, then the spontaneous emission rate is substituted by the power through Eq. (2). The result is

$$g(\lambda) = \frac{\lambda^5}{K_1 8 \pi n_r^2 h c^2 V d \lambda} \left( 1 - \exp \frac{\frac{hc}{\lambda} - \Delta F}{k_B T} \right) P_{sp}(\lambda). \quad (3)$$

Next the material gain is written in terms of the measured net modal gain as

$$g_m(\lambda) = \Gamma g(\lambda) - \alpha_i, \quad (4)$$

where  $\Gamma$  is the optical confinement factor and  $\alpha_i$  is the intrinsic loss for the optical waveguide mode. Now the modal gain can be written in terms of the measured spontaneous emission power:

$$g_m(\lambda) = \frac{\Gamma \lambda^5}{K_1 8 \pi n_r^2 h c^2 V d \lambda} \left( 1 - \exp \frac{\frac{hc}{\lambda} - \Delta F}{K_B T} \right) \times P_{sp}(\lambda) - \alpha_i \quad (5)$$

or, more simply, as

$$g_m(\lambda) = Q \lambda^5 \left( 1 - \exp \frac{\frac{hc}{\lambda} - \Delta F}{k T} \right) P_{sp}(\lambda) - \alpha_i. \quad (6)$$

In the above expression, there are three parameters which relate gain to spontaneous emission: the transparency energy  $\Delta F$ , the loss  $\alpha_i$ , and the constant  $Q$ , which includes the optical coupling constant. The losses, which actually vary slightly as a function of wavelength, are assumed constant in this technique. That is, the determination of the transparency energy is equivalent to determining the losses, since the material gain at that energy is zero. The coupling constant and transparency energy are therefore used as fitting parameters for each pair of gain and spontaneous emission spectra.

In principle it should be possible to fix the value of the coupling constant when matching a pair of gain and spontaneous emission spectra, and use that fixed value for subsequent matches. Alternatively, the best-fit matches of the gain and spontaneous emission spectra ought naturally to result in a uniform value for the coupling constant. Recent studies<sup>20-22</sup> employing this technique, however, have permitted some variation in the coupling constant from spectrum to spectrum. But allowing the coupling constant to fluctuate, even by a few percent, can lead to significant changes in the extracted values of transparency energy and loss. Therefore it is necessary to consider whether it is valid to allow the coupling constant to vary for each pair of gain and spontaneous emission spectra.

In the experiments the spontaneous emission spectra are measured from the side of the laser using a bare fiber. It is possible to mount the fiber rigidly and isolate it from vibration and air currents so that the position of the fiber is held constant. The test laser is temperature controlled and biased at a constant current, and monitored throughout the duration of the experiments. When the total spontaneously emitted power is measured and observed for stability, it varies by less than one percent over times comparable to the duration of the experiment. Thus, it does not seem reasonable to allow the coupling coefficient to vary in the fitting procedure.

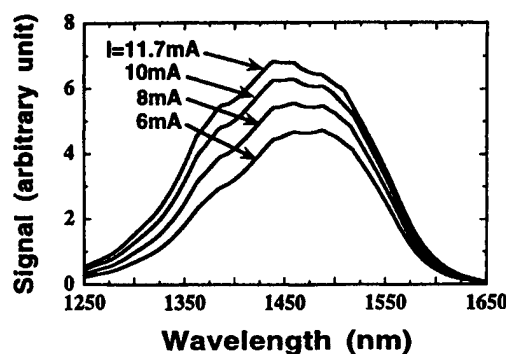


FIG. 1. The spontaneous emission spectra at four injection currents,  $I=6, 8, 10$ , and  $11.7$  mA, in increasing order. The wavelengths corresponding to the gain spectra extending from  $1500$  to  $1650$  nm.

It is also worthwhile to consider wavelength dependence of the coupling coefficient. A multimode silica core fiber was used to couple the spontaneous emission. Figure 1 shows the spontaneous emission for four injection currents up to laser threshold. Here the portion of the spontaneous emission spectrum which is transferred to obtain gain spectra is at wavelengths of  $1500$  up to  $1650$  nm. In coupling to the fiber, small variations in the glass refractive index (from  $1.44462$  to  $1.44267$ ) lead to variation in the reflectivity, and a simple estimate can be made using the Fresnel formula, i.e.,

$$R = \frac{(n_e - 1)^2}{(n_e + 1)^2} \quad (7)$$

in which  $n_e$  is the effective refractive index of the fundamental mode of the fiber. The reflectivity changes from  $3.31\%$  to  $3.28\%$  over the wavelength range of  $1500$ – $1650$  nm used to match gain and spontaneous emission. Absorption within the fiber is negligible. So, a  $0.1\%$  variation in the coupling may be reasonable, though in obtaining these results the coupling constant was not varied with respect to wavelength.

Polarization dependent gain data are extracted by measuring the ASE spectra through a polarizing laser-optical fiber interface. The gain is then calculated using the Hakki-Paoli method, in which the ratio of intensity maxima and minima of the Fabry-Perot modes is related to the gain.<sup>1</sup> As mentioned earlier, this technique relies on a good signal to noise ratio, which may be insufficient for wavelengths near the band edge where the ASE intensity is extremely low. In the peak gain region for currents near threshold, the modes are almost lasing and may not be completely resolved by the spectrometer. The mode maxima become artificially lowered and the Hakki-Paoli method underestimates the gain. In this region, Cassidy's method, employing the ratio of the average mode power to the mode minimum, is less susceptible to these effects. For our gain measurements, the Hakki-Paoli technique is used at nearly all wavelengths, except near the peak gain at just below threshold, where Cassidy's method is employed.

To obtain the best fit results from Eq. (6), we choose a constant value of  $Q$  to be used for each of the currents. The quasi-Fermi level of separation  $\Delta F$  is then varied for each current to yield transformed spontaneous emission spectra

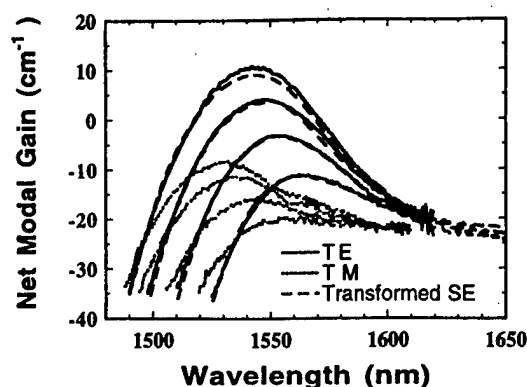


FIG. 2. Measured net modal gain spectra (solid-TE polarization, dotted-TM polarization) and transformed spontaneous emission spectra (dashed-TE polarization) are shown for injection current  $I=6, 8, 10$ , and  $11.7$  mA. Note the tail regions of the transformed spectra (on the long-wavelength side), which show closer agreement for TE and TM polarizations.

with the smallest deviation from the measured modal gain. The value of  $Q$  which is selected is that which gives the best simultaneous fit for all the spectra. The resulting transformed gain spectra then provide accurate gain data in the tail region where none was available from the direct measurement using the Hakki-Paoli or Cassidy's method.

The measured net modal gain spectra,  $\Gamma g - \alpha_i$ , (solid-TE polarization, dotted-TM polarization) are shown in Fig. 2 with the transformed spontaneous emission based on the above fitting techniques. Overall the agreement is quite good; but the improvement is most noticeable in the tail region, where the transformed spectra (dashed) show significantly less noise than the TE spectra (solid). It is interesting to note the tail of the TE gain spectra, which initially appear to taper off at a loss value different than that of the TM spectra. The transformed data show that the actual tail reaches a loss point in much closer agreement with the measured TM losses. The extracted values of transparency energy and loss are shown in Figs. 3(a) and 3(b), respectively. Also shown for comparison are the values obtained from the independent measurements of the loss and transparency energies<sup>18</sup> described below. The extracted values for all methods are in close agreement. The SE-transform method is no better or worse than the other techniques. The advantage of this method, however, is that the entire gain spectrum can be extracted from the spontaneous emission spectrum, yielding very accurately measured values of transparency energy and loss, and giving a more accurate tail for the gain spectrum.

## B. Method II: Crossing of polarization dependent optical gain spectra

Figure 4 shows the polarization dependent gain spectra obtained from the facet ASE spectrum. The transparency energy may be measured directly by examining the crossing point of the TE and TM gain spectra, and the value of loss at the crossing point is equal to the intrinsic loss. The values extracted from comparison of TE and TM gain spectra are

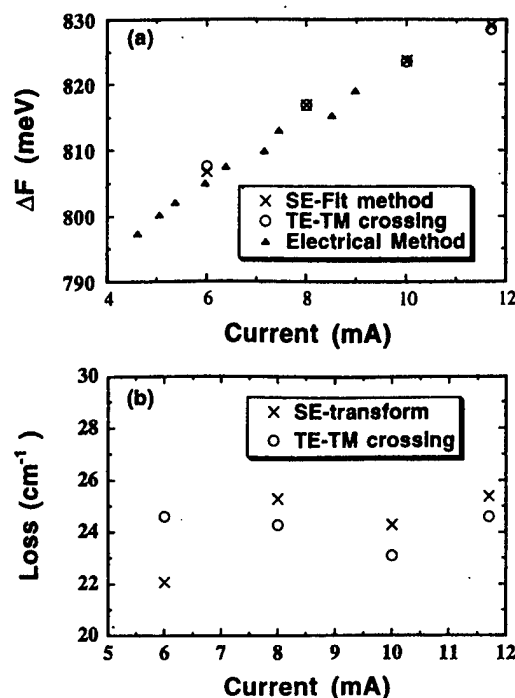


FIG. 3. A comparison of (a) the measured transparency energy based on the TE-TM crossing method (circles), the electrical method (triangles), and the spontaneous emission (SE) transformation method (crosses) and (b) the intrinsic loss using the TE-TM crossing method (circles) and the SE transformation method (crosses).

presented in Fig. 3. There are certain flaws in measuring the loss and transparency in this manner. Because of noise near the gain tail (especially for the TE spectra), it appears that the losses may be polarization dependent. If that is the case, estimates of both loss and transparency energy based on the crossing of the TE and TM gain spectra are questionable. Yet even if the losses were not polarization dependent, measuring them by examining the crossing point of TE and TM spectra is not always straightforward. For instance, the slope

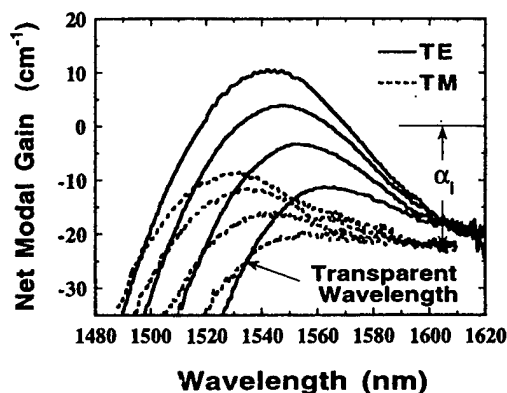


FIG. 4. Polarization dependent gain spectra for currents of 6, 8, 10, and 11.7 mA, from bottom to top curves, are shown. The plateau at the long wavelength sides gives the intrinsic loss. The crossing point of the TE- and TM-polarization gain spectra gives the transparent wavelength at each injection current. Note the apparent discrepancy in the location of the gain tails, which suggests a polarization-dependent intrinsic loss.



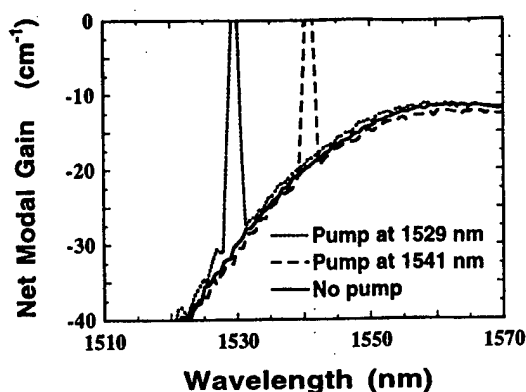


FIG. 5. Gain spectra with (dotted and dashed) and without (solid) an external optical pump. Pump light is absorbed at 1529 nm and amplified at 1541 nm, causing the gain spectrum to be enhanced (dotted) or compressed (dashed), respectively.

of the gain is relatively steep near the crossing point, so that while the measured transparency energy may be relatively accurate, the exact value of loss is much less certain. A more general problem is that it is not always possible to obtain clear TM spectra, especially in compressively strained lasers. Nevertheless, measuring the TE-TM crossing is straightforward, and has the advantage of simplicity.

### C. Method III: Measurement of gain compression in the presence of an external laser pump

One technique for measuring the transparency energy involves measuring the gain of a semiconductor laser with a constant biased current in the presence of an external optical pump. In contrast to measurements of the single-pass gain at the pump wavelength, changes in the overall gain spectrum induced by the absorption or amplification of a pump are examined. If the pump wavelength is located within the gain region, amplification of the pump will consume carriers and reduce the overall gain. Conversely, if the pump wavelength is in the absorption region, the pump will create carriers and enhance the gain. In these experiments an external distributed feedback (DFB) laser is used as the pump source, and it is filtered to prevent the ASE of the pump DFB laser from entering the Fabry-Perot laser under study. Figure 5 shows measured gain spectra at 6 mA with and without an external pump. First the pump is located in the absorption region at 1541 nm, and the gain is enhanced. Then the pump is tuned to the gain region at 1529 nm, and the gain is compressed.

The two pump wavelengths in Fig. 5 are separated by 12 nm or 6.3 meV, which corresponds to an uncertainty in the transparency energy of less than 1 %. This degree of uncertainty in the transparency energy is too large to make an accurate comparison. Fortunately, one can interpolate to improve the estimate, which gives an estimated transparency wavelength of 1535 nm, which is in close agreement with the results obtained by TE-TM crossing method. Likewise, the estimated losses can be interpolated from the pump locations, for an intrinsic loss of  $25 \text{ cm}^{-1}$ .

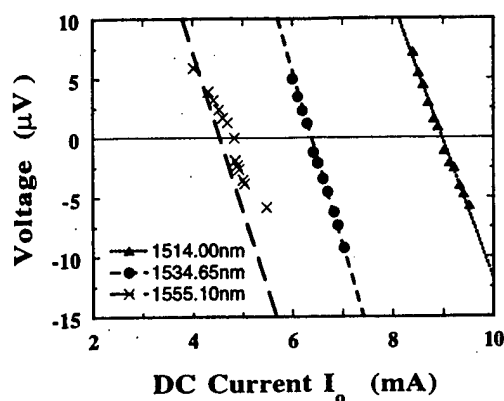


FIG. 6. A plot of the induced ac voltage magnitude across the laser terminals, due to the injection of the modulated external pump laser, as the bias current ( $I_0$ ) of the test laser is varied. When the magnitude of the induced ac voltage is zero, the laser wavelength is at the transparency energy.

While improvement might seem possible by pumping at wavelengths closer to transparency, in practice very high pump powers are required since the absorption or gain becomes very small. Little gain change was observed for pump wavelengths between 1529 and 1541 nm in experiments conducted at a bias of 6 mA, though pump powers as high as 3 mW were used. Other, more subtle problems arise as well; for instance, the sensitivity of this technique varies depending on whether the pump wavelength overlaps a Fabry-Perot resonance or not. If the pump does not overlap a Fabry-Perot maximum, the gain or absorption is weaker and the gain change may be misleadingly small. A slightly different approach based on an electrical characterization technique, described in the next section, overcomes these difficulties and provides superior accuracy in measuring the transparency energy and loss.

### D. Method IV: Measurement of electrical characteristics in the presence of an external laser pump

An excellent method<sup>19</sup> for determining the transparency energy to a high degree of accuracy also involves the use of an external pump laser. In contrast to the preceding method, the pump signal is modulated and injected into the laser under study (test laser) while the ac signal appearing across the test laser terminals is monitored by a lock-in amplifier. A modulating frequency of a few kHz is sufficient for high signal to noise ratio. When using a pump filtered to remove its ASE, the magnitude of the induced ac voltage in the test laser will be a minimum when the pump laser is tuned to the transparency energy. Alternatively, the bias of the laser under test may be varied while the pump laser is fixed. The latter method was used to measure the transparency energy and loss independently. The pump sources used were several single-mode DFB laser operating between 1514 and 1555 nm. Figure 6 shows the measured ac voltage magnitude ver-



sus current for three of the pump wavelengths used. The negative or positive sign in the plot is used to indicate the relative phase. This plot shows that as the pump wavelength is decreased, the current which has that wavelength as the transparency point increases, which is the correct trend. From our measurements, the zero crossings are obtained by fitting a curve to the measured data and taking the fitted zero value. The resulting transparency energies are compared to those of the other methods in Fig. 3(a).

### III. MANY-BODY GAIN THEORY

The optical gain with the Lorentzian line shape function gives an anomalous absorption region below the band gap and discrepancies between the transparency points and the Fermi-level separation. The spontaneous emission transformation method using the fundamental relations between the spontaneous emission and the absorption coefficients guarantees that artifacts related to the Lorentzian line shape are circumvented independent of the line shape functions (Lorentzian, Gaussian, or others). However, the slow convergence of the Lorentzian still leads to a very long tail of the gain spectra into the band gap.<sup>15</sup> Here, a non-Markovian (Gaussian) gain model with many-body effects under the spontaneous emission transformation method is used to calculate the optical gain, and we will show that this model agrees very well with the experimental data in Sec. IV.<sup>16,17</sup>

Under the spontaneous emission transformation method, the optical gain with non-Markovian relaxation and many-body effects is given by<sup>16</sup>

$$g(\omega) = \left(1 - \exp \frac{\hbar\omega - \Delta F}{kT}\right) \sqrt{\frac{\mu_0}{\epsilon}} \left(\frac{e^2}{m_0^2 \omega}\right) \times \int_0^\infty dk_{\parallel} \frac{k_{\parallel}}{\pi L_z} |M_{lm}|^2 f_1^c (1 - f_m^v) (1 - \text{Re} q_{k_{\parallel}}) \times \frac{\text{Re} L[E_{lm}(k_{\parallel})] - \text{Im} q_{k_{\parallel}} \text{Im} L[E_{lm}(k_{\parallel})]}{(1 - \text{Re} q_{k_{\parallel}})^2 + (\text{Im} q_{k_{\parallel}})^2}, \quad (8)$$

where  $\omega$  is the optical angular frequency,  $\mu_0$  is the vacuum permeability,  $\epsilon$  is the dielectric constant,  $k_{\parallel}$  is the in-plane vector,  $L_z$  is the well thickness,  $|M_{lm}|^2$  is the momentum matrix element in the strained QW,  $f_1^c$  and  $f_m^v$  are the Fermi functions for the conduction band states and the valence band states, and  $\Delta F$  is the difference in quasi-Fermi energy levels of the electrons and holes. The indices  $l$  and  $m$  denote the electron states in the conduction band and the heavy hole (light hole) subband states in the valence band. Also,  $E_{lm}(k_{\parallel}) = E_l^c(k_{\parallel}) - E_m^v(k_{\parallel}) + E_g + \Delta E_{SX} + \Delta E_{CH}$  is the normalized transition energy between electrons and holes, where  $E_g$  is the band gap of the material, and  $\Delta E_{SX}$  and  $\Delta E_{CH}$  are the screened exchange and Coulomb-hole contributions to the band gap renormalization. The factor  $q(k_{\parallel})$  is the excitonic or Coulomb enhancement of the interband transition probability.<sup>23,24</sup> The line shape function  $[E_{lm}(k_{\parallel})]$  is Gaussian for the simplest non-Markovian quantum kinetics and is given by<sup>16,17</sup>

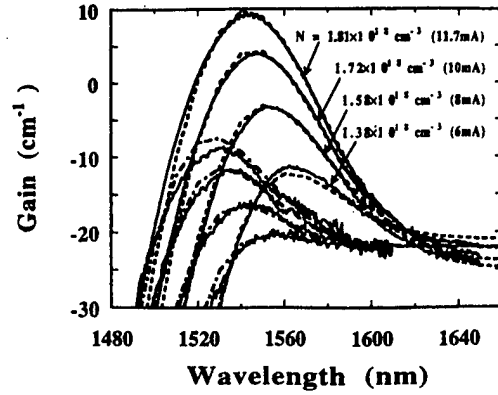


FIG. 7. The measured gain spectra (solid curves) and theoretical fits (dashed lines) using a many-body gain model are shown for both TE (upper group of curves) and TM (lower group) polarizations.

$$\text{Re} L(E_{lm}(k_{\parallel})) = \sqrt{\frac{\pi \tau_{in}(k_{\parallel}) \tau_c}{2 \hbar^2}} \times \exp\left(-\frac{\tau_{in}(k_{\parallel}) \tau_c}{2 \hbar^2} E_{lm}^2(k_{\parallel})\right) \quad (9)$$

and

$$\text{Im} L(E_{lm}(k_{\parallel})) = \frac{\tau_c}{\hbar} \int_0^\infty \exp\left(-\frac{\tau_c}{2 \tau_{in}(k_{\parallel})} t^2\right) \times \sin\left(\frac{\tau_c E_{lm}(k_{\parallel})}{\hbar} t\right) dt. \quad (10)$$

The intraband relaxation time  $\tau_{in}$  and correlation time  $\tau_c$  are assumed to be 85 and 20 fs in our calculations, respectively, for the best fit with the experimental data. The valence band structure is calculated by using the block-diagonalized  $3 \times 3$  Hamiltonian based on the  $\mathbf{k} \cdot \mathbf{p}$  method.<sup>25</sup>

### IV. COMPARISON OF THEORETICAL AND EXPERIMENTAL RESULTS AND DISCUSSION

Figure 7 shows the comparison between experimental (solid curves) and calculated (dashed curves) TE and TM gain spectra for the lattice-matched InGaAlAs multi-QW laser. The structural details are summarized in Table I. Experimental data are measured at injection currents,  $I = 6, 8, 10$ , and 11.7 mA. The corresponding carrier densities are 1.38, 1.58, 1.72, and  $1.81 \times 10^{18} \text{ cm}^{-3}$ , respectively. The carrier

TABLE I. Structure of the laser under study.

Well:	Number of wells	5	SCH width:	600 Å
	Material	InGaAlAs	Stripe width:	1.46 μm
	Strain	lattice matched	Cavity length:	638 μm
	Width	86 Å		
	PL wavelength	0.56 μm		
Barrier:	Material	InGaAlAs		
	Strain	lattice matched		
	Width	50 Å		
	PL wavelength	1.21 μm		

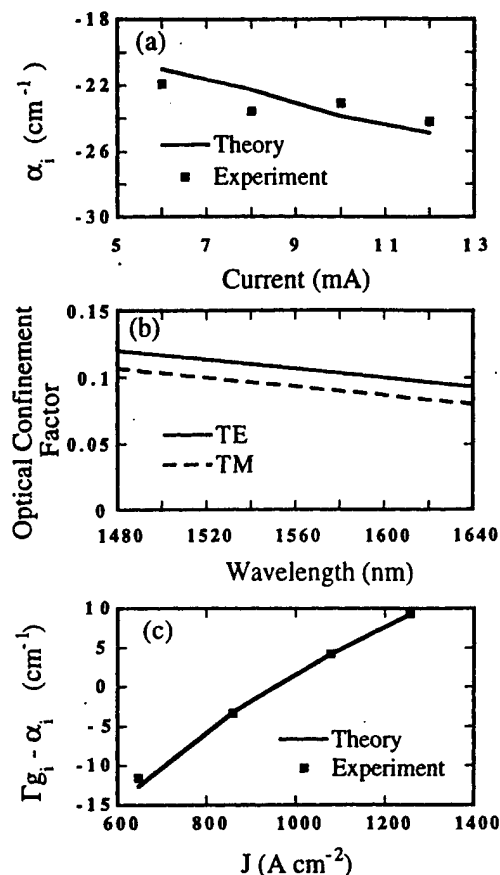


FIG. 8. The measured intrinsic loss and trend for the fits are shown in (a) for the TE polarization. In (b) the optical confinement factors for both polarizations are plotted as a function of wavelength, and in (c) the measured and predicted net modal gain versus the injection current density are shown.

densities are selected to give the best fit to the experimental data. Recently, Shtengel *et al.* showed that the absolute value of the optical loss increases with an increasing current.<sup>26</sup> Here, we obtain the optical losses for the TE polarization equal to  $-21$ ,  $-22.3$ ,  $-23.9$ , and  $-24.9$   $\text{cm}^{-1}$  for 6, 8, 10, and 11.7 mA injection currents, respectively. These values are generally within 1  $\text{cm}^{-1}$  of the best measured values and are plotted in Fig. 8(a); for the 8 mA spectra the losses are within 3  $\text{cm}^{-1}$ . The theoretical gain spectra show reasonably good agreement with the experimental results.

The optical confinement factor  $\Gamma$  per unit width of the quantum well obtained from the fitting result is shown in Fig. 8(b) and is approximately  $1.8 \times 10^{-3} \text{ nm}^{-1}$  at 1.5  $\mu\text{m}$ . This value is in good agreement with that reported for InP-based quantum well lasers.<sup>27</sup> The absolute magnitude of the TE and TM confinement factors differs by about 0.01; the TM polarization being less confined. Variation in the confinement factor with respect to wavelength follows the same trend for each polarization. Confinement decreases with increasing wavelength, since the ratio of the active region length or width to the wavelength is decreasing. In Fig. 8(c), the predicted and measured values of peak net modal gain versus injected current density also show excellent agreement. From these results, we know that the non-Markovian gain model with many-body effects is useful for comparison with experi-

ment. If the Lorentzian line shape is used instead of the Gaussian line shape, it would be difficult to obtain the exact optical losses because the slow convergence of the Lorentzian leads to a very long tail of the gain spectra into the band gap. This is mainly due to the steepness of its low-energy tail in the Gaussian, which is similar to the line shape obtained by considering the carrier-carrier and carrier-longitudinal optical (LO) phonon scatterings.<sup>7,8</sup>

## V. SUMMARY AND CONCLUSIONS

High accuracy measurements of gain, loss and transparency energy in long-wavelength semiconductors based on a hybrid approach using the fundamental relationship between the gain and the spontaneous emission spectra have been demonstrated. Our hybrid approach for the gain spectrum alleviates many of the problems related to the poor signal to noise ratio in the ASE near and below the band edge, yielding more accurate gain data in this region than any of the other available techniques. The values of loss and transparency energy obtained from the spontaneous emission transformation method agree favorably with those obtained from other techniques such as the measurement of polarization dependent gain, and measurements of the gain compression and electrical characteristics in the presence of an optical pump beam. These independent measurements of transparency energy and loss provide validation that our correlated gain and spontaneous emission spectra have a high degree of reliability. We have also compared the measured gain spectra for both polarizations with calculations using a non-Markovian gain model with many-body effects under the spontaneous emission transformation method. This model yields very good agreement to the measured gain spectra.

## ACKNOWLEDGMENTS

This work was support by ONR under Grant Nos. N00014-96-10303 and AASERT N00014-96-1-0902. S. H. Park was also partially supported by Catholic University of Taegu-Hyosang.

- <sup>1</sup>B. W. Hakki and T. L. Paoli, J. Appl. Phys. **46**, 1299 (1975).
- <sup>2</sup>D. T. Cassidy, J. Appl. Phys. **56**, 3096 (1984).
- <sup>3</sup>V. Jordan, IEE Proc.: Optoelectron. **141**, 13 (1994).
- <sup>4</sup>M. Yamada and Y. Suematsu, J. Appl. Phys. **52**, 2653 (1981).
- <sup>5</sup>P. Rees and P. Blood, IEEE J. Quantum Electron. **31**, 1047 (1995).
- <sup>6</sup>M. Yamanishi and Y. Lee, IEEE J. Quantum Electron. **23**, 367 (1987).
- <sup>7</sup>M. Asada, *Quantum Well Lasers*, edited by P. S., Zory, Jr. (Academic, San Diego, CA, 1993), Chap. 2.
- <sup>8</sup>W. W. Chow, P. M. Smowton, P. Blood, A. Girdt, F. Jahnke, and S. W. Koch, Appl. Phys. Lett. **71**, 157 (1997).
- <sup>9</sup>S. H. Park and S. L. Chuang, Appl. Phys. Lett. **72**, 3103 (1998).
- <sup>10</sup>C. F. Hsu, P. S. Zory, C. H. Wu, and M. A. Emanuel, IEEE J. Sel. Top. Quantum Electron. **3**, 158 (1997).
- <sup>11</sup>S. H. Park and S. L. Chuang, Appl. Phys. Lett. **72**, 287 (1998).
- <sup>12</sup>G. Lasher and F. Stern, Phys. Rev. A **133**, 553 (1964).
- <sup>13</sup>C. H. Henry, R. A. Logan, and F. R. Merritt, J. Appl. Phys. **51**, 3042 (1980).
- <sup>14</sup>S. L. Chuang, J. O'Gorman, and A. H. J. Levi, IEEE J. Quantum Electron. **29**, 1631 (1993).
- <sup>15</sup>P. M. Enders, IEEE J. Quantum Electron. **33**, 580 (1997).
- <sup>16</sup>D. Ahn, Prog. Quantum Electron. **21**, 249 (1997).
- <sup>17</sup>S. H. Park and S. L. Chuang, Proc. SPIE **3283**, 314 (1998).
- <sup>18</sup>G. E. Shtengel and D. A. Ackermann, Electron. Lett. **31**, 1157 (1995).

- <sup>19</sup>P. A. Andrekson, N. A. Olsson, T. Tanbun-Ek, R. A. Logan, D. L. Coblentz, and H. Temkin, *Electron. Lett.* **28**, 171 (1992).
- <sup>20</sup>G. Hunziker, W. Knop, P. Unger, and C. Harder, *IEEE J. Quantum Electron.* **31**, 643 (1995).
- <sup>21</sup>A. Schoenfelder, J. D. Ralston, K. Czotscher, S. Weisser, J. Rosenzweig, and E. C. Larkins, *J. Appl. Phys.* **80**, 582 (1996).
- <sup>22</sup>W. Fang, M. Hattendorf, S. L. Chuang, J. Minch, C. S. Chang, C. G. Bethea, and Y. K. Chen, *Appl. Phys. Lett.* **70**, 796 (1997).
- <sup>23</sup>H. Haug and S. W. Koch, *Quantum Theory of the Optical and Electronic Properties of Semiconductors* (World Scientific, Singapore, 1993).
- <sup>24</sup>W. W. Chow, S. W. Koch, and M. Sargent III, *Semiconductor-Laser Physics* (Springer, Berlin, 1993).
- <sup>25</sup>C. S. Chang and S. L. Chuang, *IEEE J. Sel. Top. Quantum Electron.* **1**, 218 (1995).
- <sup>26</sup>G. E. Shtengel, P. A. Morton, R. F. Kazarinov, D. A. Ackerman, M. S. Hybertsen, G. L. Belenky, and C. L. Reynolds Jr., *Proc. SPIE* **2994**, 678 (1997).
- <sup>27</sup>J. P. Loehr and J. Singh, *IEEE J. Quantum Electron.* **27**, 708 (1991).

# Temperature Dependence of Electrical and Optical Modulation Responses of Quantum-Well Lasers

T. Keating, X. Jin, S. L. Chuang, *Fellow, IEEE*, and K. Hess, *Fellow, IEEE*

**Abstract**—We present theory and experiment for high-speed optical injection in the absorption region of a quantum-well laser and compare the results with those of the electrical injection including carrier transport effect. We show that the main difference between the two responses is the low-frequency roll-off. By using both injection methods, we obtain more accurate and consistent measurements of many important dynamic laser parameters, which include the differential gain, carrier lifetime,  $K$  factor, and gain compression factor. Temperature-dependent data of the test laser are presented which show that the most dominant effect is the linear degradation of differential gain and injection efficiency with increasing temperature. While the  $K$ -factor is insensitive to temperature variation for multiple-quantum-well lasers, we find that the carrier capture time and nonlinear gain suppression coefficient decreases as temperature increases.

**Index Terms**—Differential gain, electrical modulation, optical injection, transport effect.

## I. INTRODUCTION

HIGH-SPEED modulation of long-wavelength semiconductor lasers is of major technological importance. The continuing development of high-bandwidth fiber optical communication systems and the unceasing demand for greater data transmission capacity over fiber-optic cables is dependent on the superior qualities offered by semiconductor laser optical transmitters. Long-wavelength lasers, as studied in this paper, are especially useful for long-haul communications since the loss in optical fibers is minimal near wavelengths of 1.55  $\mu\text{m}$ . Practical communication systems based on these lasers also require robust temperature performance for application in ambient, uncooled environments where the device may be required to operate between  $-40^\circ\text{C}$  and  $85^\circ\text{C}$ . To improve these devices, it is therefore important to study their temperature-dependent response and analyze which effects are most responsible for limiting the modulation bandwidth.

The excessive damping that limits the electrical modulation bandwidth of quantum-well (QW) lasers originates from a number of possible mechanisms, including photon lifetime [1], carrier capture and escape [2], [3], carrier diffusion [4], carrier heating [5], [6], spectral hole burning [7], and circuit parasitics [8]. The photons generated by the stimulated recombination

of electrons and holes travel in the cavity. On average, they exist for a certain amount of time and disappear from the cavity due to the intrinsic absorption or transmission from the mirror facets. Therefore, the photon lifetime constitutes an intrinsic limitation on the modulation response. The major sources of carrier heating in semiconductor lasers are injection heating, stimulated recombination heating, and free carrier heating. These changes in the carrier temperature will be reflected in the changes in gain. An increase of a few degrees will result in a decrease in gain of several percent, which appears in the rate equations as a nonlinear gain suppression coefficient. Spectral hole burning theory also predicts an increase in the nonlinear gain suppression coefficient with increasing carrier temperature. Parasitic effects come from the bias circuit and the shunting of modulation current around the active layer, which will cause a low-frequency roll-off of modulation response. The carrier diffusion, capture, and escape times are usually defined to characterize the carrier transport processes [9], which give a parasitic-like roll-off and are indistinguishable from parasitic effects. In QW lasers, the carrier transport effect is an important limit for multiple-quantum-well (MQW) laser modulation bandwidth. In general when the number of wells increases, the modulation bandwidth of the device initially increases, but it is ultimately saturated by the carrier transport effect. This saturation effect was observed in gain-coupled InGaAsP distributed feedback (DFB) lasers with more than eight QW's [10].

A schematic of high-speed modulation by electrical injection and optical injection is shown in Fig. 1. For electrical modulation, the electrons are injected from the outer edge of the left separate-confinement-heterostructure (SCH) region and the holes from the outer edge of the right SCH region. The injected carriers diffuse through the SCH region and are captured into the QW's before recombining by stimulated emission processes. Compared with electrical modulation, optical modulation with an optical energy in the absorption range of the QW directly produces photon-generating carriers inside the test laser's active region via injection of a modulated laser beam through one of the test laser's mirror facets. Therefore, the majority of carriers transporting through the SCH region is not required for lasing action although the coupling between SCH and QW states still exists for optical modulation. In this way, optical modulation removes the severe low-frequency roll-off due to the transport and parasitic effects and helps to clarify the intrinsic response.

In this paper, the high-speed modulation response of a QW DFB laser operating at 1.55  $\mu\text{m}$  is investigated for two types of modulation, electrical and optical. Electrical modulation

Manuscript received March 9, 1999; revised June 16, 1999. This work was supported by the Office of Naval Research under Grant N00014-96-1-0303 and Grant N00014-98-1-0604.

T. Keating, X. Jin, and S. L. Chuang are with the Department of Electrical and Computer Engineering, University of Illinois at Urbana-Champaign, Urbana, IL 61801 USA.

K. Hess is with the Department of Electrical and Computer Engineering and the Beckman Institute, University of Illinois at Urbana-Champaign, IL 61081 USA.

Publisher Item Identifier S 0018-9197(99)07609-5.

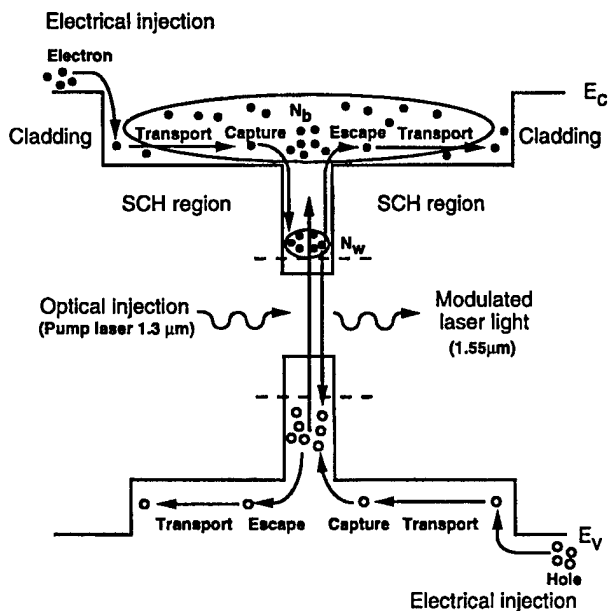


Fig. 1. Energy-band QW potential diagram for high-speed modulation by optical or electrical injections. For electrical injection, the carriers have to transport and get captured by the QW's. For optical injection, we choose the optical pump energy such that carriers are generated in the wells.

is performed by applying a microwave signal directly on the injection current of the test laser. Optical modulation is performed by injecting light from a second pump laser operating at  $1.3\text{ }\mu\text{m}$  which itself is being directly modulated electrically, so that the injected light is absorbed in the QW's of the  $1.55\text{-}\mu\text{m}$  test laser. Both sets of responses are compared with theory in order to extract the values of the fundamental parameters which determine as well as limit the modulation bandwidth. Optical injection at this wavelength eliminates circuit parasitic and carrier transport effects, and the intrinsic laser response can be directly measured [11], [12]. Our experiment differs from the experiment performed in [11], where the optical injection is at a wavelength close to that of the test laser. Therefore, competition of carriers and gain saturation have to be considered for both the pump and test wavelengths. We inject pump signal into the center of the active waveguide region of the test laser to avoid the spatial effects on the optical modulation and optimize the modulation response. It has been shown [14] that the optical modulation response can be influenced by the spatial characteristics (the spot size and its position) of the pump light. Our setup is similar to that in [15], where the intrinsic absorption of the pump light modulates the test laser output. However, little work has been performed so far on directly comparing the electrical and optical modulation response at different temperatures. We show data for temperature dependence of both optical and electrical injection. To analyze the basic parameters controlling the modulation response, the simplest approach is to use rate equations for the cavity photon density and modulated carrier density. Rate equations provide a reasonable description of most of the observed phenomena.

This paper is organized as follows. In Section II, the optical modulation theory is presented and compared with that of electrical modulation including transport effects. In Section III,

our experimental setup is described and comparisons between optical and electrical modulation responses are made, and the extracted high-speed parameters are shown. Finally, the temperature dependence of important laser parameters are discussed in Section IV.

## II. RATE EQUATIONS FOR OPTICAL AND ELECTRICAL MODULATION

Fig. 1 shows a typical SCH QW laser. We will model the carrier transport (diffusion, capture, and emission) in such a laser structure and study its effects on the small-signal modulation with electrical injection and optical injection. Our objective is to calculate the small-signal frequency response of the test laser for optical modulation from the pump laser and use the same rate equations with a different source term to derive the electrical modulation response of the test laser. In general, transport effects for electrical microwave modulation can be modeled by taking into account the carrier density in the SCH region, the carrier density in the well region, and the photon density separately [9]. Coupling of the carrier density in the barrier states above the QW's to the carrier density in the QW's is modeled by two terms representing carrier capture and escape into or from the wells, respectively. In this case, three rate equations are needed. The source term enters through the injection current in electrical modulation. The model considers carrier injection from the outer edges of the SCH region, diffusion across the SCH region, and the subsequent capture and emission of carriers by the QW. For optical injection using an external pump laser, the pump photon density  $S_p$  acts as the source term. Since the optical energy of the pump laser determines whether the photons are absorbed in the well or in the barriers, we choose the pump wavelength to be longer than the bandgap wavelength of the barriers and shorter than the bandedge wavelength of the wells so that absorption occurs only in the wells. The rate equations for both cases are written as

$$\frac{dN_b}{dt} = \frac{\eta_{inj} I}{q V_b} - \frac{N_b}{\tau_b} - \frac{N_b}{\tau_{bw}} + \frac{N_w V_w}{\tau_{wb} V_b} \quad (1)$$

represents the photon generation due to optical pumping at the wavelength (1.3  $\mu\text{m}$ ) where the optically injected photons are absorbed in the well regions.  $S_p$  is the pump photon density, and  $\alpha_p$  is the absorption at the pump wavelength. The above model is often referred to as the reservoir model [9] and is equivalent to models which incorporate additional effects such as diffusive transport [14]. A spontaneous emission term has been ignored in (3) for above threshold operation.

Assuming a small-signal optical injection due to the external pump laser

$$S_p(t) = S_{p0} + s_p(\omega)e^{j\omega t} \quad (4)$$

where the test laser is biased at a dc current  $I(t) = I_0$  above threshold. The responses can be solved by assuming

$$S(t) = S_0 + s(\omega)e^{j\omega t} \quad (5)$$

$$N_b(t) = N_{b0} + n_b(\omega)e^{j\omega t} \quad (6)$$

$$N_w(t) = N_{w0} + n_w(\omega)e^{j\omega t} \quad (7)$$

and

$$G(N_w) = G(N_{w0}) + g'(N_w - N_{w0}) \quad (8)$$

where  $g'$  is the differential gain of the test laser, and  $N_{w0}$  is steady-state carrier density in the QW.

Substituting (4)–(8) into (1)–(3), the steady-state quantities can be obtained by setting the time-dependent terms to zero. Then, the small-signal equations for the time-dependent terms give

$$j\omega n_b = 0 - \frac{n_b}{\tau_b} - \frac{n_b}{\tau_{bw}} + \frac{n_w V_w}{\tau_{wb} V_b} \quad (9)$$

$$j\omega n_w = \frac{n_b V_b}{\tau_{bw} V_w} - \frac{n_w}{\tau_w} - \frac{n_w}{\tau_{wb}} - v_g \left[ \frac{G_0 s}{1 + \epsilon S_0} - \frac{G_0 S_0 \epsilon s}{(1 + \epsilon S_0)^2} + \frac{g' S_0 n_w}{1 + \epsilon S_0} \right] + v_g \alpha_p S_p \quad (10)$$

$$j\omega s = \Gamma v_g \left[ -\frac{G_0 S_0 \epsilon s}{(1 + \epsilon S_0)^2} + \frac{g' S_0 n_w}{1 + \epsilon S_0} \right] \quad (11)$$

where the steady-state gain-loss relations  $\Gamma v_g G_0 / (1 + \epsilon S_0) = 1/\tau_p$ , and the Taylor expansion  $1/(1 + \epsilon S) = 1/(1 + \epsilon S_0) - \epsilon s / (1 + \epsilon S_0)^2$  are used. This set of small-signal equations can be reduced by eliminating  $n_b$  and  $n_w$  to give a relationship

shown in (12), at the bottom of the page, between the test laser signal  $s(\omega)$  and the pump signal  $s_p(\omega)$ .

The optical modulation response can be written in a normalized form

$$\frac{M(\omega)}{M(0)} = \frac{\omega_r^2}{\omega_r^2 - \omega^2 + j\omega\gamma} \quad (\text{optical}) \quad (13)$$

where

$$\omega_r^2 = \frac{(v_g g' / \chi) S_0}{\tau_p (1 + \epsilon S_0)} \left( 1 + \frac{\epsilon}{v_g g' \tau_w} \right) \quad (14)$$

$$\gamma = \frac{(v_g g' / \chi) S_0}{1 + \epsilon S_0} + \frac{\epsilon S_0}{(1 + \epsilon S_0) \tau_p} + \frac{1}{\chi \tau_w} \quad (15)$$

$$\chi = 1 + \frac{\tau_{bw}}{\tau_{wb}} \quad (16)$$

For a small-signal electrical injection,  $I(t) = I_0 + i(\omega)e^{j\omega t}$ , with no external pump,  $S_p(t) = 0$ . The resulting modulation response is given by [9] and [21] in (17), shown at the bottom of the page, which can be written in the form

$$\frac{M(\omega)}{M(0)} = \frac{\omega_r^2}{(1 + j\omega\tau_{bw})(\omega_r^2 - \omega^2 + j\omega\gamma)} \quad (\text{electrical}) \quad (18)$$

where  $\tau_{bw}$  is a constant which contributes to low-frequency roll-off. The interpretation of this effect is not straightforward. The roll-off in the modulation response derived above is equivalent to the roll-off caused by a simple electrical parasitic, such as a capacitance in parallel to the device. However, in real devices, the effective capacitance may be bias-dependent since the device capacitance is related to the storage of charge in the forward-biased junction. The charge storage itself results from a combination of effects including transport and carrier heating and is difficult to model in terms of a small number of rate equations [15]–[17]. Despite these difficulties, the modulation response can be matched very well for the experiments here with a single total roll-off frequency  $f_p$  for a given temperature. If the transport effect dominates, the roll-off frequency of the transport effect is  $f_p = 1/(2\pi\tau_{bw})$ . In this case, we can measure the carrier diffusion and capture time of the QW.

Because the stimulated emission occurs in the QW's, the carrier lifetime in the SCH or barrier region is usually very

$$\begin{aligned} M(\omega) &= \frac{s(\omega)}{s_p(\omega)} \\ &= \frac{V_g^2 \alpha_p \Gamma g' S_0}{\left[ j\omega \left( 1 + \frac{j\omega\tau_{bw} + \tau_{bw}/\tau_b}{j\omega\tau_{wb}(j\omega\tau_{bw} + 1 + \tau_{bw}/\tau_b)} \right) + \frac{1}{\tau_w} + \frac{S_0 g' v_g}{1 + \epsilon S_0} \right] \left( j\omega + \frac{\epsilon S_0}{\tau_p(1 + \epsilon S_0)} \right) + \frac{v_g g' S_0}{\tau_p(1 + \epsilon S_0)^2}} \end{aligned} \quad (12)$$

$$\begin{aligned} M(\omega) &= \frac{s(\omega)}{i(\omega)} \\ &= \frac{\frac{\eta_{inj}}{qV_w}}{(1 + j\omega\tau_{bw})} \frac{V_g \Gamma g' \frac{S_0}{(1 + \epsilon S_0)}}{\left\{ \left[ j\omega \left( 1 + \frac{\tau_{bw}}{\tau_{wb}(j\omega\tau_{bw} + 1)} \right) + \frac{1}{\tau_w} + \frac{S_0 g' v_g}{1 + \epsilon S_0} \right] \left[ j\omega + \frac{\epsilon S_0}{\tau_p(1 + \epsilon S_0)} \right] + \frac{v_g g' S_0}{\tau_p(1 + \epsilon S_0)^2} \right\}} \end{aligned} \quad (17)$$

TABLE I  
SUMMARY OF ELECTRICAL AND OPTICAL MODULATION RESPONSES

Electrical Pumping and 1.3 $\mu\text{m}$ Optical Pumping	
Electrical	Optical
$\frac{M(\omega)}{M(0)} = \frac{\omega_r^2}{(1+j\omega\tau_{bw})(\omega_r^2 - \omega^2 + j\omega\gamma)}$	$\frac{M(\omega)}{M(0)} = \frac{\omega_r^2}{\omega_r^2 - \omega^2 + j\omega\gamma}$
$\gamma = \frac{1}{\tau_w\chi} + \frac{v_g g' S_0}{\tau_p \chi (1 + \epsilon S_0)} \left( \tau_p + \frac{\epsilon \chi}{v_g g'} \right)$	
$\omega_r^2 = \frac{S_0 v_g g'}{\tau_p \chi (1 + \epsilon S_0)} \left( 1 + \frac{\epsilon}{\tau_w v_g g'} \right)$	
$\chi = 1 + \frac{\tau_{bw}}{\tau_{wb}}$	

long, so we set  $\tau_{bw}/\tau_b \ll 1$  in (12). The modulation responses for both injections are summarized in Table I. Thus the comparison between the optical and electrical modulations is clear. The relaxation frequency  $\omega_r = 2\pi f_r$ , and damping factor  $\gamma$  for both cases are the same. The transport factor  $\chi = 1 + \tau_{bw}/\tau_{wb}$  has also been introduced to the equations. The only difference between the two responses is that optical injection has no low frequency roll-off, which corresponds to transport effects. There would also be a difference when the number of wells is varied. Thus, optical modulation gives an intrinsic modulation response of a laser since the injected pump light is chosen such that the pump light is absorbed only in the well region.

For optical injection, the carriers are injected directly into the QW region, which removes the requirement of carrier transport from the SCH region to the QW region before lasing. In other words, optical injection removes the low-frequency roll-off caused by carriers transporting through SCH region. However, the SCH and QW regions are still coupled together. There are always carriers being captured by and escaping from the QW's. The rate of capture and escape will influence the modulation response intrinsically. Therefore, because of the SCH structure, carrier diffusion capture-escape still affects the optical modulation response, which comes in through the  $\chi$  factor. Thus, the effective differential gain is reduced by a factor of  $\chi$  for the same photon density. This reduction is present even in the absence of low-frequency roll-off in the optical injection, which results in the reduction of the resonance frequency. The effective carrier recombination lifetime in the well is also increased by a factor of  $\chi$ , and the nonlinear gain suppression coefficient remains unchanged. Another important factor in high-speed modulation is the  $K$  factor, which is the slope of the damping factor versus relaxation frequency squared

$$\gamma = K f_r^2 + \frac{1}{\chi \tau_w} \quad (19)$$

$$K = 4\pi^2 \left( \tau_p + \frac{\epsilon}{v_g g' \chi} \right). \quad (20)$$

The  $K$  factor is usually used to determine the maximum possible modulation bandwidth  $f_{\max} = 2\pi \sqrt{2/K}$ . A small  $K$  factor means a large laser bandwidth. Even if we use optical injection modulation, the carrier capture and escape processes still increase the  $K$  factor and limit the maximum modulation. The above parameters characterize the intrinsic modulation response of semiconductor lasers.

TABLE II  
STRUCTURE OF THE TEST LASER

Well:	Number of wells	7	SCH width:	705 Å
	Material	InGaAsP	Stripe width:	1.2 $\mu\text{m}$
	Strain	-1.6% comp.	Cavity length:	400 $\mu\text{m}$
	Width	70 Å		
	PL wavelength	1.5564 $\mu\text{m}$		
Barrier:	Material	InGaAsP		
	Strain	lattice-matched		
	Width	100 Å		
	PL wavelength	1.255 $\mu\text{m}$		

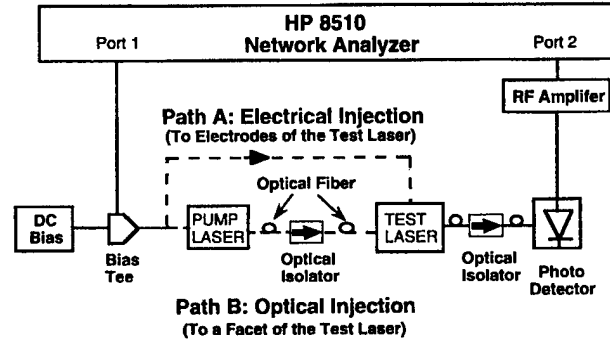


Fig. 2. Schematic diagram of electrical and optical modulation experiment. Path A is for electrical injection experiment. Path B is for optical injection experiment with a 1.3- $\mu\text{m}$  pump.

### III. EXPERIMENTAL RESULTS

The high-speed modulation response of a buried heterostructure MQW DFB laser was measured. The composition of the undoped active region is described in Table II. The barrier photoluminescence wavelength peak occurs at 1.255  $\mu\text{m}$ . Therefore, pump light at 1.3  $\mu\text{m}$  will be absorbed in the QW's.

A schematic diagram of the modulation response experiments is shown in Fig. 2. The laser is held at constant temperature and measurements are made at 20°C, 25°C, 30°C, 35°C, and 40 °C. In the electrical modulation experiments, shown as path A in Fig. 2, the HP 8510 network analyzer provides a small microwave signal (0 dBm) at frequencies swept from 45 MHz to 10 GHz, which is coupled to the test laser electrodes through a bias-T and a high-speed probe. The laser light is coupled to a fiber using a lensed fiber-optical interface and travels through an optical isolator before being measured by a high-speed (29 GHz) photodetector. The small-signal response is increased by an 18-dB-gain RF amplifier before entering the network analyzer, which measures the magnitude of the modulation response  $|M(\omega)/M(0)|^2$ . The data are averaged to reduce noise. The optical response measurements shown as path B in Fig. 2 are similar to electrical modulation experiments, except that a 1.3- $\mu\text{m}$  pump laser with a wide bandwidth is modulated electrically, and its modulated optical output is injected into the test DFB laser facet. The modulation of the pump laser is recorded at a fixed bias and stored for the calibration of the optical response of the 1.55- $\mu\text{m}$  test laser. The pump light is completely absorbed in the test laser, so the light coupled out of the test laser does not require additional filtering of the pump light.

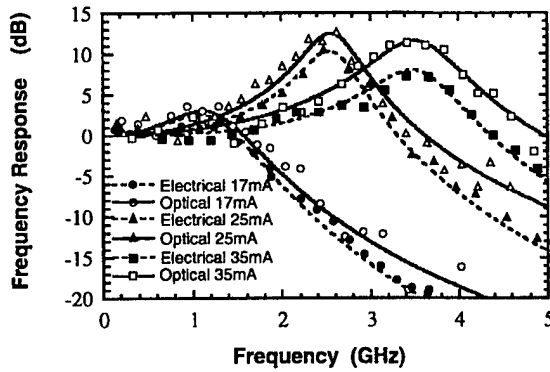


Fig. 3. Normalized modulation response,  $10 \log(|M(\omega)/M(0)|^2)$ , due to electrical injection and optical injection at  $1.3 \mu\text{m}$ . The solid and dashed lines are theoretical modulation responses using (13) and (18), and symbols are measurement results.

The electrical and optical modulation responses are first compared at a fixed temperature of  $20^\circ\text{C}$ . Fig. 3 shows the least-square fits of the measured modulation responses using the theory derived above for electrical and optical injections. The fits are used to extract the differential gain and nonlinear gain suppression factor. In general, the optical injection measurements exhibit more noise than the electrical injection measurements, since the system losses are higher for the optical injection experiments. However, the optical modulation responses have less parameters to fit, which means less freedom of choosing a number. On the other hand, the electrical modulation responses usually have a higher signal-to-noise ratio and more parameters to be handled than the optical modulation. Thus, simultaneously fitting electrical and optical modulation responses can compensate each method's shortage and obtain more accurate laser parameters. Also, by comparing the two responses, the roll-off frequency  $f_p$  can be obtained more accurately. Both modulation responses show clearly that the relaxation peaks increase in frequency as the dc bias is increased. The modulation responses due to optical injection exhibit a slower roll-off at high frequencies, which indicates the absence of low-frequency pole on the optical response. Also, the peak of the optical pump response is generally higher than that of the electrical, and the differences between the two responses increase with increasing current. For 35-mA current injection, electrical modulation has very obvious roll-off because the roll-off frequency is 3.52 GHz at this temperature ( $20^\circ\text{C}$ ). Fig. 4 shows that the roll-off frequency  $f_p$  at various temperatures from  $20^\circ\text{C}$  to  $40^\circ\text{C}$  is independent of the current bias. As we discussed before, the shunt capacitance of parasitic effects may be bias-dependent, and the roll-off frequency of the transport effect is only determined by carrier diffuse-capture time  $\tau_{bw}$ . Although we cannot exclude the parasitic effects, we still can see that the transport effects are more important than the parasitic effects for this DFB laser.

In Fig. 5(a), the relaxation frequency squared is plotted versus optical power. The slope of the linear fit will be used later to extract the differential gain. The damping factor is calculated using extracted parameters from the modulation responses and is plotted in Fig. 5(b). The slope of the linear fit at large relaxation frequency is the  $K$  factor. The deviation at

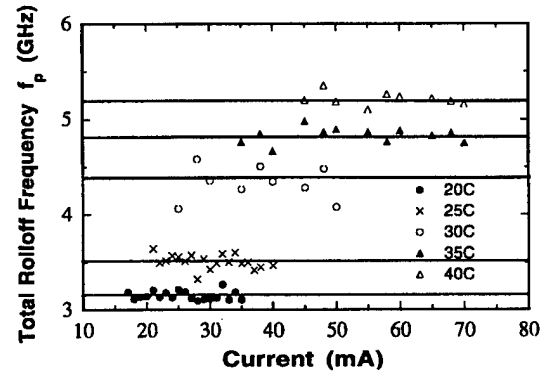
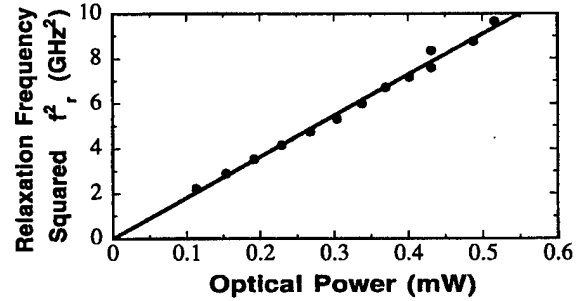
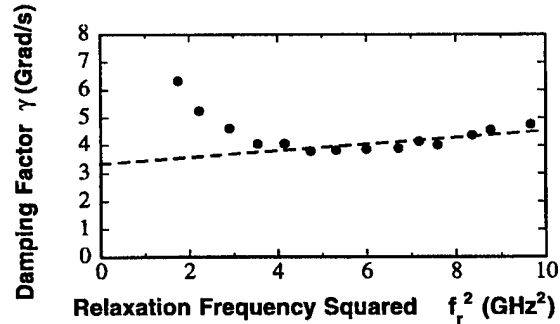


Fig. 4. The total roll-off frequency ( $f_p = 1/2\pi\tau_{bw}$ ) versus the bias current at different temperature. The solid line is the average value of roll-off frequency.



(a)



(b)

Fig. 5. (a) The relaxation frequency squared versus optical power at  $20^\circ\text{C}$ . The line is the least-square fit to the data using (14). (b) The damping factor versus the relaxation frequency squared at  $20^\circ\text{C}$ . The dash line is the linear fit for large relaxation frequency, with a slope equal to the  $K$  factor.

the low-frequency end between the data and the linear dashed line is due to the negligence of the spontaneous emission term. If we include the spontaneous emission factor  $R_{sp}$ , the damping factor should have an additional term  $R_{sp}/S$  which can be neglected at high photon density  $S$  (corresponding to a large relaxation frequency). The complete set of extracted parameters at  $20^\circ\text{C}$  is listed in Table III. The differential gain and nonlinear gain suppression coefficient are well within the values typically found in the literature.

#### IV. TEMPERATURE DEPENDENCE

It is important to determine which factors affecting the modulation responses are most sensitive to temperature. The



TABLE III  
HIGH-SPEED LASER PARAMETERS AND EXTRACTED VALUES AT 20 °C, USING SIMULTANEOUS FITTING OF THE ELECTRICAL AND OPTICAL MODULATION RESPONSES

Parameter	Symbol	Value	Error
Carrier lifetime	$\tau_w$	0.37 ns	$\pm 0.05$ ns
Effective differential gain	$g'/\chi$	$1.32 \times 10^{-15} \text{ cm}^2$	$\pm 0.01 \times 10^{-15} \text{ cm}^2$
K factor	$K$	0.20 ns	$\pm 0.06$ ns
Nonlinear gain suppression coefficient	$\epsilon$	$3.11 \times 10^{-17} \text{ cm}^3$	$\pm 0.5 \times 10^{-17} \text{ cm}^3$
Photon lifetime	$\tau_p$	2.4 ps	$\pm 0.2$ ps
Intrinsic loss	$\alpha_i$	$20 \text{ cm}^{-1}$	$\pm 2 \text{ cm}^{-1}$
Mirror loss	$\bar{\alpha}$	$30 \text{ cm}^{-1}$	$\pm 3 \text{ cm}^{-1}$
Group velocity	$v_g$	$8.5 \times 10^9 \text{ cm/s}$	$\pm 0.1 \times 10^9 \text{ cm/s}$
Injection efficiency	$\eta_{inj}$	0.32	$\pm 0.1$
Width	$w$	1.25 $\mu\text{m}$	
Well width	$L_w$	7 nm	
Barrier width	$L_b$	10 nm	
SCH width	$L_{sch}$	70.5 nm	
Number of wells	$N_w$	7	
Active volume	$V$	$1.2 \times 10^{-10} \text{ cm}^3$	
Optical coupling constant	$\eta_c$	0.10	$\pm 0.05$
Optical confinement factor	$\Gamma$	0.06	$\pm 0.01$

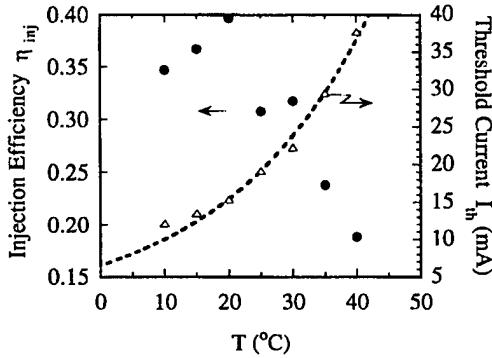


Fig. 6. The injection efficiency and threshold current as a function of temperature. The efficiency degrades severely with temperature. The solid line shows the trend. The dashed line is fitting of threshold current using the formula  $I_{th} = I_0 e^{T/T_0}$ , where  $T_0 = 24$  K.

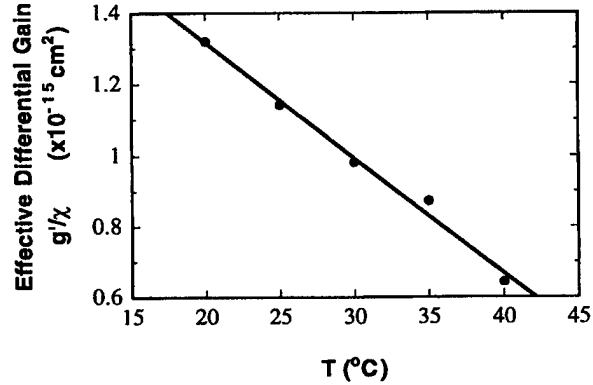


Fig. 7. The effective differential gain ( $g'/\chi$ ) as a function of temperature, showing strong degradation with temperature.  $\chi = 1 + \tau_{bw}/\tau_{wb}$  accounts for carrier transport/capture effect.

fitting procedure described above is applied to each set of modulation responses at each temperature. In Fig. 6, the injection efficiency and threshold current of the test laser are plotted versus temperature. This plot is obtained from measured  $L$ - $I$  curves. The injection efficiency is defined as the fraction of current above threshold which results in the radiative recombination. A fraction of the injected current in InGaAsP lasers is lost (by nonradiative recombination or carrier leakage) at high temperatures, and this fraction does not contribute to radiative recombination or optical gain. The injection efficiency degrades relatively severely with temperature, by a factor of more than two over the 30° temperature increase (about 10% in absolute temperature). The injection efficiency acts to change the modulation response primarily by reducing the overall magnitude of the response. Indirectly, however, the wasted carriers may contribute to the forward bias capacitance, further influencing the modulation response. An exponential temperature dependence of the threshold current is generally used, and the overall characteristic temperature  $T_0$  is 24 K for this laser, which indicates a large dependence on temperature.

A higher carrier density is necessary to achieve the threshold gain condition with increasing temperature. This results in the nonradiative recombination current being a large fraction of the total current. Several mechanisms have been proposed to explain the observed high-temperature sensitivity of the threshold current of InGaAsP lasers. These are carrier leakage over the heterojunction, Auger recombination, and intervalance band absorption.

The effective differential gain ( $g'/\chi$ ) also shows a strong temperature dependence and is plotted in Fig. 7. Over the temperature range plotted, the differential gain decreases by a factor of approximately two, which shows a linear function of the temperature [27]. This effect is due to the temperature dependence of the Fermi distribution, the carrier density, and the intrinsic transition linewidth broadening. However, it is difficult to isolate the significance of each quantity on the temperature dependence of a laser because so many physical phenomena are involved. It can be interpreted as follows. The broadening of the Fermi occupation probability function with increasing temperature spreads the carriers over a larger

energy range for a given overall carrier density. The result is a lower spectral concentration of inverted carriers, which leads to a broadening and flattening of the gain spectrum. Thus, the gain is higher at lower temperatures for the same carrier density, and the carrier density required to achieve a particular gain increases with temperature. In addition, thermionic emission of electrons from the QW to the barrier region is also enhanced at high temperatures. These effects contribute to strong recombination outside the QW and carrier leakage. Since the increased carrier population in the barrier region does not contribute to the optical gain, the differential gain decreases rapidly at high temperatures. This decrease in gain strongly reduces the modulation bandwidth [13]. The differential gain plays a central role in determining the fundamental frequency response of semiconductor lasers since the intrinsic direct modulation speed varies as the square root of the differential gain at the operating carrier density and wavelength.

In Fig. 8(a), the carrier lifetime  $\tau_w$  in the QW's is plotted and shows a decrease with increasing temperature. The carrier lifetime is expected to shorten with increasing temperature, since in 1.55- $\mu\text{m}$  devices the carrier recombination is dominated by Auger recombination [18], which is strongly temperature-dependent. In Fig. 8(b), the total roll-off frequency is plotted versus temperature, showing an increase with increasing temperature. Usually, the low-frequency roll-off is a combination of the effects of the shunt capacitance, external circuit parasitic, and internal transport effect. As for the transport effect, the carrier diffusion and capture time across the SCH region ( $\tau_{bw}$ ) is usually limited by the hole diffusion time, which is insensitive (for MQW's) or slightly increasing (for single-QW's) according to temperature increments from 200 to 350 K [9], [21]. If we assume the carrier transport effect is dominant, we can calculate the carrier diffusion-capture time  $\tau_{bw}$ , which is also shown in Fig. 8(b). However, our data shows a decrease of  $\tau_{bw}$  with increasing temperature. This can be explained as follows. First, in simple view, the carrier diffusion-capture time  $\tau_{bw}$  is inversely proportional to the hole diffusion constant  $D = k_B T \mu / q$  where the mobility  $\mu$  is also temperature-dependent.  $k_B$  is the Boltzmann constant. Actually the mobility  $\mu$  decreases with increasing temperature. The total changes in diffusion constant  $D$  are determined by changes in  $\mu T$ . To be more exact, the carrier diffusion is usually referred to the diffusion capacitance of the test laser, which has a separate temperature dependence not limited to constant  $D$  in obvious ways [16]. Second, the transport effect may not play the only role in the roll-off frequency. The electrical parasitic effect can also account for the low-frequency roll-off. However, the external circuit parasitic will not change significantly with laser temperature. Thus, the capacitance of the test laser should respond to the increase of roll-off frequency. This trend indicates that the capacitance decreases with increasing temperature. This is reasonable since the charge storage capacitance decreases with decreasing carrier lifetime. Generally, because of this parasitic frequency, the roll-off frequency cannot be used to directly extract the exact value of carrier diffusion-capture time. Typical values for the well capture time are on the

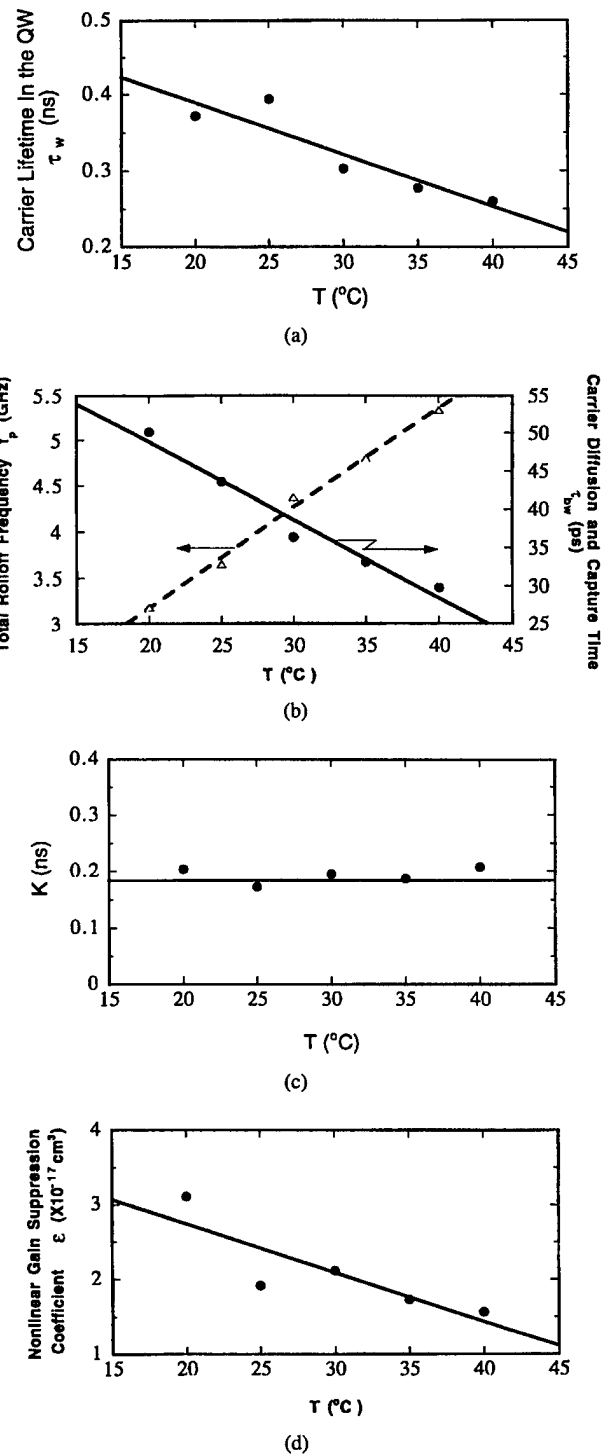


Fig. 8. (a) The carrier lifetime is plotted as a function of temperature, showing a large decrease as the temperature increases. (b) The roll-off frequency is plotted as a function of temperature, which increases with temperature. The carrier diffusion and capture time is also plotted in (b), which decreases with temperature. (c) The  $K$  factor is plotted as a function of temperature, which is insensitive to temperature. (d) The nonlinear gain suppression coefficient is plotted. The line in each figure shows the trend only.

order of tens of picoseconds [9], [14], [21]. Fig. 8(c) shows that the  $K$  factor is insensitive to temperature, which agrees with the previous literature [21]. The more QW's there are, the more independent of the  $K$  factor on temperature [21].

For single-QW lasers, the  $K$  factor can vary by two times between 200–350 K [4]. The temperature insensitivity of the  $K$  factor implies that the differential gain and the nonlinear gain suppression coefficient have a similar temperature dependence and cancel each other to maintain a temperature-insensitive  $\epsilon/(g'/\chi)$  ratio in InGaAsP-InP QW materials. This means the nonlinear gain suppression coefficients should decrease with increasing temperature. The nonlinear gain suppression coefficients of different temperatures are shown in Fig. 8(d), which are particularly sensitive to the extracted value of the damping factor and have large error variations. However, the decrease in nonlinear gain suppression coefficient with increasing temperature still can be seen. The nonlinear gain saturation results from a variety of factors, but it is considered to arise primarily through dynamic carrier heating [5], [6] and perhaps spectral hole burning [7]. If the  $K$  factor is constant, it means the maximum bandwidth  $f_{\max}$  is insensitive to the temperature. The lower temperature will not improve the potential bandwidth of QW lasers. Indeed, it gets worse because of the lower roll-off frequency. On the other hand, the injection efficiency and high threshold will deteriorate the optical signal at higher temperature. Therefore, designing a high-speed laser is a tradeoff among all aspects.

## V. CONCLUSIONS

The temperature dependence of the electrical and optical modulation responses have been investigated, and rate-equation theoretical models show excellent agreement with the data. The major difference between the two responses is the low-frequency roll-off, which is constant with respect to bias current at a given temperature. The carrier diffusion-capture-escape time influences the intrinsic modulation response of QW lasers through the transport factor  $\chi$ . We fit electrical and optical modulation responses at the same time at each current and each temperature. The combination of two measurements allows us to obtain a set of more accurate laser parameters. Temperature-dependent laser parameters are shown in this paper. When temperature increases, the most dominant effect is the linear degradation of differential gain, and reduction of injection efficiency and carrier lifetime in the QW's. The temperature-dependent response of all parameters closely follows physically reasonable trends.

## ACKNOWLEDGMENT

The authors would like to thank Dr. T. C. Wu for providing expert advice on the optical modulation experiments.

## REFERENCES

- [1] C. Y. Tsai, F. P. Shih, T. L. Sung, T. Y. Wu, C. H. Chen, and C. Y. Tsai, "A small-signal analysis of the modulation response of high-speed quantum-well lasers: Effects of spectral hole burning, carrier heating, and carrier diffusion-capture-escape," *IEEE J. Quantum Electron.*, vol. 33, pp. 2084–2096, 1997.
- [2] S. C. Kan, D. Vassilovski, T. C. Wu, and K. Y. Lau, "On effects of carrier diffusion and quantum capture in high speed modulation of quantum well lasers," *Appl. Phys. Lett.*, vol. 61, pp. 752–754, 1992.
- [3] D. Klotzkin, K. Kamath, and P. Bhattacharya, "Quantum capture times at room temperature in high-speed InGaAs-GaAs self-organized quantum-dot lasers," *IEEE Photon. Technol. Lett.*, vol. 9, pp. 1301–1303, 1997.
- [4] R. Nagarajan, T. Fukushima, S. W. Corzine, and J. E. Bowers, "Effects of carrier transport on high-speed quantum well lasers," *Appl. Phys. Lett.*, vol. 59, pp. 1835–1837, 1991.
- [5] M. Grupen and K. Hess, "Severe gain suppression due to dynamic carrier heating in quantum well lasers," *Appl. Phys. Lett.*, vol. 70, pp. 808–810, 1997.
- [6] M. P. Kesler and E. P. Ippen, "Subpicosecond gain dynamics in GaAlAs laser diodes," *Appl. Phys. Lett.*, vol. 51, pp. 1765–1767, 1987.
- [7] Y. Matsui, H. Murai, S. Arahira, Y. Ogawa, and A. Suzuki, "Enhanced modulation bandwidth for strain-compensated InGaAlAs-InGaAsP MQW lasers," *IEEE J. Quantum Electron.*, vol. 34, pp. 1970–1978, 1998.
- [8] R. Olshansky, P. Hill, V. Lanzisera, and W. Powazink, "Frequency response of 1.3  $\mu\text{m}$  InGaAsP high speed semiconductor lasers," *IEEE J. Quantum Electron.*, vol. QE-23, pp. 1410–1418, 1987.
- [9] R. Nagarajan, M. Ishikawa, T. Fukushima, R. Geels, and J. Bowers, "High speed quantum well lasers and carrier transport effects," *IEEE J. Quantum Electron.*, vol. 28, pp. 1990–2008, 1992.
- [10] H. Lu, C. Blaauw, B. Benyon, G. P. Li, and T. Makino, "High-power and high-speed performance of 1.3- $\mu\text{m}$  strained MQW gain-coupled DFB lasers," *IEEE J. Select. Topics Quantum Electron.*, vol. 1, pp. 375–381, 1995.
- [11] C. B. Su, J. Eom, C. H. Lange, C. B. Kim, R. B. Lauer, W. C. Rideout, and J. S. LaCourse, "Characterization of the dynamics of semiconductor lasers using optical modulation," *IEEE J. Quantum Electron.*, vol. 28, pp. 118–127, 1992.
- [12] K. J. Vahala and M. A. Newkirk, "Parasitic-free modulation of semiconductor lasers," *IEEE J. Quantum Electron.*, vol. 25, pp. 1393–1398, 1989.
- [13] R. F. Nabiev, E. C. Vail, and C. J. Chang-Hasnain, "Temperature dependent efficiency and modulation characteristics of Al-free 980-nm laser diodes," *IEEE J. Select. Topics Quantum Electron.*, vol. 1, pp. 234–243, 1995.
- [14] N. Tessler, M. Margalit, R. Ben Michael, M. Orenstein, and G. Eisenstein, "Modulation of quantum well lasers by short optical excitation: Energy and spatial dependent effects," *IEEE Photon. Technol. Lett.*, vol. 7, pp. 23–25, 1995.
- [15] D. Vassilovski, T. C. Wu, S. Kan, K. Y. Lau, and C. E. Zah, "Unambiguous determination of quantum capture, carrier diffusion, and intrinsic effect in quantum-well laser dynamics using wavelength-selective optical modulation," *IEEE Photon. Technol. Lett.*, vol. 7, pp. 706–708, 1995.
- [16] M. Grupen and K. Hess, "Simulation of carrier dynamics in quantum well lasers," *Proc. SPIE*, vol. 2693, pp. 374–385, 1996.
- [17] M. Grupen and K. Hess, "Simulation of carrier transport and nonlinearities in quantum-well laser diodes," *IEEE J. Quantum Electron.*, vol. 34, pp. 120–140, 1998.
- [18] J. Minch, S. H. Park, T. Keating, and S. L. Chuang, "Theory and experiment of InGaAsP and InGaAlAs long-wavelength strained quantum-well lasers," *IEEE J. Quantum Electron.*, vol. 35, pp. 771–782, May 1999.
- [19] C. E. Zah, R. Bhat, B. N. Pathak, F. Favire, W. Lin, M. C. Wang, N. C. Andreadakis, D. M. Hwang, M. A. Koza, T. P. Lee, Z. Wang, D. Darby, D. Flanders, and J. J. Hsieh, "High-performance uncooled 1.3- $\mu\text{m}$  AlGaInAs/InP strained-layer quantum-well laser for subscriber loop applications," *IEEE J. Quantum Electron.*, vol. 30, pp. 511–523, 1994.
- [20] J. Shimizu, H. Yamada, S. Murata, A. Tomita, M. Kitamura, and A. Suzuki, "Optical-confinement-factor dependencies of the  $K$  factor, differential gain, and nonlinear gain coefficient for 1.55  $\mu\text{m}$  InGaAs/InGaAsP MQW and strained-MQW lasers," *IEEE Photon. Technol. Lett.*, vol. 3, pp. 773–776, 1991.
- [21] M. Ishikawa, R. Nagarajan, T. Fukushima, J. Wasserbauer, and J. Bowers, "Long wavelength high-speed semiconductor laser with carrier transport effects," *IEEE J. Quantum Electron.*, vol. 28, pp. 2230–2241, 1992.
- [22] S. Seki, K. Yokoyama, and P. Sotirelis, "Theoretical analysis of high-temperature characteristics of 1.3  $\mu\text{m}$  InP-based quantum-well lasers," *IEEE J. Select. Topics Quantum Electron.*, vol. 1, pp. 264–274, 1995.
- [23] S. Kakimoto and H. Watanabe, "Threshold current, differential gain, and relaxation resonance frequency of 1.55- $\mu\text{m}$  bulk and MQW DFB lasers diodes," *IEEE J. Quantum Electron.*, vol. 34, pp. 1231–1239, 1998.
- [24] W. Rideout, W. F. Sharfin, E. S. Koteles, M. O. Vassell, and B. Elman, "Well-barrier hole burning in quantum well lasers," *IEEE Photon. Technol. Lett.*, vol. 3, pp. 784–786, 1991.
- [25] S. J. Sweeney, A. F. Philips, A. R. Adams, E. P. O'Reilly, and P. J. A. Thijs, "The effect of temperature dependent processes on the performance of 1.5- $\mu\text{m}$  compressively strained InGaAs(P) MQW semiconductor diode lasers," *IEEE Photon. Technol. Lett.*, vol. 10, pp. 1076–1078, 1998.

- [26] W. Fang, M. Hattendorf, S. L. Chuang, J. Minch, and C. S. Chang, "Analysis of temperature sensitivity in semiconductor lasers using gain and spontaneous emission measurements," *Appl. Phys. Lett.*, vol. 70, pp. 796-798, 1997.
  - [27] L. F. Tiemeijer, P. J. A. Thijs, P. J. de Waard, J. J. M. Binsma, and T. V. Dogen, "Dependence of polarization, gain, linewidth enhancement factor, and  $K$  factor on the sign of strain of InGaAs/InP strained-layer multi-quantum well lasers," *Appl. Phys. Lett.*, vol. 58, pp. 2738-2740, 1991.
  - [28] A. Yariv, "Scaling laws and minimum threshold currents for quantum-confined semiconductor lasers," *Appl. Phys. Lett.*, vol. 53, pp. 1033-1035, 1988.
  - [29] A. Haug, "Theory of the temperature dependence of the threshold current of an InGaAsP laser," *IEEE J. Quantum Electron.*, vol. QE-21, pp. 716-718, 1985.
  - [30] H. Temkin, D. Coblentz, R. A. Logan, J. P. van der Ziel, T. Tanbun-Ek, R. D. Yadavish, and A. M. Sergent, "High temperature characteristics of InGaAsP/InP laser structures," *Appl. Phys. Lett.*, vol. 62, pp. 2402-2404, 1993.
  - [31] Y. Zou, J. S. Osinski, P. Grodzinski, P. D. Dapkus, W. C. Rideout, W. F. Sharfin, J. Schlafer, and F. D. Crawford, "Experimental study of Auger recombination, gain, and temperature sensitivity of 1.5  $\mu\text{m}$  compressively strained semiconductor lasers," *IEEE J. Quantum Electron.*, vol. 29, pp. 1565-1575, 1993.
  - [32] D. M. Byrne and B. A. Keating, "A laser diode model based on temperature dependent rate equations," *IEEE Photon. Technol. Lett.*, vol. 1, pp. 1076-1078, 1989.
- T. Keating**, photograph and biography not available at the time of publication.
- X. Jin**, photograph and biography not available at the time of publication.
- S. L. Chuang** (S'78-M'82-SM'88-F'97), for biography, see p. 969 of the June 1999 issue of this JOURNAL.
- K. Hess** (M'79-SM'83-F'85), photograph and biography not available at the time of publication.

# Dual-pump four-wave mixing in a double-mode distributed feedback laser

J. Minch\* and S. L. Chuang

University of Illinois at Urbana-Champaign, Department of Electrical and Computer Engineering,  
1406 West Green Street, Urbana, Illinois 61801

Received May 3, 1999; revised manuscript received September 20, 1999

We present a comprehensive theoretical model with experimental results on four-wave mixing in a distributed feedback laser with two pump modes. Here the twin lasing modes serve as pump waves for the four-wave mixing, which takes place within the laser cavity. We show what we believe are new experimental measurements of the two-pump four-wave mixing conversion efficiency spectrum and show that, to first order, there is no fundamental dependence of the conversion efficiency on pump separation. This result indicates significant improvement in the probe and conjugate wavelength separation and in the conversion efficiency. Our theoretical model agrees quite well with the measured data and predicts the key experimentally observed phenomena, including the relative invariance of the conversion efficiency on pump separation, and the strong enhancement of certain conjugate waves when the probe detuning is close to the pump separation. © 2000 Optical Society of America [S0740-3224(00)01101-2]

OCIS codes: 140.3490, 190.4380, 190.5970, 190.2620.

## 1. INTRODUCTION

Much of the recent research on four-wave mixing (FWM) has been driven by its potential as an all-optical wavelength conversion technique.<sup>1</sup> Many groups have published studies of FWM in semiconductor optical amplifiers (SOA's),<sup>2-4</sup> where an external pump wave and an external probe wave are injected into the amplifier. Also, other groups have studied FWM in single-mode distributed feedback (DFB) lasers,<sup>5-9</sup> where the lasing mode serves as the pump wave and an external probe is injected into the lasing cavity. One of the largest challenges facing the practical use of this technology has been the poor conversion efficiency for useful wavelength shifts. Only very recently has significant improvement been achieved, with the use of extremely long SOA's.<sup>4</sup>

A clever solution to improve the conversion efficiency for larger wavelength shifts was proposed several years ago<sup>10</sup> by introduction of a second pump wave with a detuning from the first pump wavelength. The dynamic grating formed by the beating of the first pump with the probe wave causes the second pump to scatter into a shifted conjugate wave. The extra wavelength shift gained in this approach is exactly the wavelength separation of the two pump waves. Subsequent reports, including experimental data<sup>11</sup> (although few points of data were offered) and theory,<sup>12,13</sup> indicated that the conversion efficiency is relatively independent of the pump wavelength separation, being indirectly affected only through the dispersion of the gain and of the refractive index. Since then, experiments have been carried out both with parallel pumps in optical fibers<sup>14</sup> and SOA's<sup>15-17</sup> and with orthogonal pumps.<sup>18-24</sup> The use of orthogonal pumps is particularly attractive, since it can lead to polarization-independent wavelength conversion and optical spectral inversion. However, only very recently have detailed experimental data been published demonstrating the rela-

tive independence of conversion efficiency on the pump wavelength separation.<sup>15-17,25</sup>

In this paper, for the first time to our knowledge, is presented a new experimental configuration that uses a DFB laser with two lasing modes that serve as dual pumps. In contrast to the previous studies, which require two external pump waves and an external probe signal to be injected into a SOA or optical fiber, the lasing modes of the DFB laser serve as the two pump waves, and only an external probe signal is needed. In Section 2 we describe a comprehensive theory for the two-pump FWMs which yields analytical formulas for the small detuning case. In Section 3 we present detailed data showing the spectral dependence of the conversion efficiency for each of the important conjugate waves and discuss some of the interesting physical effects. In Section 4 we offer a summary of our measurements and draw some brief conclusions.

## 2. THEORETICAL MODEL

In the physical model of the laser operation and the FWM, several simplifying assumptions are made.

First, a perturbative approach is taken in that it is assumed that the power of the probe and of all resulting conjugate waves is negligible compared with the power of each pump wave and that these negligible values can be ignored for the modeling of the pump waves.

Second, a mean-field approximation is employed in which the intensity of all the fields is assumed to have little spatial variation.<sup>6,7</sup> This is probably unrealistic, since the presence of two lasing modes almost certainly means that there is some spatial dependence involved. To include this spatial variation in the analysis of the laser would require a numerical model such as the transfer-matrix model,<sup>26</sup> which would become especially complicated with the correct treatment of two lasing modes.<sup>27</sup>

This simplification, while physically inaccurate, yields analytical solutions and gives simple explanations for most of the interesting phenomena observed in the data.

Third, dispersion in both the refractive index and the gain is ignored.

Fourth, the nonlinear gain suppression coefficient is included but is assumed to be constant. This allows for the inclusion of intersubband processes such as carrier heating and spectral hole burning, which are important for FWM at larger pump-probe detunings. While the frequency dependence of these processes is ignored in this treatment, the detunings studied in our experiments are small enough that this is a good approximation.

Figure 1 is a schematic diagram of the electric field lines relevant to this study of two-pump FWM. The total field can be written as

$$E(t, z) = \{E_A + E_B \exp(i\Delta t) + E_{AC} \exp(-i\Delta t) \\ + E_{BC} \exp(i2\Delta t) + E_1 \exp(-i\Omega t) \\ + E_2 \exp(i\Omega t) + E_{B1} \exp[i(\Delta - \Omega)t] \\ + E_{B2} \exp[i(\Delta + \Omega)t] + E_x \exp[-i(\Delta - \Omega)t] \\ + E_{Bx} \exp[i(2\Delta - \Omega)t]\} \exp(-i\omega_A t). \quad (1)$$

In this expression  $E_A$  and  $E_B$  are each lasing modes of the DFB laser that serve as pump waves.  $\omega_A$  represents the lasing angular frequency of mode A, and the frequency separation between the two pumps is given by  $\Delta$ . The external probe wave is represented by  $E_1$ , and its frequency separation from pump wave A is given by  $\Omega$ . Note that, throughout this paper, pump A is defined to be the closest one to the probe wave, so which mode is represented by A and B depends on the location of the probe wave. The pump waves' mixing with each other leads to the creation of conjugates  $E_{AC}$  and  $E_{BC}$ . The interaction of the probe with the two pump waves leads to the creation of the other conjugates.  $E_2$ ,  $E_{B1}$ , and  $E_{B2}$  are created mainly as a result of third-order processes. Terms due to higher order processes are, in general, left out inasmuch as they are small. The exception to this approximation are the fifth-order processes  $E_x$  and  $E_{Bx}$ , which have a resonant condition when  $\Delta = \Omega$ . They are included here to explain the experimentally observed conjugate waves in this regime.

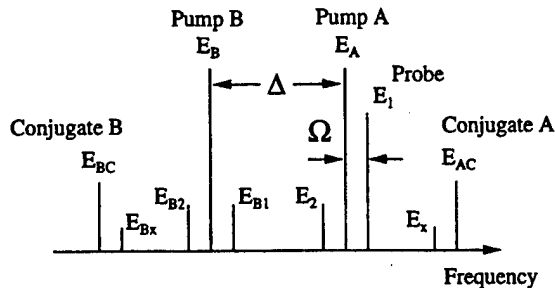


Fig. 1. Definitions of the optical electric fields in the frequency spectrum relevant to this study of two-pump FWM.  $E_A$  and  $E_B$  represent the lasing modes of the laser that serve as pump waves.  $E_1$  is the probe wave, and the other lines are conjugates created by the mixing of these fields.  $E_{AC}$  and  $E_{BC}$  are the conjugate waves created by the two pumps alone.

### A. Model for the Two Pump Modes

To model the lasing modes, we implement the following rate equations<sup>28</sup>:

$$\frac{dN}{dt} = \frac{I}{qV} - \frac{N}{\tau} - v_g a(N - N_0)[1 - \epsilon(S_A + S_B)] \\ \times (S_A + S_B), \quad (2)$$

$$\frac{dS_A}{dt} = \Gamma v_g a(N - N_0)[1 - \epsilon(S_A + S_B)]S_A \\ - \frac{S_A}{\tau_A} + \beta R_{sp}, \quad (3)$$

$$\frac{dS_B}{dt} = \Gamma v_g a(N - N_0)[1 - \epsilon(S_A + S_B)]S_B \\ - \frac{S_B}{\tau_B} + \beta R_{sp}, \quad (4)$$

where  $I$  is the injection current;  $q$  is the charge of an electron;  $V$  is the active-region volume;  $N$  is the carrier density;  $N_0$  is the transparency carrier density;  $\tau$  is the carrier lifetime;  $v_g$  is the group velocity;  $a$  is the differential gain;  $\Gamma$  is the optical confinement factor;  $\epsilon$  is the nonlinear gain suppression coefficient;  $\beta$  ( $\sim 1 \times 10^{-5}$ ) is the ratio of spontaneous emission photons that couple into the lasing modes;  $R_{sp}$  is the spontaneous emission rate;  $S_A$  and  $S_B$  are the density of photons in the lasing modes; and  $\tau_A$  and  $\tau_B$  are the photon lifetimes for each of the lasing modes A and B, respectively. In general, since the two lasing modes are at separate wavelengths, there would be different values of  $a$  and  $N_0$  for each mode. In DFB lasers the modal behavior is dominated by the relative values of the cavity loss (i.e., photon lifetime) for each mode. While the dispersion of the gain will have a minor effect on the strength of the modes, these effects are overwhelmed by the relative values of  $\tau_A$  and  $\tau_B$ . Therefore we make the simplifying assumption that  $a$  and  $N_0$  are constant.

In the steady state the left-hand side of these equations can be set to zero. It is relatively straightforward to solve for the photon densities of each mode as a function of the carrier density:

$$S_A = \tau_A \frac{y - \tau_B x}{\tau_A - \tau_B}, \quad (5)$$

$$S_B = \tau_B \frac{\tau_A x - y}{\tau_A - \tau_B}, \quad (6)$$

where

$$y = \frac{-b_1 \pm (b_1^2 - 4a_1c_1)^{1/2}}{2a_1}, \quad (7)$$

$$x = \Gamma c_1 + 2\beta R_{sp}, \quad (8)$$

$$a_1 = \epsilon v_g a(N_s - N_0), \quad (9)$$

$$b_1 = -v_g a(N_s - N_0), \quad (10)$$

$$c_1 = \frac{I}{qV} - \frac{N_s}{\tau}. \quad (11)$$

Rewriting Eq. (3) in terms of the carrier density gives

$$N_s = \frac{(S_A/\tau_{p1}) - \beta R_{sp}}{\Gamma v_g a [1 - \epsilon(S_A + S_B)] S_A} + N_0. \quad (12)$$

Using Eqs. (5)–(11) in Eq. (12) yields a single nonlinear equation for the carrier density. Given a value for the injection current, one may solve this equation numerically. Note that the sign in Eq. (7) should be chosen to yield a physically allowable solution; that is,  $S_A$  and  $S_B$  are positive.  $\beta R_{sp}$  is included so that the light power output below and above threshold operation can be modeled with the same rate equation.

### B. No Probe Case

When there is no probe wave present, FWM still exists owing to the presence of both lasing modes in the DFB cavity. To model the carrier density beating that is due to the lasing modes, it is necessary to rewrite Eq. (2) in terms of the electric field (the fields are assumed to be normalized so that their intensities are equal to the photon density).

$$\frac{dN}{dt} = \frac{I}{qV} - \frac{N}{\tau} - v_g a (N - N_0) [1 - \epsilon |E(t)|^2] |E(t)|^2. \quad (13)$$

Assuming that the carrier density has the form<sup>29</sup>

$$N(t) = N_s + \delta N_\Delta \exp(-i\Delta t) + \delta N_\Delta^* \exp(i\Delta t) \quad (14)$$

and using the rotating-wave approximation, we can straightforwardly solve for both the steady-state carrier density and the sinusoidally varying component<sup>29</sup>

$$N_s = \frac{\frac{I\tau}{qV} + v_g a \tau N_0 (1 - \epsilon |E_s|^2) |E_s|^2}{1 + v_g a \tau (1 - \epsilon |E_s|^2) |E_s|^2}, \quad (15)$$

$$\delta N_\Delta = \frac{v_g a \tau (N_s - N_0) (1 - 2\epsilon |E_s|^2) E_A E_B^*}{1 + v_g a \tau (1 - \epsilon |E_s|^2) |E_s|^2 - i\Delta \tau}, \quad (16)$$

where

$$|E_s|^2 = |E_A|^2 + |E_B|^2 = S_A + S_B. \quad (17)$$

To treat the electric fields, the wave equation

$$\nabla^2 E - \frac{n^2}{c^2} \frac{\partial^2 E}{\partial t^2} = \frac{1}{\epsilon_0 c^2} \frac{\partial^2 P}{\partial t^2} \quad (18)$$

is used with the electric fields and the polarizations broken into Fourier components as

$$E(x, y, z, t) = U(x, y) \sum_j E_j(z) \exp(-i\omega_j t), \quad (19)$$

$$P(x, y, z, t) = U(x, y) \sum_j P_j(z) \exp(-i\omega_j t). \quad (20)$$

Using Eqs. (19) and (20) in Eq. (18), multiplying by  $U^*(x, y)$ , and integrating over the  $x$  and  $y$  dimensions yields the one-dimensional wave equation<sup>29</sup>

$$\frac{d^2 E_j}{dz^2} + \frac{n^2 \omega_j^2}{c^2} E_j = -\frac{\Gamma \omega_j^2}{\epsilon_0 c^2} P_j. \quad (21)$$

The components of the polarization can be found from

$$P = \epsilon_0 \chi E, \quad (22)$$

where<sup>29</sup>

$$\chi = -\frac{nc}{\omega_0} v_g a (N - N_0) [\alpha + i(1 - \epsilon |E|^2)]. \quad (23)$$

These lead to the following components of the polarization:

$$P_{AC} = -\frac{\epsilon_0 n c a}{\omega_A} \{ \delta N_\Delta [\alpha + i(1 - \epsilon |E_s|^2)] - i\epsilon (N_s - N_0) E_A E_B^* \} E_A + (N_s - N_0) [\alpha + i(1 - \epsilon |E_s|^2)] E_{AC}, \quad (24)$$

$$P_{BC} = -\frac{\epsilon_0 n c a}{\omega_A} \{ \delta N_\Delta^* [\alpha + i(1 - \epsilon |E_s|^2)] - i\epsilon (N_s - N_0) E_A^* E_B \} E_B + (N_s - N_0) [\alpha + i(1 - \epsilon |E_s|^2)] E_{BC}. \quad (25)$$

In the case of no probe wave the components of the electric field are given by

$$E_j = A_j \exp(ik_j z), \quad (26)$$

where  $k_j = n\omega_j/c$ . By inserting these fields into the one-dimensional wave equation (21) and applying the slowly varying envelope approximation  $[(\partial^2 A_j)/\partial z^2 = 0]$ , we obtain the following coupled-mode equations:

$$\frac{\partial A_j}{\partial z} = \frac{i\omega_j \Gamma}{2n\epsilon_0 c} P_j \exp(-ik_j z). \quad (27)$$

In general, the coupled-mode equations are solved for the spatial variation of each of the pump, probe, and conjugate waves. Here we make the simplifying assumption that the waves behave as if they were in an optical amplifier. Under these conditions the spatial dependence for each pump wave is solved for. These solutions are then inserted into the coupled-mode rate equations for the conjugate. This leads to the following expressions for the conjugate waves:

$$E_{AC} = \frac{1}{2(1 - \epsilon |E_s|^2)} \times \left\{ \frac{v_g a \tau (1 - 2\epsilon |E_s|^2) [\alpha + i(1 - \epsilon |E_s|^2)]}{1 + v_g a \tau (1 - \epsilon |E_s|^2) |E_s|^2 - i\Delta \tau} + i\epsilon \right\} \times E_A^2 E_B^*, \quad (28)$$

$$E_{BC} = \frac{1}{2(1 - \epsilon |E_s|^2)} \times \left\{ \frac{v_g a \tau (1 - 2\epsilon |E_s|^2) [\alpha + i(1 - \epsilon |E_s|^2)]}{1 + v_g a \tau (1 - \epsilon |E_s|^2) |E_s|^2 + i\Delta \tau} + i\epsilon \right\} \times E_B^2 E_A^*. \quad (29)$$

### C. External Probe with a Detuning $\Omega \ll \Delta$

In the situation in which an injected probe wave with a pump-probe detuning  $\Omega$  is much smaller than the pump

separation  $\Delta$ , the conjugates  $E_2$ ,  $E_{B1}$ , and  $E_{B2}$  become significant. The carrier density in this case is expressed as<sup>29</sup>

$$N(t) = N_S + \delta N_\Omega \exp(-i\Omega t) + \delta N_\Omega^* \exp(i\Omega t). \quad (30)$$

The carrier beating due to the two pump waves has been neglected, since it has no interactions with the slower  $\exp(-i\Omega t)$  terms. If we insert Eq. (30) into Eq. (13) and use the rotating-wave approximation, the carrier beating term is given as<sup>29</sup>

$$\delta N_\Omega = -\frac{(N_S - N_0)(1 - 2\epsilon|E_s|^2)S_\Omega/P_s}{1 + (1 - \epsilon|E_s|^2)P_0 - i\Omega\tau}, \quad (31)$$

where  $P_s = 1/\nu_g a \tau$ ,  $P_0 = |E_s|^2/P_s$ , and

$$S_\Omega = E_1 E_A^* + E_A E_2^* + E_{B1} E_B^* + E_B E_{B2}^*. \quad (32)$$

The components of the polarization can be written as

$$P_A = -\frac{\epsilon_0 n c a}{\omega_A} (N_S - N_0) [\alpha + i(1 - \epsilon|E_s|^2)] E_A, \quad (33)$$

$$P_B = -\frac{\epsilon_0 n c a}{\omega_A} (N_S - N_0) [\alpha + i(1 - \epsilon|E_s|^2)] E_B, \quad (34)$$

$$P_1 = -\frac{\epsilon_0 n c a}{\omega_A} ((N_S - N_0) [\alpha + i(1 - \epsilon|E_s|^2)] E_1 + \{\delta N_\Omega [\alpha + i(1 - \epsilon|E_s|^2)] - i\epsilon(N_S - N_0) S_\Omega\} E_A), \quad (35)$$

$$P_2 = -\frac{\epsilon_0 n c a}{\omega_A} ((N_S - N_0) [\alpha + i(1 - \epsilon|E_s|^2)] E_2 + \{\delta N_\Omega^* [\alpha + i(1 - \epsilon|E_s|^2)] - i\epsilon(N_S - N_0) S_\Omega^*\} E_A), \quad (36)$$

$$P_{B1} = -\frac{\epsilon_0 n c a}{\omega_A} ((N_S - N_0) [\alpha + i(1 - \epsilon|E_s|^2)] E_{B1} + \{\delta N_\Omega [\alpha + i(1 - \epsilon|E_s|^2)] - i\epsilon(N_S - N_0) S_\Omega\} E_B), \quad (37)$$

$$P_{B2} = -\frac{\epsilon_0 n c a}{\omega_A} ((N_S - N_0) [\alpha + i(1 - \epsilon|E_s|^2)] E_{B2} + \{\delta N_\Omega^* [\alpha + i(1 - \epsilon|E_s|^2)] - i\epsilon(N_S - N_0) S_\Omega^*\} E_B). \quad (38)$$

Since  $\Omega$  is small, the probes and the conjugates are assumed to have the same spatial dependence as the pump wave.<sup>30</sup> Thus the fields can be expressed as  $E_A$ ,  $E_1$ , and  $E_2$ , equivalent to  $A_j \exp(ik_A z)$ , and  $E_B$ ,  $E_{B1}$ , and  $E_{B2}$ , equivalent to  $A_j \exp(ik_B z)$ . Using these fields in the one-dimensional wave equation (21) and assuming that the first and the second derivatives of the field amplitudes ( $A_j$ ) vanish with respect to  $z$  in the leading-order approximation, we obtain

$$-k_{A,B}^2 E_{A,B} + \frac{n^2 \omega_{A,B}^2}{c^2} E_{A,B} = -\frac{\omega_{A,B}^2 \Gamma}{\epsilon_0 c^2} P_{A,B} \quad (39)$$

for the pump waves. Similarly, for the probe and the conjugate waves, but using Eq. (39) to eliminate  $k_A$  and  $k_B$ , we obtain

$$\Omega E_{1,B1} = \frac{\omega_A \Gamma}{2n^2} \left\{ \frac{n c a}{\omega_A} (N_S - N_0) [\alpha + i(1 - \epsilon|E_s|^2)] \times E_{1,B1} - \frac{P_{1,B1}}{\epsilon_0} \right\} + \kappa_{1,B1} E_i, \quad (40)$$

$$-\Omega E_{2,B2} = \frac{\omega_A \Gamma}{2n^2} \left\{ \frac{n c a}{\omega_A} (N_S - N_0) \times [\alpha + i(1 - \epsilon|E_s|^2)] E_{2,B2} - \frac{P_{2,B2}}{\epsilon_0} \right\}, \quad (41)$$

where  $E_i$  is the incident probe wave,  $\kappa_1$  is a coupling coefficient, and  $\kappa_{B1}$  is 0 in the equation for  $E_{B1}$ .

Using the rotating-wave approximation, we obtain from Eqs. (39)–(41) the following matrix equation:

$$\vec{M} \begin{bmatrix} E_1 \\ E_2^* \\ E_{B1} \\ E_{B2}^* \end{bmatrix} = \begin{bmatrix} \kappa E_i \\ 0 \\ 0 \\ 0 \end{bmatrix}, \quad (42)$$

where the matrix elements are given as

$$M_{11} = \Omega - K \left( -\frac{B}{P_s A} - i\epsilon \right) |E_A|^2,$$

$$M_{12} = -K \left( -\frac{B}{P_s A} - i\epsilon \right) E_A^2,$$

$$M_{13} = -K \left( -\frac{B}{P_s A} - i\epsilon \right) E_B^* E_A,$$

$$M_{14} = -K \left( -\frac{B}{P_s A} - i\epsilon \right) E_B E_A,$$

$$M_{21} = -K \left( -\frac{B^*}{P_s A} + i\epsilon \right) E_A^{*2},$$

$$M_{22} = -\Omega - K \left( -\frac{B^*}{P_s A} + i\epsilon \right) |E_A|^2,$$

$$M_{23} = -K \left( -\frac{B^*}{P_s A} + i\epsilon \right) E_A^* E_B^*,$$

$$M_{24} = -K \left( -\frac{B^*}{P_s A} + i\epsilon \right) E_A^* E_B,$$

$$M_{31} = -K \left( -\frac{B}{P_s A} - i\epsilon \right) E_A^* E_B,$$

$$M_{32} = -K \left( -\frac{B}{P_s A} - i\epsilon \right) E_A E_B,$$

$$M_{33} = \Omega - K \left( -\frac{B}{P_s A} - i\epsilon \right) |E_B|^2,$$



$$\begin{aligned}
M_{34} &= -K \left( -\frac{B}{P_s A} - i\epsilon \right) E_B^2, \\
M_{41} &= -K \left( -\frac{B^*}{P_s A} + i\epsilon \right) E_A^* E_B^*, \\
M_{42} &= -K \left( -\frac{B^*}{P_s A} + i\epsilon \right) E_A E_B^*, \\
M_{43} &= -K \left( -\frac{B^*}{P_s A} + i\epsilon \right) E_B^{*2}, \\
M_{44} &= -\Omega - K \left( -\frac{B^*}{P_s A} + i\epsilon \right) |E_B|^2, \quad (43)
\end{aligned}$$

where

$$\begin{aligned}
A &= 1 + (1 - \epsilon |E_s|^2) P_0 - i\Omega\tau, \\
B &= [\alpha + i(1 - \epsilon |E_s|^2)](1 - 2\epsilon |E_s|^2), \\
K &= \frac{\Gamma c a (N_s - N_0)}{2n}. \quad (44)
\end{aligned}$$

Solving this system, we obtain

$$\frac{E_2^*}{\kappa E_i} = (\bar{M}^{-1})_{21} = \frac{E_A^{*2} U}{D}, \quad (45)$$

$$\frac{E_{B1}}{\kappa E_i} = (\bar{M}^{-1})_{31} = \frac{E_A^* E_B U^*}{D}, \quad (46)$$

$$\frac{E_{B2}^*}{\kappa E_i} = (\bar{M}^{-1})_{41} = \frac{E_A^* E_B^* U}{D}, \quad (47)$$

where

$$\begin{aligned}
U &= \frac{\Gamma c a (N_s - N_0)}{2n P_s} \{ -[\alpha + i(1 - \epsilon |E_s|^2)] \\
&\quad \times (1 - 2\epsilon |E_s|^2) + i\epsilon P_s (1 + P_0 - i\Omega\tau) \}, \quad (48)
\end{aligned}$$

$$\begin{aligned}
D &= \Omega(-\Omega(1 + P_0) - i(\Omega_R^2 - \Omega^2)\tau + \epsilon\{\Omega P_s P_0^2 \\
&\quad - i\Omega_R^2 \tau [P_s(1 + P_0 - i\Omega\tau) - 2P_s P_0]\}), \quad (49)
\end{aligned}$$

$$\Omega_R^2 = \frac{P_0}{\tau \Gamma v_g a (N_s - N_0)}. \quad (50)$$

Note that Eq. (45) reduces to the equivalent of Eq. (67) of Ref. 6 in the limit of no second pump ( $|E_B|^2 = 0$ ) and no nonlinear gain ( $\epsilon = 0$ ). Also, this formulation is equivalent to a formulation in which the van der Pol equation is used as in Ref. 7 for the single-pump case. In the case of two pumps a second van der Pol equation describing the evolution of the waves near the second pump would be used. Insofar as the definition of  $E_i$  in Ref. 7 differs from ours by a factor of  $i$ , in the limit of no second pump ( $|E_B|^2 = 0$ ) our matrix  $\bar{M}$  [in Eqs. (42)–(44)] reduces to a  $2 \times 2$  matrix that can be shown to be identical to Eqs. (11)–(14) of Ref. 7.

Finally, it is interesting that Eqs. (42)–(44) contain no dependence on the pump separation ( $\Delta$ ). With dispersion effects neglected, this indicates that the conversion effi-

ciency for the shifted conjugates  $E_{B1}$  and  $E_{B2}$  should be the same as that for  $E_2$  no matter what the pump separation is. In practice, the conversion range is limited by the window of appreciable net gain for the semiconductor material.

#### D. Resonance Case when the Probe–Pump Detuning $\Omega \approx \Delta$

If the injected probe wave has a larger pump–probe detuning such that it is of the order of the pump spacing, we can no longer neglect the carrier density beating that is due to the two pumps [the  $\exp(-i\Delta t)$  term]. In this case we express the carrier density as

$$\begin{aligned}
N(t) &= N_s + \delta N_\Delta \exp(-i\Delta t) \\
&\quad + \delta N_\Delta^* \exp(i\Delta t) + \delta N_\Omega \exp(-i\Omega t) \\
&\quad + \delta N_\Omega^* \exp(i\Omega t) + \delta N_x \exp[-i(\Delta - \Omega)t] \\
&\quad + \delta N_x^* \exp[i(\Delta - \Omega)t], \quad (51)
\end{aligned}$$

where  $\delta N_x$  represents the carrier density beating that is due to the mixing of the  $\delta N_\Omega$  and the  $\delta N_\Delta$  terms. Inserting Eq. (51) into Eq. (13) gives the following system of equations:

$$\bar{P} \begin{bmatrix} \delta N_\Omega \\ \delta N_x^* \end{bmatrix} = \begin{bmatrix} Q_1 \\ Q_2 \end{bmatrix}, \quad (52)$$

where

$$\begin{aligned}
P_{11} &= i\Omega\tau - 1 - (1 - \epsilon |E_s|^2) P_0, \\
P_{12} &= -\frac{1}{P_s} (1 - 2\epsilon |E_s|^2) E_A E_B^*, \\
P_{21} &= -\frac{1}{P_s} (1 - 2\epsilon |E_s|^2) E_A^* E_B, \\
P_{22} &= -i(\Delta - \Omega)\tau - 1 - (1 - \epsilon |E_s|^2) P_0, \\
Q_1 &= \frac{1}{P_s} (N_s - N_0) (1 - 2\epsilon |E_s|^2) E_A^* E_1, \\
Q_2 &= \frac{1}{P_s} [\delta N_\Delta^* (1 - 2\epsilon |E_s|^2) \\
&\quad - 2\epsilon (N_s - N_0) E_A^* E_B] E_A^* E_1. \quad (53)
\end{aligned}$$

These equations yield solutions of

$$\begin{bmatrix} \delta N_\Omega \\ \delta N_x^* \end{bmatrix} = \frac{1}{P_{11}P_{22} - P_{12}P_{21}} \begin{bmatrix} P_{22} & -P_{12} \\ -P_{21} & P_{11} \end{bmatrix} \begin{bmatrix} Q_1 \\ Q_2 \end{bmatrix}. \quad (54)$$

When  $\Delta - \Omega$  becomes small there is a large resonance in the  $\delta N_x$  terms. This beating causes each pump to scatter into the conjugates detuned at this frequency. As a result,  $E_2$  and  $E_{B1}$  experience a large enhancement, and two new conjugates,  $E_x$  and  $E_{Bx}$ , become observable. Relationships for the electric fields can be written, resulting in a large set of linear equations. We leave this analysis out because it becomes very difficult to track and because it yields little insight into the physics of the system. However, we do summarize here the field dependencies of the resulting conjugates from this fifth-order process:

$$\begin{aligned}
E_x &= \chi_x^{(5)} E_B |E_A|^2 E_A^* E_1, \\
E_{B1} &= \chi_{B1}^{(5)} E_B^* E_A^3 E_1^*, \\
E_2 &= \chi_2^{(5)} E_B^2 E_A^* E_1, \\
E_{Bx} &= \chi_{Bx}^{(5)} |E_B|^2 E_A^2 E_1^*.
\end{aligned} \quad (56)$$

### 3. EXPERIMENTS

For our experiments, we use an index-coupled DFB laser with two lasing modes as the mixing device. Another DFB laser similar to the mixing laser, but with a single mode, is used to provide the probe signal. The probe signal is coupled into a fiber and is passed through an optical isolator to eliminate injection of light from the mixing DFB laser into the probe DFB laser. The probe light is then passed through a 20-dB fiber coupler to permit monitoring of the power of the probe signal injected into the mixing DFB laser. Light emitted from the other facet of the mixing DFB laser is coupled into another fiber and is monitored with a Hewlett-Packard optical spectrum analyzer to yield the output powers of the pump, probe, and conjugate signals. The operating temperatures of both probe and mixing DFB lasers are maintained by means of thermoelectric controllers, with the mixing DFB laser being kept at 25 °C for all the experiments. Tuning of the probe signal is accomplished by changing of the operating bias current and of the temperature of the probe DFB laser. A larger tuning range is achieved by use of several different probe DFB lasers.

### 4. RESULTS AND DISCUSSION

Figure 2 shows a typical spectrum from the antireflection facet of the two-mode DFB laser at a bias current of  $I = 90$  mA. Again,  $E_A$  and  $E_B$  are the two lasing modes, and  $E_{AC}$  and  $E_{BC}$  are conjugates caused by the mixing of the lasing modes. Curves showing light output power versus bias current for both the lasing modes and the conjugates are shown by means of symbols in Fig. 3(a). The power shown corresponds to the peak power of each mode measured. The dashed curves represent a fit of the photon density in each mode, obtained from Eqs. (5)–(12), (28), and (29), with the parameters listed in Table 1. The relationship between the photon densities  $S$  of each mode and the measured peak power  $P_{\text{meas}}$  can be expressed as

$$P_{\text{meas}} = K_1 h \nu_g A S, \quad (57)$$

where  $K_1$  is a coupling constant,  $h \nu$  is the photon energy ( $\sim 0.8$  eV),  $\nu_g$  is the group velocity,  $A$  is the cross-sectional area of the waveguide ( $\sim 1 \mu\text{m} \times 0.25 \mu\text{m}$ ), and  $S$  is the photon density. Our fit yields a value of  $\sim 0.44$  for  $K_1$ , which is quite reasonable. Figure 3(b) shows the measured conjugate powers versus the following power laws, which they should obey:

$$\begin{aligned}
S_{AC} &\propto S_A^2 S_B, \\
S_{BC} &\propto S_A S_B^2.
\end{aligned} \quad (58)$$

The slope of 1 on the log-log plot indicates that the conjugates do indeed obey these relationships.

Figure 4 shows typical spectra of the FWM that results when a probe wave is injected at a pump-probe detuning that is much smaller than the pump spacing. These spectra are for three different probe detunings. Also, it should be noted that these spectra are taken from the highly reflecting facet of the mixing DFB laser. The mixing of the probe wave with the first pump creates three main conjugate waves. Here one of the advantages of using two pumps for FWM is very clear. Each of the conjugate waves is approximately the same power, even though  $E_{B2}$  is shifted by an extra 2 nm (the separation of the two pump waves) relative to  $E_2$ , which is the resulting conjugate if just  $E_A$  were present.

This result can be seen more explicitly in Fig. 5, where the conversion efficiency, defined as the ratio of the output conjugate power to the input probe power, is plotted

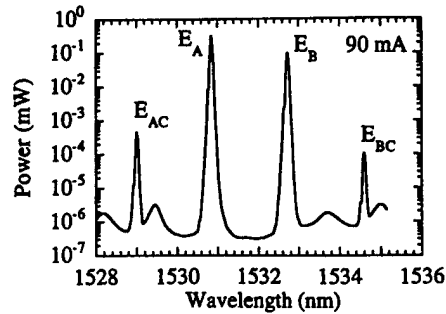


Fig. 2. Typical lasing power spectrum of the mixing two-mode DFB laser.  $E_A$  and  $E_B$  are the two lasing modes, and  $E_{AC}$  and  $E_{BC}$  are the conjugates created by the mixing of these modes.

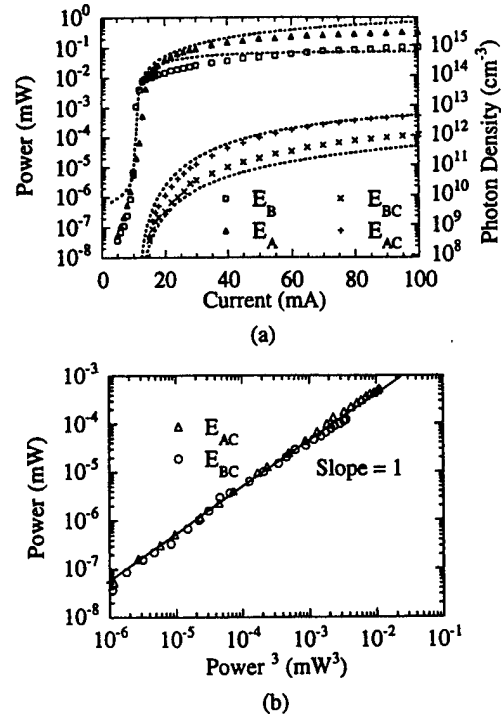


Fig. 3. (a) Light output power versus the bias current (symbols), for the two lasing modes as well as the created conjugates shown in Fig. 2. The dashed curves represent theoretical fits of the photon density in each mode. (b) Power of each conjugate wave plotted versus the proper power dependence on the lasing field powers as described in the text [Eqs. (58)].

**Table 1. Parameters Used in the Theoretical Calculations**

Parameter	Symbol (Unit)	Value
Electron charge	$q$ (C)	$1.602 \times 10^{-19}$
Active-region volume	$V$ (cm <sup>3</sup> )	$1 \times 10^{-11}$
Carrier lifetime	$\tau$ (s)	$0.8 \times 10^{-9}$
Group velocity	$v_g$ (cm s <sup>-1</sup> )	$8.33 \times 10^9$
Differential gain	$a$ (cm <sup>2</sup> )	$2 \times 10^{-16}$
Transparency carrier density	$N_0$ (cm <sup>-3</sup> )	$1 \times 10^{18}$
Nonlinear gain coefficient	$\epsilon$ (cm <sup>3</sup> )	$7 \times 10^{-17}$
Optical confinement factor	$\Gamma$	0.1
Photon lifetime	$\tau_{p1}$ (s)	$1.33333 \times 10^{-12}$
	$\tau_{p2}$ (s)	$1.33332 \times 10^{-12}$
Linewidth enhancement factor	$\alpha$	5
Spontaneous emission	$\beta R_{sp}$ (cm <sup>-3</sup> s <sup>-1</sup> )	2800

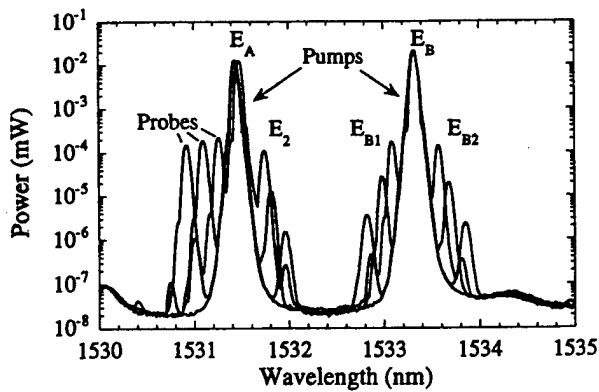


Fig. 4. Typical FWM power spectra for the case of an injected probe wave with a small detuning on the left-hand side of pump  $E_A$ . For each probe detuning shown, three conjugate waves  $E_2$ ,  $E_{B1}$ , and  $E_{B2}$  are produced.

as symbols for each of the conjugates. The wavelength in this plot corresponds to the wavelength of the probe wave. Also, it should be noted that the definitions of each conjugate depend on the location of the probe wave; the pump closest to the probe wave is always considered to be  $E_A$ . We can see that there is only a small variation among these three conjugates, especially at small pump-probe detunings. These variations can be accounted for by differences in the gain and cavity enhancement experienced by each of the conjugates.

The curves in Fig. 5 correspond to the theoretical results that we obtained by using the absolute magnitude squared of Eqs. (45) and (47). The solid curves represent the conversion efficiency of  $E_2$ , and the dashed curve represents the conversion efficiency of the shifted conjugates. Differences in the two theoretical curves are due to the difference in power of the two pump waves. The parameters for this fit are again those listed in Table 1. Note that the theoretical conversion efficiency spectra do not take into account either dispersion of the gain and of the refractive index or the spatial dependence of the two pump waves. These effects could account for the fact that the theory predicts a larger difference than is mea-

sured between the conjugates in the cases in which the probe wave is near one of the pumps. The theory also ignores the presence of the DFB grating as well as the end facets, leaving out the detailed effects of the cavity on the conversion efficiency spectrum. This is why the theory does not predict much of the behavior for the case in which the probe is away from the pump wavelengths.

To demonstrate more clearly the relative independence of the conversion efficiency on pump separation, we repeated the experiments for a similar DFB laser with two lasing modes  $\sim 6$  nm apart. Figure 6 shows the conversion efficiency for the three conjugates (denoted by symbols) as well as the amplified spontaneous emission or the lasing spectrum (denoted by the solid curve). Again, there is a relatively small difference between the conversion efficiency of  $E_2$  and the shifted conjugate  $E_{B2}$ , even though the extra shift is 6 nm ( $\sim 750$  GHz). In Fig. 7 we show the conversion efficiency of  $E_{B2}$  relative to that of the conjugate in an experiment conducted with a similar DFB laser, but with a single lasing mode (single pump wave).<sup>9</sup> The  $x$  axis represents the pump-probe detuning frequency for the single-pump case, and, for the two-pump result, zero detuning represents halfway between the two modes. This was done so that the two cases

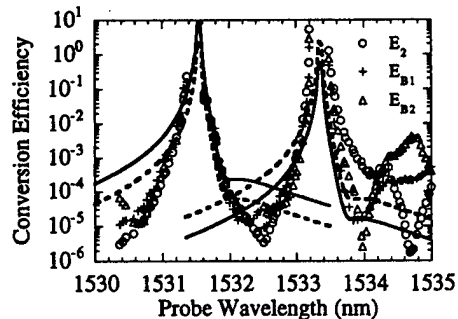


Fig. 5. Conversion efficiency (symbols) for each of the generated conjugate waves, plotted versus the probe wavelength. The curves are theoretical fits of the conversion efficiency, with the solid curves representing  $E_2$  and the dashed curves representing the shifted conjugates ( $E_{B1}$  and  $E_{B2}$ ). There is relatively little difference in conversion efficiency for the first conjugate and the shifted conjugates.

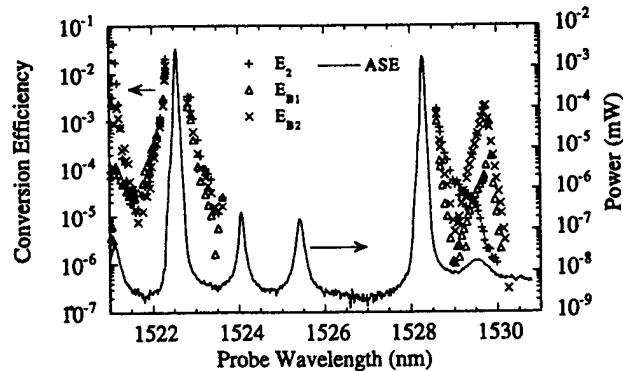


Fig. 6. Conversion efficiency (symbols) for the conjugate waves in another DFB laser with two pump wavelengths  $\sim 6$  nm apart. The solid curve represents the laser power spectrum or the amplified spontaneous emission spectrum without the injected probe wave. Again, there is relatively little difference in conversion efficiency for the first conjugate and the shifted conjugates.

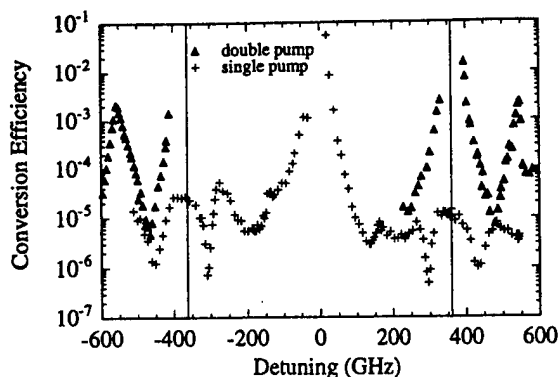


Fig. 7. Comparison of the conversion efficiency for two-pump FWM and single-pump FWM<sup>9</sup> in DFB lasers. The conversion efficiency is shown versus the probe detuning for the single-pump case. For the two-pump case, zero detuning is chosen to be midway between the pump waves so that a comparison can be made on the basis of the same overall frequency shift. For small enough probe detunings, the two-pump case gives conversion efficiencies between 100 and 1000 times larger.

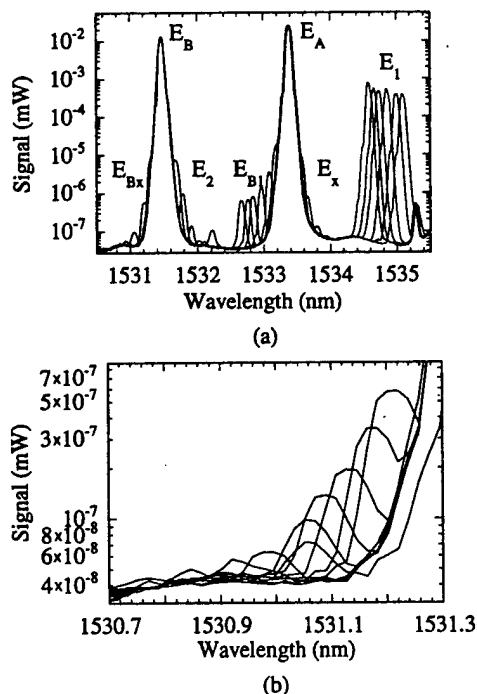


Fig. 8. (a) Typical FWM power spectra for the case in which the probe detuning is close to the probe separation. In this case conjugates  $E_2$  and  $E_{B1}$  experience a large enhancement, while new conjugates  $E_x$  and  $E_{Bx}$  are also created. (b) Close-up of newly created conjugate  $E_{Bx}$ .

could be compared on the basis of the same frequency shift. The two-pump case can give a 100–1000 $\times$  increase in conversion efficiency if the probe is close enough to one of the pump waves. Note that there could be a difference in coupling coefficients between the two cases, which would change the relative values of these two conversion efficiency curves; however, we estimate that this should account for no more than a factor of 5 between the two curves. Also, the difference in pump power between the two cases needs to be considered in this comparison. The exact values of the pump powers are difficult to obtain be-

cause of the unknown coupling coefficients. The total, maximized lasing power from each laser, collected from the side in which the probe wave was injected, was  $\sim 1$  mW for each laser. For the two-pump case, however, this power is split between two modes, which makes the conversion efficiency lower than if the same pump powers were used.

When the probe detuning becomes comparable with the spacing between the pump waves, some interesting phenomena occur. Figure 8(a) shows the resulting spectra for several probe detunings close to the pump separation frequency. Two of the conjugates ( $E_2$  and  $E_{B1}$ ) become strongly enhanced in this figure. Also, two new conjugates appear ( $E_x$  and  $E_{Bx}$ ) and become as strong as the others. A close-up view of the newly created  $E_{Bx}$  is shown in Fig. 8(b).

The conversion efficiencies of each of these conjugates are plotted in Fig. 9. Again, the  $x$  axis represents the position of the probe wave. The point at which the pump-probe detuning is equivalent to the pump separation is  $\sim 1535.3$  nm. As the probe wave approaches this location each of the conjugates experiences a large enhancement. When the probe wave is away from this location,  $E_x$  and  $E_{Bx}$  disappear, while  $E_2$  and  $E_{B1}$  are still observed. As pointed out in section 2, this happens because  $E_x$  and  $E_{Bx}$  are created by a fifth-order process, while  $E_2$  and  $E_{B1}$  have contributions from both the third-order FWM processes and this resonant fifth-order process. Where the fifth-order process no longer dominates, there are still contributions to these conjugates.

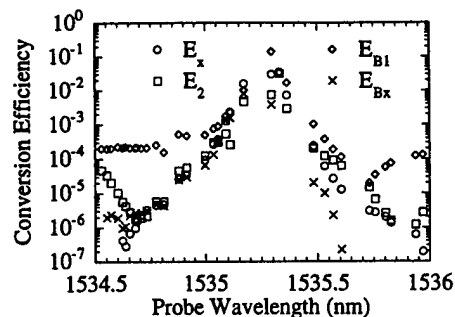


Fig. 9. Conversion efficiencies for the four conjugates that experience a large resonance when the probe detuning is near the pump separation.

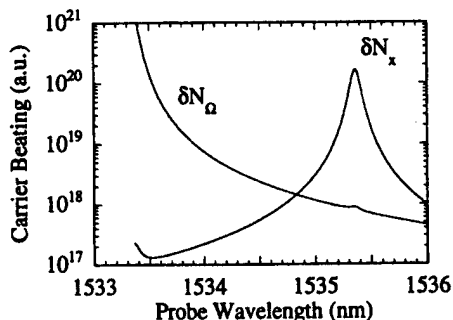


Fig. 10. Normalized magnitude of the carrier beating terms important in the creation of the observed conjugates. The  $x$  axis corresponds to the position of the injected probe wave. When the probe detuning is near the pump separation frequency the large resonance in  $\delta N_x$  causes the observed enhancement of the conjugates shown in Figs. 8 and 9.

Figure 10 shows a plot of the relative strengths of the carrier beating processes  $\delta N_\Omega$  and  $\delta N_x$ , from Eq. (55), normalized to the power of the probe wave. For probe wavelengths that give small pump-probe detunings,  $\delta N_\Omega$  is large and causes the large enhancement in the conversion efficiency seen for this regime, as discussed above. As the detuning becomes larger,  $\delta N_\Omega$  drops off rapidly. However, as the detuning becomes closer to the pump separation,  $\delta N_x$  has a large resonance, which leads to the large enhancement of each of the conjugates shown in Figs. 8 and 9.

## 5. SUMMARY AND CONCLUSIONS

We have presented what is for the first time, to the best of our knowledge, a comprehensive study of the properties of four-wave mixing (FWM) in a distributed feedback (DFB) laser with two lasing modes. We show detailed experimental measurements of the two-pump FWM conversion efficiency spectrum and show that, to first order, there is no fundamental dependence of the conversion efficiency on pump separation. Any dependence comes from smaller effects such as cavity effects and dispersion of the gain and of the refractive index. We have also presented a comprehensive model for the lasing modes and the FWM based on a mean-field approximation. This model agrees quite well with the measured data, showing no dependence on pump separation for the two-pump FWM conversion efficiency. Also, it explains how the carrier density beating induced by the pump-pump beating and the pump-probe beating can interact and lead to a new resonant enhancement of some conjugate waves, as observed in the experimental data for probe detunings of the order of the pump separation.

The practicality of using two-mode DFB lasers for wavelength conversion is severely limited by the difficulty in building such a device, especially with a tunable separation between the lasing modes. Little work has been done in this area.<sup>31</sup> In practice, one can use either a single-mode DFB laser with one external pump, which provides a tunable detuning, or two external pump lasers injected into a SOA, as was done in many of the studies cited in our reference list. The analytical results obtained from our theory can be applied to these cases, since a mean-field approach (which leaves out the details of the laser cavity) has been used.

## ACKNOWLEDGMENTS

The authors thank C. S. Chang for helpful discussions and insights over the course of this work. This research was supported by Office of Naval Research grant N0014-96-1-0902.

\*Present address, MIT Lincoln Laboratory, 224 Wood Street, Lexington, Massachusetts 02420.

## REFERENCES

1. S. J. B. Yoo, "Wavelength conversion technologies for WDM network applications," *J. Lightwave Technol.* **14**, 955-966 (1996).
2. T. Mukai and T. Saitoh, "Detuning characteristics and conversion efficiency of nearly degenerate four-wave mixing in a 1.5- $\mu\text{m}$  traveling-wave semiconductor laser amplifier," *IEEE J. Quantum Electron.* **26**, 865-875 (1990).
3. J. Zhou, N. Park, K. Vahala, M. Newkirk, and B. Miller, "Four-wave mixing wavelength conversion efficiency in semiconductor traveling-wave amplifiers measured to 65 nm of wavelength shift," *IEEE Photon. Technol. Lett.* **6**, 984-987 (1994).
4. F. Girardin, J. Eckner, G. Guekos, R. Dall'Ara, A. Mecozzi, A. D'Ottavi, F. Martelli, S. Scotti, and P. Spano, "Low-noise and very high-efficiency four-wave mixing in 1.5-mm-long semiconductor optical amplifiers," *IEEE Photon. Technol. Lett.* **9**, 746-748 (1997).
5. S. Murata, A. Tomita, J. Shimizu, H. Kitamura, and A. Suzuki, "Observation of highly non-degenerate four-wave mixing (>1 THz) in an InGaAsP multiple quantum well laser," *Appl. Phys. Lett.* **58**, 1458-1460 (1991).
6. A. Mecozzi, A. D'Ottavi, and R. Hui, "Nearly degenerate four-wave mixing in distributed feedback semiconductor lasers operating above threshold," *IEEE J. Quantum Electron.* **29**, 1477-1487 (1993).
7. R. Hui, S. Benedetto, and I. Montrosset, "Optical frequency conversion using nearly degenerate four-wave mixing in a distributed-feedback semiconductor laser: theory and experiment," *J. Lightwave Technol.* **11**, 2026-2031 (1993).
8. H. Kuwatsuka, H. Shoji, M. Matsuda, and H. Ishikawa, "THz frequency conversion using nondegenerate four-wave mixing process in a lasing long-cavity  $\lambda/4$ -shifted DFB laser," *Electron. Lett.* **31**, 2108-2110 (1995).
9. J. Minch, C. S. Chang, and S. L. Chuang, "Wavelength conversion in distributed-feedback lasers," *IEEE J. Sel. Top. Quantum Electron.* **2**, 569-576 (1997).
10. G. Grosskopf, R. Ludwig, and H. G. Weber, "140 Mbit/s DPSK transmission using an all-optical frequency converter with a 4000 GHz conversion range," *Electron. Lett.* **24**, 1106-1107 (1988).
11. G. Grosskopf, L. Kuller, R. Ludwig, R. Schnabel, and H. G. Weber, "Semiconductor laser optical amplifiers in switching and distribution networks," *Opt. Quantum Electron.* **21**, S59-S79 (1989).
12. N. Schunk, G. Grosskopf, R. Ludwig, R. Schnabel, and H. G. Weber, "Frequency conversion by nearly-degenerate four-wave mixing in traveling-wave semiconductor laser amplifiers," *IEEE Proc. Optoelectron.* **137**, 209-214 (1990).
13. N. Schunk, "All-optical frequency conversion in a traveling wave semiconductor laser amplifier," *IEEE J. Quantum Electron.* **27**, 1271-1279 (1991).
14. K. Inoue, "Tunable and selective wavelength conversion using fiber four-wave mixing with two pump lights," *IEEE Photon. Technol. Lett.* **6**, 1451-1453 (1994).
15. I. Tomkos, I. Zacharopoulos, D. Syvridis, T. Spicopoulos, C. Caroubalos, and E. Roditi, "Improved performance of a wavelength converter based on dual pump four-wave mixing in a bulk semiconductor optical amplifier," *Appl. Phys. Lett.* **72**, 2499-2501 (1998).
16. T. Morgan, J. Lacey, and R. Tucker, "Widely tunable four-wave mixing in semiconductor optical amplifiers with constant conversion efficiency," *IEEE Photon. Technol. Lett.* **10**, 1401-1403 (1998).
17. I. Tomkos, I. Zacharopoulos, D. Syvridis, T. Spicopoulos, C. Caroubalos, and E. Roditi, "Performance of a reconfigurable wavelength converter based on dual-pump four-wave mixing in a semiconductor optical amplifier," *IEEE Photon. Technol. Lett.* **10**, 1404-1406 (1998).
18. G. Hunziker, R. Paiella, D. Geraghty, K. Vahala, and U. Koren, "Polarization-independent wavelength conversion at 2.5 Gb/s by dual-pump four-wave mixing in a strained semiconductor optical amplifier," *IEEE Photon. Technol. Lett.* **8**, 1633-1635 (1996).
19. P. O. Hedekvist, M. Karlsson, and P. A. Andrekson, "Polarization dependence and efficiency in a fiber four-wave mixing phase conjugator with orthogonal pump waves," *IEEE Photon. Technol. Lett.* **8**, 776-778 (1996).
20. M. Eiselt, R. Schnabel, and E. Dietrich, "Polarization insensitive frequency converter with the capability of chirp removal," *IEEE Photon. Technol. Lett.* **10**, 63-65 (1998).

21. I. Zacharopoulos, I. Tomkos, D. Syvridis, T. Sphicopoulos, C. Caroubalos, and E. Roditi, "Study of polarization-insensitive wave mixing in bulk semiconductor optical amplifiers," *IEEE Photon. Technol. Lett.* **10**, 352-354 (1998).
22. A. Mecozzi, G. Contestabile, F. Martelli, L. Graziani, A. D'Ottavi, P. Spano, R. Dall'Ara, J. Eckner, F. Girardin, and G. Gueskos, "Optical spectral inversion without frequency shift by four-wave mixing using two pumps with orthogonal polarization," *IEEE Photon. Technol. Lett.* **10**, 355-357 (1998).
23. A. Mecozzi, G. Contestabile, L. Graziani, F. Martelli, A. D'Ottavi, P. Spano, R. Dall'Ara, and J. Eckner, "Polarization-insensitive four-wave mixing in a semiconductor optical amplifier," *Appl. Phys. Lett.* **72**, 2651-2653 (1998).
24. G. Contestabile, F. Martelli, A. Mecozzi, L. Graziani, A. D'Ottavi, P. Spano, G. Gueskos, R. Dall'Ara, and J. Eckner, "Efficiency flattening and equalization of frequency up- and down-conversion using four-wave mixing in semiconductor optical amplifiers," *IEEE Photon. Technol. Lett.* **10**, 1398-1400 (1998).
25. J. Minch, C. S. Chang, and S. L. Chuang, "Wavelength conversion using two-pump four-wave mixing in a double-modulated distributed-feedback laser," presented at Lasers and Electro-Optics Society 1997 Meeting of the IEEE, San Francisco, Calif., Nov. 10-13, 1997, paper MN3.
26. W. Fang, A. Hsu, S. L. Chuang, T. Tanbun-Ek, and A. M. Sergent, "Measurement and modeling of distributed-feedback lasers with spatial hole burning," *IEEE J. Sel. Top. Quantum Electron.* **2**, 547-554 (1997).
27. P. Szczepanski, "Semiclassical theory of multimode operation of a distributed feedback laser," *IEEE J. Quantum Electron.* **24**, 1248-1257 (1988).
28. S. L. Chuang, *Physics of Optoelectronic Devices* (Wiley, New York, 1995).
29. G. Agrawal, "Population pulsations and nondegenerate four-wave mixing in semiconductor lasers and amplifiers," *J. Opt. Soc. Am. B* **5**, 147-159 (1988).
30. W. Yee and K. Shore, "Nearly degenerate four-wave mixing in laser diodes with nonuniform longitudinal gain distribution," *J. Opt. Soc. Am. B* **11**, 1221-1228 (1994).
31. S. Ito, M. Suehiro, T. Hirata, and T. Hidaka, "Two-longitudinal mode laser diodes," *IEEE Photon. Technol. Lett.* **7**, 959-961 (1995).

# REPORT DOCUMENTATION PAGE

Form Approved

OMB No. 0704-0188

Public reporting burden for this collection of information is estimated to average 1 hour per response, including the time for reviewing instructions, searching existing data sources, gathering and maintaining the data needed, and completing and reviewing the collection of information. Send comments regarding this burden estimate or any other aspect of this collection of information, including suggestions for reducing this burden to Washington Headquarters Services, Directorate for Information Operations and Reports, 1215 Jefferson Davis Highway, Suite 1204, Arlington, VA 22202-4302, and to the Office of Management and Budget, Paperwork Reduction Project (0704-0188), Washington, DC 20503.

1. AGENCY USE ONLY (Leave blank)		2. REPORT DATE February 1, 2000		3. REPORT TYPE AND DATES COVERED Final Technical	
4. TITLE AND SUBTITLE High-Bandwidth Direct Modulation of Distributed-Feedback Quantum-Well Lasers				5. FUNDING NUMBERS N00014-96-1-0902	
6. AUTHOR(S) S. L. Chuang					
7. PERFORMING ORGANIZATION NAMES(S) AND ADDRESS(ES) University of Illinois Dept. of Electrical & Computer Engineering 1406 W. Green Street Urbana, IL 61801				8. PERFORMING ORGANIZATION REPORT NUMBER	
9. SPONSORING / MONITORING AGENCY NAMES(S) AND ADDRESS(ES) Office of Naval Research ATTN: ONR 353 (AASERT) 800 N. Quincy Street, Room 804 Arlington, VA 22217-5660				10. SPONSORING / MONITORING AGENCY REPORT NUMBER	
11. SUPPLEMENTARY NOTES					
a. DISTRIBUTION / AVAILABILITY STATEMENT Approved for public release				12. DISTRIBUTION CODE	
13. ABSTRACT (Maximum 200 words)  Wide-bandwidth microwave modulation of semiconductor strained quantum-well lasers using distributed-feedback structures plays an important role in high bit-rate optical communication systems. It is therefore critical to conduct research on the device physics of strained semiconductor quantum-well lasers under high-frequency modulation and on the creation of new techniques to characterize high-speed quantum-well lasers. The goals of this project are (1) to design and fabricate high bandwidth distributed-feedback quantum-well lasers using strain effects and (2) to combine microwave and optical measurement techniques to investigate the physics and device performance of quantum-well lasers under high-speed modulation conditions. The project is interdisciplinary in nature since optoelectronic device technology, microwave and optical measurement techniques will be introduced to the study of high-frequency modulation of quantum-well lasers for optical communication systems.					
14. SUBJECT TERMS strained quantum-well lasers, semiconductor lasers, optoelectronics, integrated laser-modulators				15. NUMBER OF PAGES	
				16. PRICE CODE	
17. SECURITY CLASSIFICATION OF REPORT unclassified	18. SECURITY CLASSIFICATION OF THIS PAGE unclassified	19. SECURITY CLASSIFICATION OF ABSTRACT unclassified	20. LIMITATION OF ABSTRACT UL		